

ULTRA-WIDEBAND TEM HORNS, TRANSIENT ARRAYS
AND EXPONENTIAL CURVES: A FDTD LOOK

THESIS

Troy S. Utton, B.S.E.E

Captain, USAF

AFIT/GE/ENG/99M-29

Approved for public release, distribution unlimited

19990413 108

REPORT DOCUMENTATION PAGE			Form Approved OMB No. 0704-0188	
Public reporting burden for this collection of information is estimated to average 1 hour per response, including the time for reviewing instructions, searching existing data sources, gathering and maintaining the data needed, and completing and reviewing the collection of information. Send comments regarding this burden estimate or any other aspect of this collection of information, including suggestions for reducing this burden, to Washington Headquarters Services, Directorate for Information Operations and Reports, 1215 Jefferson Davis Highway, Suite 1204, Arlington, VA 22202-4302, and to the Office of Management and Budget, Paperwork Reduction Project (0704-0188), Washington, DC 20503.				
1. AGENCY USE ONLY (Leave blank)		2. REPORT DATE March 1999		3. REPORT TYPE AND DATES COVERED Master's Thesis
4. TITLE AND SUBTITLE ULTRA-WIDEBAND TEM HORNS, TRANSIENT ARRAYS AND EXPONENTIAL CURVES: A FDTD LOOK			5. FUNDING NUMBERS	
6. AUTHOR(S) Troy S. Utton, Capt., USAF				
7. PERFORMING ORGANIZATION NAME(S) AND ADDRESS(ES) Air Force Institute of Technology 2950 P Street WPAFB OH 45433-7765			8. PERFORMING ORGANIZATION REPORT NUMBER AFIT/GE/ENG/99M-29	
9. SPONSORING/MONITORING AGENCY NAME(S) AND ADDRESS(ES) Jon S.H. Schoenberg, Maj. USAF Program Manager, Solid State Microwave Source Technology AFRL/DEMP 3550 Aberdeen Avenue, SE Kirtland AFB NM 87117-5776 Phone 505-246-0650			10. SPONSORING/MONITORING AGENCY REPORT NUMBER	
11. SUPPLEMENTARY NOTES Dr. Andrew J. Terzuoli/937-255-3636 ext 4717/andrew.tezuoli@afit.af.mil				
12a. DISTRIBUTION AVAILABILITY STATEMENT Distribution Unlimited			12b. DISTRIBUTION CODE	
13. ABSTRACT (Maximum 200 words) This research investigates the possibility of applying exponentially curved conducting plates to single-element Transverse Electromagnetic (TEM) horns and their transient arrays to enhance the UWB characteristics already experienced by these radiators. The first part of this study demonstrates the Finite-Difference Time-Domain (FDTD) method's ability to duplicate experimental data, and establishes the baseline models used throughout the remainder of the research. The baseline models consist of the typical flat-triangle shaped conducting plates. The exponential taper models incorporate the exponential curves in the height, the width, and both the height and width directions. One, two- and four-element baseline configurations are compared to their respective exponential-curved models. The comparisons are made in both the time-domain and the frequency-domain. The research concludes that reflection are not reduced by the application of exponential curves, but that the curves can increase or decrease the peak field strength depending on the input pulse width and the direction to which the curve is applied. This research also demonstrates, with the FDTD method, the major benefits realized when transient arrays are constructed from these elements. The final product of this research results from the exploration of methods to reduce FDTD run-times of these types of problems. The run-times are reduced by 96%, and approach the run-times necessary for interfacing the FDTD method with an optimizing algorithm.				
14. SUBJECT TERMS TEM Horns, Finite-Difference Time-Domain, Transient Arrays, Exponential Tapers, Ultra-Wideband, Computational Electromagnetics			15. NUMBER OF PAGES 132	
			16. PRICE CODE	
17. SECURITY CLASSIFICATION OF REPORT Unclassified	18. SECURITY CLASSIFICATION OF THIS PAGE Unclassified	19. SECURITY CLASSIFICATION OF ABSTRACT Unclassified	20. LIMITATION OF ABSTRACT UL	

ULTRA-WIDEBAND TEM HORNS, TRANSIENT ARRAYS AND
EXPONENTIAL CURVES: A FDTD LOOK

THESIS

Presented to the Faculty of the School of Engineering
Of the Air Force Institute of Technology
Air University
In Partial Fulfillment of the
Requirements for the Degree of
Master of Science in Electrical Engineering

Troy S. Utton, B.S.E.E
Captain, USAF

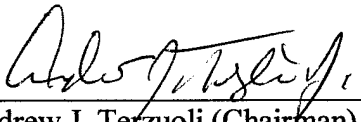
March 1999

Approved for public release, distribution unlimited

ULTRA-WIDE BAND TEM HORNS, TRANSIENT ARRAYS
AND EXPONENTIAL CURVES: A FDTD LOOK

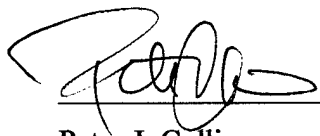
Troy S. Utton, B.S.E.E
Captain, USAF

Approved:



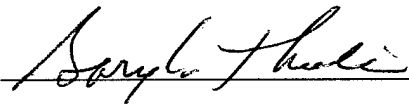
Andrew J. Terzuoli (Chairman)

12 Mar 99
Date



Peter J. Collins

12 MAR 99
Date



Gary A. Thiele

15 MAR 99
Date

Acknowledgements

Many elements had to come about to make this research effort happen. I would like to professional thank each person that provided support in one way or another. First of all I would like to thank my advisor, Dr. Andrew Terzuoli, and committee members, Dr. Gary Thiele and Major Peter Collins for their guidance in the beginning and then allowing me the flexibility of pursuing the objectives in my own fashion. I would also like to extend a special thank you to Dr. Terzuoli for providing the initial contacts at Phillips Laboratory, and for his constant encouragement.

The people at Phillips Laboratory also deserve special thanks. I want to express my gratitude to Bill Prather for the opportunity, hospitably, and support he gave me in my visit to the laboratory. I'm indebted to Major Jon Schoenberg who patiently answered my endless supply of questions. Without his sincere interest in the success of this study, it would not have been possible. I would also like to thank Dr. Joe Yakura who was instrumental in getting me started with TSAR

Also deserving thanks is John Ladbury, National Institute for Standards and Technology, for jumping though hoops to provide me with a valuable source of information, Dave Doak for computer support, and Captain Dave Van Veldhvizen for his technical advice concerning evolutionary algorithms.

I'll never be able to express enough gratitude to the next group. First I would like to thank my parents who have consistently provided support and encouragement, and made every achievement easy for me with their sacrifice and love. Secondly I would like to thank my mother-in-law who provided an immense amount of help in the last couple of weeks of this effort. The next two deserving thanks is the "Ty-nado" and "Bug" who never had daddy's complete attention during this process. Finally, without a doubt, the one deserving the biggest "Thank You" is the "Dungeon Master" or more affectionately known as "G". Thank you Glendora.

Troy S. Utton

Table of Contents

	Page
Acknowledgements.....	iii
List of Figure.....	vi
List of Table.....	xi
Abstract.....	xii
Chapter 1: Introduction.....	1
Objectives.....	3
Methodology.....	3
Terminology.....	4
Tools.....	6
Chapter 2: Background.....	9
Ultra-Wideband Radiators	9
Coupling Attack Modes.....	10
Requirements on Radiated Field.....	11
TEM Horns and Transient Arrays.....	15
Single Element.....	15
Design Considerations.....	16
Design Improvements.....	19
Transient Arrays.....	20
Time-Domain to Frequency-Domain and Back.....	21
Finite-Difference Time-Domain Method.....	22
Application Found In Literature.....	26
Plate Shaping and Exponential Tapers.....	27
Optimization Routines and FDTD.....	28
Chapter Review.....	30
Chapter 3: Methodology.....	31
Descriptions of Antennas and Models.....	31
Exponential Taper Design.....	33
Model Generation.....	33
Creating the CAD Model.....	33
Setting Material Properties.....	34
Development of the Double-Linear Models.....	35
Development of Y-Directed (Width) Exponential Taper Horn.....	38
Development of X-Directed (Height) Exponential Taper Horn.....	39
Development of Double-Exponential Taper Horn.....	40
Meshing.....	40
Determination of Cell Size.....	41
Excitation of the Antenna.....	46
Experimental Pulse and Modifications.....	47
Gaussian Pulse.....	50
Determination of Simulation Time.....	52
The Collection of the Data of Interest.....	52
Analysis Technique.....	54
Time-Domain.....	54

Frequency-Domain.....	54
Reduction of Run-Time Study.....	54
Chapter Review.....	55
Chapter 4: Results and Analysis.....	56
Establishing the Base Line.....	56
Differences Between Model and Experiment.....	60
Pulse and Bandwidth Limits.....	60
Exponential Curves - Peak Field Values Dominate.....	64
Time-Domain.....	64
Identifying and Quantifying Reflections.....	65
Frequency-Domain Analysis.....	67
Arrays.....	68
Reduction In Run-Time Study.....	71
Full vs. Quarter – 5mm Grid.....	71
Full Horn – 5mm vs. 10mm.....	72
Full vs. Quarter – 10mm Grid.....	73
Early-Time.....	74
Summary of Time-Reduction Study.....	75
Chapter Review.....	76
Chapter 5: Conclusions and Suggestions.....	77
Conclusions.....	77
Exponential Curves.....	79
Transient Arrays.....	79
Reduction in Run-Time Study.....	80
Summary of Conclusions.....	80
Suggestions for Further Research.....	80
Summary.....	81
Appendix A.....	83
Appendix B.....	89
Appendix C.....	98
Appendix D.....	107
Bibliography	116
Vita.....	119

List of Figures

	Page
Figure 1. TEM Horn Antenna – Basic Form.....	2
Figure 2. Exponential Taper in the X Direction.....	5
Figure 3. Exponential Taper in the Y Direction	5
Figure 4. Research Software/Process Flowchart.....	8
Figure 5. Experimental Input Pulse	12
Figure 6. Power Spectral Density for Experimental Pulse	12
Figure 7. PSD for Gaussian Pulse	13
Figure 8. Gaussian Input Pulse.....	14
Figure 9. PSD for Ideal Impulse Input Pulse.....	14
Figure 10. Ideal Input Pulse.....	15
Figure 11. Determination of High Frequency Cutoff.....	17
Figure 12. High Frequency Transmission Line Model of TEM Horn.....	18
Figure 13. Low Frequency Transmission Line Model of a TEM of Horn.....	18
Figure 14. Various Configurations of Four Element Arrays of TEM Horns.....	21
Figure 15. Field Vector Components in FDTD Cell.....	24
Figure 16. The Top and Side View of the TWIT.....	27
Figure 17. Top View TEM Horn	32
Figure 18. Side View TEM Horn	32
Figure 19. Inner-Solid Used to Form TEM Horn in MGED	35
Figure 20. MGED Solid Representation of Double-Linear TEM Horn	36
Figure 21. MGED Representation of Four-Element Array of TEM Horns – First Version	36
Figure 21. MGED Representation of Four-Element Array of TEM Horns – Redrawn Version	37
Figure 22. First Version Transient Responses vs. Redrawn Version (Version Two).....	38
Figure 23. MGED Method of Y-Directed Exponential Taper Construction	39
Figure 24. MGED Method of X-Directed Exponential Taper Construction – Side View	40

Figure 25. Transient Responses for 5mm,7mm, and 10mm Grid Resolutions.....	42
Figure 26. Meshed Model, Side View, Large Horn, X-Directed Linear Taper(left), X-Directed Exponential Taper(right).....	43
Figure 27. Meshed Model, Top View, Large Horn, Y-Directed Linear Taper.....	43
Figure 28. Meshed Model, Top View, Large Horn, Y-Directed Exponential Taper.....	43
Figure 29. Meshed Model, Side View, Small Horn, X-Directed Linear Taper.....	43
Figure 30. Meshed Model, Side View, Small Horn, X-Directed Exponential Taper.....	43
Figure 31. Meshed Model, Top View, Small Horn, Y-Directed Linear Taper.....	44
Figure 32. Meshed Model, Top View, Small Horn, Y-Directed Exponential Taper.....	44
Figure 33. Meshed Model, Side View, Large 4-Element Array, Linear Taper	44
Figure 34. Meshed Model, Side View, Large 4-Element Array(Version 2), Linear Taper	45
Figure 35. Meshed Model, Side View, Large 4-Element Array, Exponential Taper	45
Figure 36. Meshed Model, Side View, Small 4-Element Array, Linear Taper	46
Figure 37. Meshed Model, Side View, Small 4-Element Array, Exponential Taper	46
Figure 38. Experimental Pulse Before Modifications	48
Figure 39. Modification of Trailing End of Experimental Pulse	49
Figure 40. Final Input Pulse Form	50
Figure 41a. Guassian Pulse Applied to Large Horn	51
Figure 41b. Guassian Pulse Applied to Small Horn	51
Figure 42. Coordinate Convention	53
Figure 43. Application of Mirror Boundary Conditions	55
Figure 44. Single-Element Double-Linear Horn, Experimental Results vs. Simulated – PSD and Transient Response.....	57
Figure 45. 2-Element Array Double-Linear Horn (version 2) Experimental Results vs. Simulated – PSD and Transient Response.....	57

Figure 46. 4-Element Array Double-Linear Horn (version 2) Experimental Results vs. Simulated – PSD and Transient Response	58
Figure 47. Two-Element Double (version 1)-Linear Horn, Experimental Results vs. Simulated – PSD and Transient Response	59
Figure 48. Four-Element Double-Linear Horn(version 1), Experimental Results vs. Simulated – PSD and Transient Response.....	59
Figure 49. PSD of Experimental and Gaussian Input pulse and the Corresponding Outputs from the Single-Element Double-Linear Horn	61
Figure 50. Creation of the Standing Wave	62
Figure 51. Transient Response Resulting from Guassian Pulse Excitation of the Double-Linear Single-Element Horn	63
Figure 52. Frequency Response Resulting from Segmentation of Total Transient Response.....	64
Figure 53. Looking Inside the Large Horn – $\frac{1}{4}$ the Length from the Feed and On Boresite – Experimental Input Pulse.....	66
Figure 54. Looking Inside the Small Horn – $\frac{1}{2}$ the Length from the Feed and On Boresite – Gaussian Input Pulse.....	67
Figure 55. Positive Portion of Initial Gaussian Pulse Large 2-Element Array	68
Figure 56. Negative Portion of Initial Gaussian Pulse Large 2-Element Array	68
Figure 57. PSD of Entire Initial (Early) Gaussian Pulse Large 2-Element Array	68
Figure 58. PSD of Entire Transient Response Gaussian Pulse, Large 2-Element Array.....	68
Figure 59. Comparison of Transient Response of 1-Element, 2-Element, and 4-Element Double-Linear Configurations	69
Figure 60. A Comparison of Each Element of the 4-Element Array and the Single-Element Horn of the Same Design	70
Figure 61. Full and Quarter Horn Comparison (5mm Cell Size).....	72
Figure 62. Full - 5mm vs. 10mm Comparison	73
Figure 63. Full and Quarter Horn Comparison (10mm Cell Size).....	74
Figure 64. Summary of Reduction of Run-Time Study.....	75
Figure A-1. Frequency Response Resulting from Segmentation of Total Transient Response (Experimental Pulse)	83

Figure A-2. PSD Comparison of 1, 2, and 4 Element Arrays Large Horn (Experimental Input Pulse).....	84
Figure A-3. PSD Comparison of 1, 2, and 4 Element Arrays Large Horn (Gaussian Input Pulse).....	85
Figure A-4. Transient Response Comparison of 1, 2, and 4 Element Arrays Large Double-Linear (Gaussian Input Pulse).....	86
Figure A-5. Transient Response Comparison of 1, 2, and 4 Element Arrays Small Double-Linear (Gaussian Input Pulse).....	87
Figure A-6. PSD Comparison of 1, 2, and 4 Element Arrays Small Horn (Gaussian Input Pulse).....	88
Figure B-1. Comparison of Double-Linear and X-dir Exponential Taper Curve (1-Element, Large Horn, Experimental Input Pulse).....	89
Figure B-2. Comparison of Double-Linear and Y-dir Exponential Taper Curve (1-Element, Large Horn, Experimental Input Pulse).....	90
Figure B-3. Comparison of Double-Linear and Double-Exponential Taper Curve (1-Element, Large Horn, Experimental Input Pulse).....	91
Figure B-4. Comparison of Double-Linear and X-dir Exponential Taper Curve (2-Element, Large Horn, Experimental Input Pulse).....	92
Figure B-5. Comparison of Double-Linear and Y-dir Exponential Taper Curve (2-Element, Large Horn, Experimental Input Pulse).....	93
Figure B-6. Comparison of Double-Linear and Double-Exponential Taper Curve (2-Element, Large Horn, Experimental Input Pulse).....	94
Figure B-7. Comparison of Double-Linear and X-dir Exponential Taper Curve (4-Element, Large Horn, Experimental Input Pulse).....	95
Figure B-8. Comparison of Double-Linear and Y-dir Exponential Taper Curve (4-Element, Large Horn, Experimental Input Pulse).....	96
Figure B-9. Comparison of Double-Linear and Double-Exponential Taper Curve (4-Element, Large Horn, Experimental Input Pulse).....	97
Figure C-1. Comparison of Double-Linear and X-dir Exponential Taper Curve (1-Element, Large Horn, Gaussian Input Pulse).....	98
Figure C-2. Comparison of Double-Linear and Y-dir Exponential Taper Curve (1-Element, Large Horn, Gaussian Input Pulse)	99
Figure C-3. Comparison of Double-Linear and Double-Exponential Taper Curve (1-Element, Large Horn, Gaussian Input Pulse).....	100
Figure C-4. Comparison of Double-Linear and X-dir Exponential Taper Curve (2-Element, Large Horn, Gaussian Input Pulse).....	101

Figure C-5. Comparison of Double-Linear and Y-dir Exponential Taper Curve (2-Element, Large Horn, Gaussian Input Pulse).....	102
Figure C-6. Comparison of Double-Linear and Double-Exponential Taper Curve (2-Element, Large Horn, Gaussian Input Pulse).....	103
Figure C-7. Comparison of Double-Linear and X-dir Exponential Taper Curve (4-Element, Large Horn, Gaussian Input Pulse)	104
Figure C-8. Comparison of Double-Linear and Y-dir Exponential Taper Curve (4-Element, Large Horn, Gaussian Input Pulse).....	105
Figure C-9. Comparison of Double-Linear and Double-Exponential Taper Curve (4-Element, Large Horn, Gaussian Input Pulse).....	106
Figure D-1. Comparison of Double-Linear and X-dir Exponential Taper Curve (1-Element, Small Horn, Gaussian Input Pulse).....	107
Figure D-2. Comparison of Double-Linear and Y-dir Exponential Taper Curve (1-Element, Small Horn, Gaussian Input Pulse)	108
Figure D-3. Comparison of Double-Linear and Double-Exponential Taper Curve (1-Element, Small Horn, Gaussian Input Pulse).....	109
Figure D-4. Comparison of Double-Linear and X-dir Exponential Taper Curve (2-Element, Small Horn, Gaussian Input Pulse).....	110
Figure D-5. Comparison of Double-Linear and Y-dir Exponential Taper Curve (2-Element, Small Horn, Gaussian Input Pulse).....	111
Figure D-6. Comparison of Double-Linear and Double-Exponential Taper Curve (2-Element, Small Horn, Gaussian Input Pulse).....	112
Figure D-7. Comparison of Double-Linear and X-dir Exponential Taper Curve (4-Element, Small Horn, Gaussian Input Pulse).....	113
Figure D-8. Comparison of Double-Linear and Y-dir Exponential Taper Curve (4-Element, Small Horn, Gaussian Input Pulse).....	114
Figure D-9. Comparison of Double-Linear and Double-Exponential Taper Curve (4-Element, Small Horn, Gaussian Input Pulse).....	115

List of Tables

	Page
Table 1. Summary of Horn Dimensions.....	31
Table 2. Peak Field Strengths and Design vs. Baseline Comparisons.....	65
Table 3. Ranking of Designs According to Peak Field Strengths.....	78

Abstract

This research investigates the possibility of applying exponentially curved conducting plates to single-element Transverse Electromagnetic (TEM) horns and their transient arrays to enhance the UWB characteristics already experienced by these radiators. The first part of this study demonstrates the Finite-Difference Time-Domain (FDTD) method's ability to duplicate experimental data, and establishes the baseline models used throughout the remainder of the research. The baseline models consist of the typical flat-triangle shaped conducting plates. The exponential taper models incorporate the exponential curves in the height, the width, and both the height and width directions. One, two- and four-element baseline configurations are compared to their respective exponential-curved models. The comparisons are made in both the time-domain and the frequency-domain. The research concludes that reflection are not reduced by the application of exponential curves, but that the curves can increase or decrease the peak field strength depending on the input pulse width and the direction to which the curve is applied. This research also demonstrates, with the FDTD method, the major benefits realized when transient arrays are constructed from these elements. The final product of this research results from the exploration of methods to reduce FDTD run-times of these types of problems. The run-times are reduced by 96%, and approach the run-times necessary for interfacing the FDTD method with an optimizing algorithm.

Ultra-Wideband TEM Horns, Transient Arrays, And Exponential Curves: A FDTD Look

Chapter 1: Introduction

Transverse Electromagnetic (TEM) horn antennas are showing promise as ultra-wideband (UWB) radiators in the world of directed energy weapons (DEW). Due to their relatively small size and simple construction, transient arrays of TEM elements are easily fabricated. This, combined with the fact that smaller elements require smaller sources, makes them an attractive alternative to other antennas of choice in the DEW arena, the reflector and lens Impulse Radiating Antenna (IRA).

The TEM horn is a two-conductor, end-fire, traveling wave structure, which when designed correctly has the added advantage over other broadband sources, such as the spiral and logarithmic antennas, in that all frequencies are radiated in phase with each other [1]. The two conductors of the TEM horn essentially form a transmission line whose characteristic impedance is matched to the feeding transmission line to reduce reflections from the source. Figure 1 is an illustration of the TEM horn in its most basic form. On transmission, assuming the aperture size is electrically small, the TEM horn radiates on bore-sight the first temporal derivative of the input pulse [2]. The horn also provides directivity not achieved with other antennas, which becomes a positive attribute when the goal is to focus energy on a target. Problems, however, arise that hamper the performance of TEM horn antennas. Reflections, diffraction, and the low frequency performance are all issues that need to be dealt with in order for this class of antennas to operate as required.

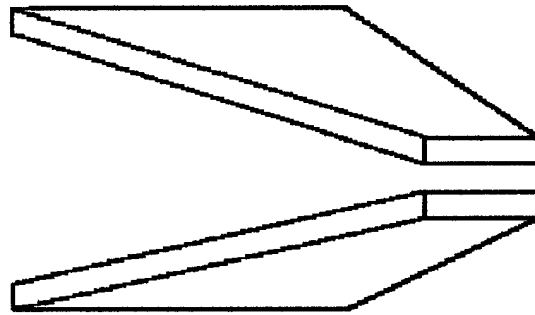


Figure 1. TEM Horn Antenna – Basic Form

Techniques addressing each of these concerns have been studied and employed with success, but each technique comes with design tradeoffs. One technique that has only received mild attention considers exponentially curved conducting plates instead of the standard linear design most often associated with these types of horns. The idea behind the exponential curves is to produce a gradual transition to the free space impedance seen at the aperture of the horn.

This research investigates the possibility of applying exponentially curved conducting plates to single-element TEM horns and transient arrays to enhance the UWB characteristics already experienced by these radiators. The Finite-Difference Time-Domain (FDTD) method is employed as the numerical analysis implement.

This chapter gives a brief overview of the document. Some of the terms that might be encountered and unfamiliar to the reader are explained. The objectives of the research are stated, a terse look at the methodology is given, and it finishes with a quick look at the tools being utilized. Chapter 2 details the background of UWB weapons and the need for pulses with fast rise-times and high spectral content. It takes a look at the TEM horn research found in the literature as well as some FDTD studies concerning this topic. The last part of the literature review presents the motivation for the exponential curved plates. Chapter 3 shows the development of the models under test, as well as the

test procedure. Chapter 4 is the presentation of results and the fifth chapter completes the document with a conclusion, summary, and suggested research areas.

Objectives

This research project has two goals or objectives. The main goal is to investigate how exponential curves, applied to the conducting elements of TEM horns and 2 and 4-element arrays of the same horns, effect the wide-band characteristics of the radiated pulse. As a byproduct, the second objective is to investigate the use of perfect electric conducting (PEC) and perfect magnetic conducting (PMC) boundary conditions to lessen the computational volume. The intentions are to reduce the run-time down to a level that would allow the code being used to interface with an optimizing algorithm, while delivering a replication of the data generated with a full model.

Methodology

To begin with, FDTD runs are compared with experimental data to determine the code's ability to simulate reality. Data exists for a single element horn with linear flares, as well as two and three-element linear arrays of the same horn. Once confidence is gained, a test matrix is established with 39 variations of the TEM horn. Some of the variations are duplication in configuration, and only fed with different input pulses, while others have a completely different set of dimensions. The idea is to determine if the characteristics resulting from the curvature variation are repeatable between dimensionally different horns and whether the characteristics produce desirable effects. A complete description of each variation along with the purposes of each is provided in Chapter 3.

To achieve the second objective some particular variations are chosen from the test matrix to be used in the reduction in run-time study. This portion of the research begins by taking the configuration with the longest run time, applying mirror boundary

conditions to reduce the computational volume, comparing the results to the full model case, and comparing runtimes.

In each case the time-domain or transient response is analyzed as well as the power spectral density (PSD). The PSD is generated using a Fast Fourier Transform (FFT) routine. The only limitation on the bandwidth analyzed is determined by the upper limit of the FDTD method. The period for time-domain analyzes is 10 to 15 round trip transient times, 2τ , as determined by the physical dimensions of the horn under investigation and the speed of light. Peaks in the transient response, attributable to reflections are identified and the differences noted. Again, the double linear horn is considered the baseline configuration.

Terminology

Some of the terminology encountered to this point and from here on might be unfamiliar to the reader. This maybe, impart, due to the relatively newness of this research area, or it might be due to the author's own interjections of terminology. It is the intentions of this section to clarify these terms. One such term that appears in literature several times is the use of *taper* as applied to TEM horns. Predominately it is used to refer to resistive loading of the conducting plates, but Wolstenholme [3] applies tapered periodic surfaces to the ends of the conducting plates of a TEM horn in his thesis research. *Taper* in this research effort simply refers to the curvature of the conducting plates, as illustrated in Figure 2 and Figure 3. The terms *taper*, *flare*, and *curvature* are used interchangeably throughout this document.

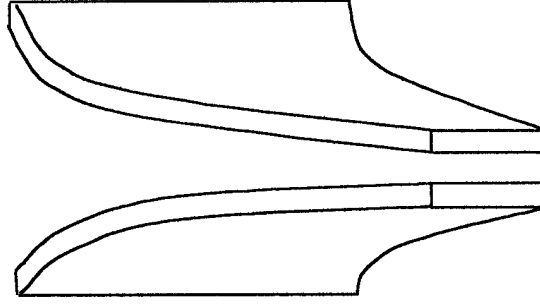


Figure 2. Exponential Tapered in the X Direction

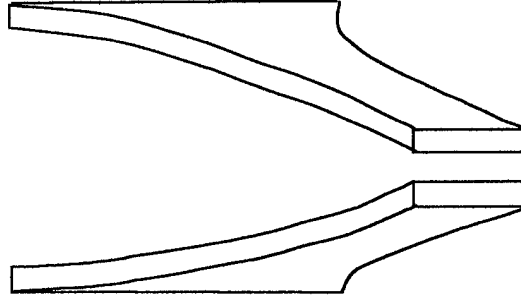


Figure 3. Exponential Taper in the Y Direction

To realize the goal of these antennas and the role they play in ultra-wideband (UWB) systems it is important to know the definition used to classify these systems as UWB. Similar to the defining equation found in [4] for broadband systems, [5] takes it a step further and includes a categorization that introduces the criteria for UWB antennas in terms of its fractional bandwidth. The fractional bandwidth, B_F is given by

$$B_F = \frac{f_U - f_L}{(f_U + f_L)/2} 100\%, \quad (1)$$

where f_L is the lowest frequency with a significant contribution and f_U is the upper frequency of significance. Narrow-band antennas fall in the 0% to 1% range, wide-band

in the range between 1% and 25%, and UWB antennas 25% up to but not including 200%. Two hundred percent must be excluded from the range because it would require f_U to have a zero frequency, or D.C. value, which does not radiate from a physical antenna. As an example of the fractional bandwidth of a UWB antennas, one design of the reflector IRA has achieved a B_F of 180%, or a band-ratio of 60. Band-ratio is another figure of merit used to categorize UWB systems and is given by f_U / f_L .

To generate an ultra-wideband signal in the UWB range discussed above, these systems must operate in the time domain. This is accomplished by applying an impulse to the system. An impulse implies zero rise-time, which is not physically realizable. The pulses used to excite UWB antennas will always have a non-zero rise-time, and therefore are not a true impulse. In the literature, impulse, pulse, and impulse-like are used interchangeably, as is done in this document.

Tools

This research effort exercises the capability of 5 different pieces of software. The models are designed and drawn with a computer aided design (CAD) program developed by the United States Army's Ballistic Research Laboratory (BRL) at Aberdeen, Maryland. The program package, BRL-CAD, consists of a collection of tools for computer aided design, graphics, and image processing. The solid model editor portion of the package, MGED (Multi-device Graphics Editor), is used to generate the 3-dimensional (3D) models used throughout this investigation. A more thorough description of this program will be given later as will the procedure used to develop the test models.

Once the solid models are created, they are put into the mesh format required by the FDTD program. The automatic mesh-generator, Anastasia (Ana), grids the object into cells and produces the input file required by the FDTD program. Ana was developed around the BRL-CAD program by Lawrence Livermore National Laboratory, with the

intended purpose of generating meshes for the FDTD method. The smallest cell size allowed by Ana is 1mm^3 .

Before the FDTD method is applied to the meshed antenna, it is necessary to inspect the meshed horn to insure it, as accurately as possible, represent the antenna. The program used to accomplish this task is called Image. Image allows the meshed model to be rotated in the 3 dimensions and allows the user to zoom in on specific areas of interest. An example of the need to view the meshed object is when the aperture and feed dimensions are critical. The meshing might result in smaller than desired aperture dimensions, which would require different conductor spacing or a different cell dimension.

The final step to producing the output is accomplished with another code developed by Lawrence Livermore National Laboratory. The Temporal Scattering And Response (TSAR, pronounced like *czar*) FDTD software package is the computational engine for producing the radiated fields from the antennas under-test. Some of the features of this program are:

- 1) Portable to many different platforms.
- 2) Able to run problems much larger than the computers memory due to a built in virtual memory routine.
- 3) It is quite flexible; over 70 different input variables control the operation of the software.
- 4) One can apply a large range of electromagnetic fields (arbitrary plane waves, user defined incident fields, electric dipoles, and magnetic dipoles)
- 5) Able to produce a large number of output quantities with a single run
- 6) Well documented code [7].

The operation of TSAR requires three to seven input files depending on the problem. Scattered, radiated, and coupled field data, as well as current data, can be collected at any

point within the computational volume, or through the use of near-to-far field transforms, anywhere in space. The ability to collect output data with this code is outstanding.

The post processing of the data is accomplished with the graphing and Fast Fourier Transform routines of MATLAB®.

Figure 4 gives a visual summary of the software used and process followed from model generation to useful field data.

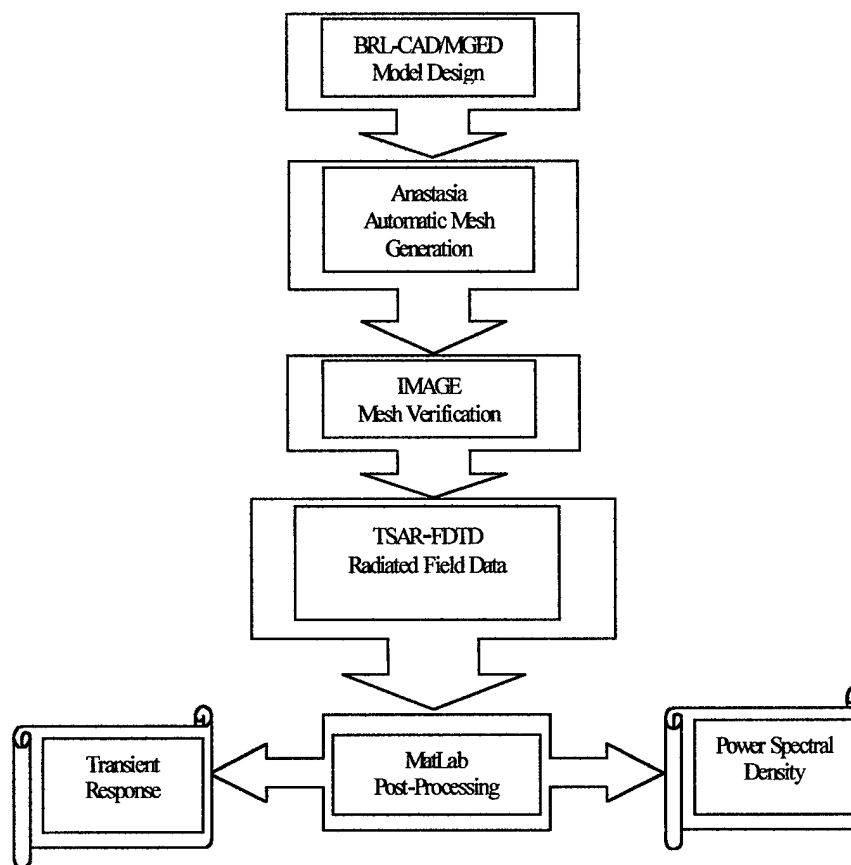


Figure 4. Research Software/Process Flowchart

Chapter 2: Background

Several specific areas of research interest (UWB radiators, TEM horns, transient arrays, the FDTD method, exponential tapers, and evolutionary algorithms) are combined to bring about this specific undertaking. Therefore the goal of this chapter is not to teach the theory of any one area, but to present a reading bibliography and highlight some of the areas that might be of interest. The reader is encouraged to pursue a more complete explanation of a specific area of interest in the sources provided.

Ultra-Wideband Radiators

The use of a horn as a weapon can be seen as far back as biblical times when the walls of Jericho were felled with focused acoustical energy. Turning from the past toward the present day brings targets filled with electronic components (communications systems, flight control systems, fire control system, navigation systems, etc.) The destructive or disruptive energy comes in the form of electromagnetic radiation. This, of course, is only one of the applications of ultra-wideband (UWB) systems, on which the antenna of this research effort is focused. Other uses include UWB communication systems, target recognition and avoidance systems, and detection devices.

The latter uses are primarily concerned with the reception of UWB signals, while the former is focused on the transmit properties of these types of systems. When antenna's theory of reciprocity is applied, they exhibit the same properties in transmit and receive, only the objectives differ in each application. Because the transmit characteristics of some UWB antennas are explored in this study a brief description of their uses will be explained in order to illustrate the requirements put on an UWB pulse.

Regardless of the target system's function, assuming it contains electrical components, electromagnetic energy can and will effect its operation when applied correctly. Correctly, in most cases, is not easily defined and that is where the benefits of an Ultra-wideband pulse proves themselves.

Coupling Attack Modes

There are basically two methods of coupling energy into the target system, through the *front-door* and through the *back-door*. *Front-door* coupling results from energy received through antennas and other sensors. This type of coupling requires more knowledge/intelligence of the target system and would not necessarily require an UWB pulse. Continuous wave radiation at the correct in-band frequency would be just as or more effective. The potential power, P , coupled into a target system is

$$P = S\sigma, \quad (2)$$

where S is the incident power density and σ is the coupling cross sectional area. This is a very generalized equation and many factors come into effect. For *front-door* coupling through an antenna, σ is the effective area of the antenna. Because the effective area peaks in the in-band frequency, f , the coupled power falls off sharply as f^2 above the in-band frequency and f^4 below. This also assumes you are in the main lobe of the target antenna; side lobe irradiation will be much less effective. [8] The preceding discussion again illustrates the benefit of UWB radiation. An UWB signal would include the in-band frequency of the antenna along with the rest of the bandwidth that would have the potential for coupling through *back-door* paths.

Back-door coupling is the coupling of energy into the target system through apertures resulting from the constructions of the target system. *Back-door* coupling paths can include seams, cracks, hatches, access panels, windows, doors, unshielded or improperly shield cables, etc. [8] Slots created or resulting from fins, in particular those that deploy after launch, are another major vulnerability that can be attacked. The slots are most susceptible to magnetic fields and act as $\lambda/2$ -antennas, especially when the H-field is oriented parallel to the slots. The wings and fins respond best to E-fields oriented parallel to them, and when they extend into the body cavity they act as a secondary radiation source. In this case the fins and wings act as $\lambda/4$ -antennas, but if they are

attached to the munitions body they respond as $\lambda/2$ -antennas and the coupled surface current on the wings is passed on to the body. [9]

Requirements on Radiated Field

The goal of directed-energy weapons (DEW), of which UWB systems are a part, is to deposit as much energy as possible on the target in order to produce a desired affect. By deploying a signal that imparts high energy levels to a wide-band of frequencies, the user is allowed to be more generic in the attack mode. Less intelligence on the target systems is required and multiple targets can be engaged by one system.

Theoretically, an impulse in time would access all the desired frequencies plus some. It would produce the ultimate frequency bandwidth, zero to infinity. Of course this is only academic, because a true impulse can not be generated. There is a non-zero rise-time and fall-time. Research is ongoing to reduce both, the goal being to increase the spectral content and consequently the bandwidth of the signal. Pulses like the one shown in Figure 5 are generated with stacked Blumleins for voltage multiplication and triggered with fast photoconductive gallium arsenide (GaAs) avalanche type switches. These solid-state source are capable of 200-300 picosecond rise-times with a repetition rate of 1-200 Hz. With some modifications the rise-times, pulse duration, and peak values can be controlled.[10] The pulse shown in Figure 5 is used to feed some of the models found in this report and Figure 6 is its PSD.

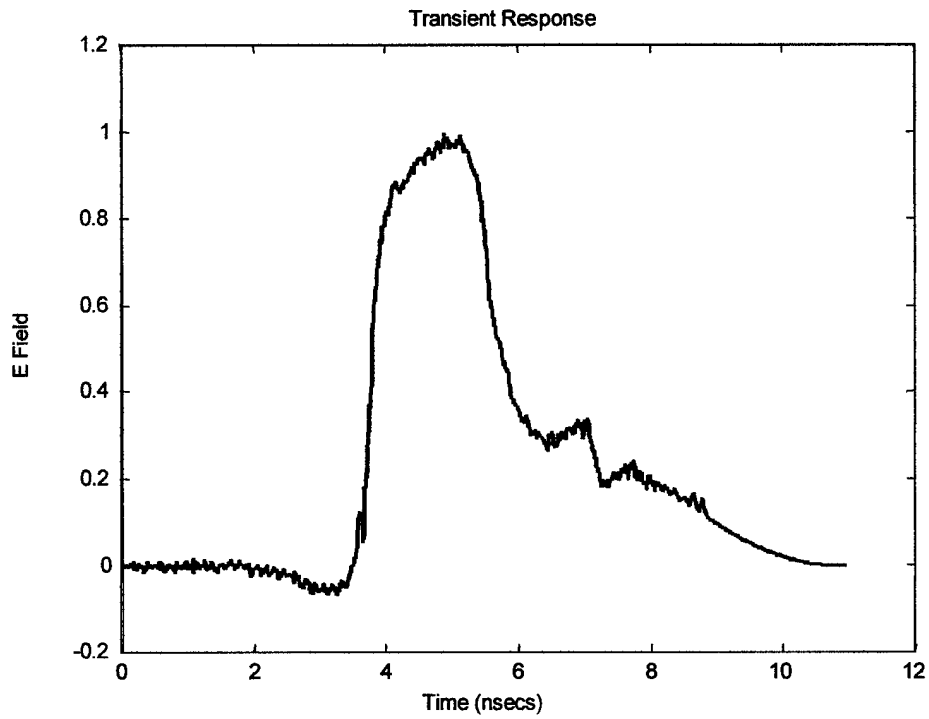


Figure 5. Experimental Input Pulse

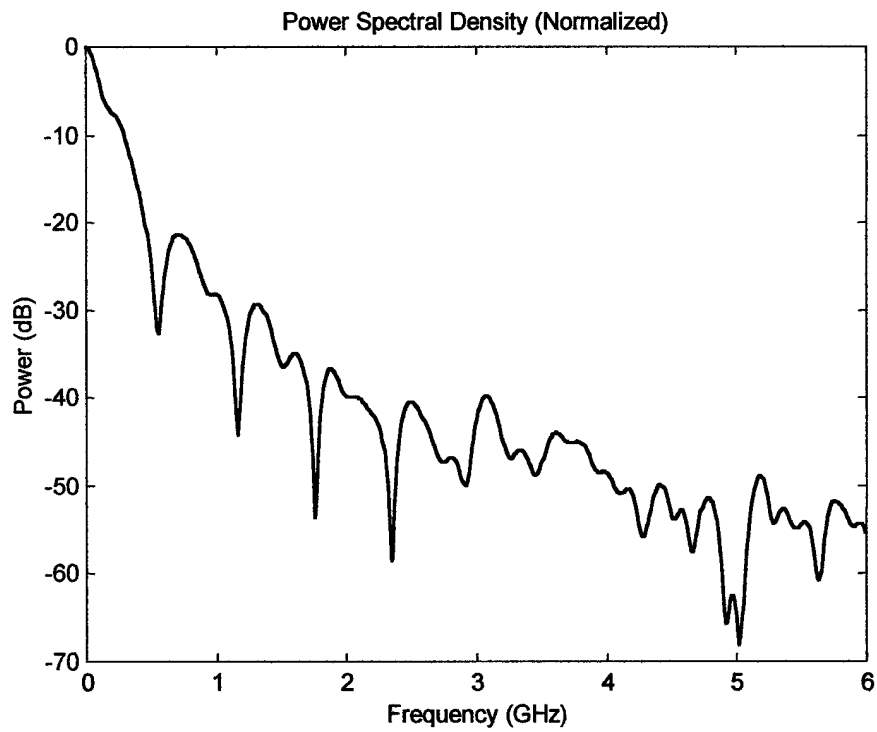


Figure 6. Power Spectral Density (PSD) for Experimental Pulse

Notice that the PSD is fairly flat from approximately 1.8 GHz to 4 GHz with the exception of the severe negative spike at 2.3 GHz, and that the higher energy content is in the 0-2 GHz range. The goal is to produce something like what is shown in Figure 7. Figure 7 is the PSD produced with the gaussian pulse shown in Figure 8. Note the difference in the magnitude scale between Figure 6 and Figure 7. Obviously the gaussian pulse generates the more desirable PSD, unless some specific application or target requires the peak power level at the 0-500Mhz wavelength.

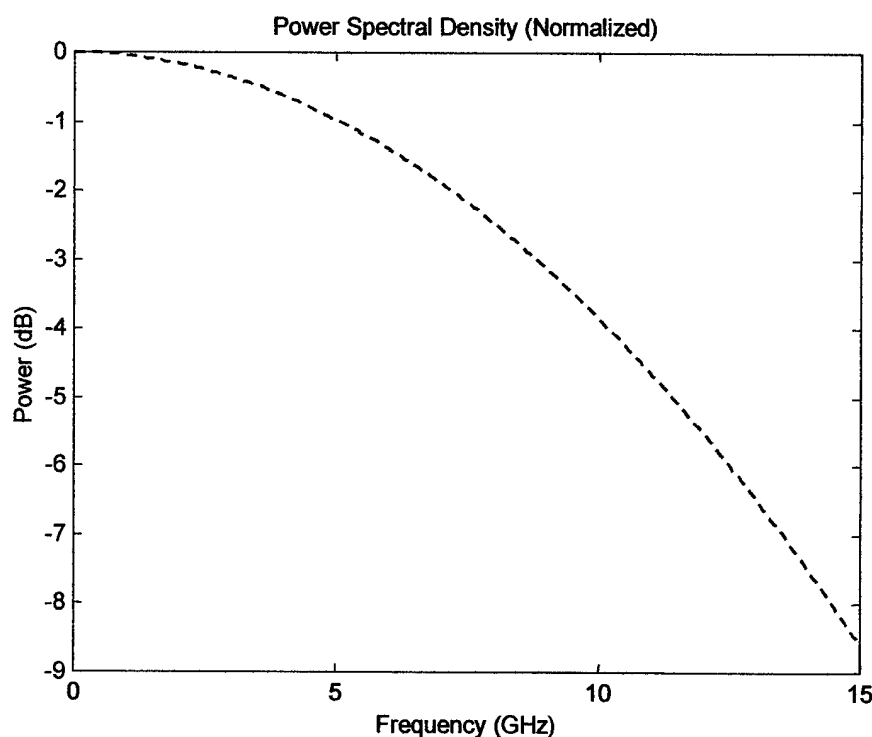


Figure 7. PSD for Gaussian Pulse

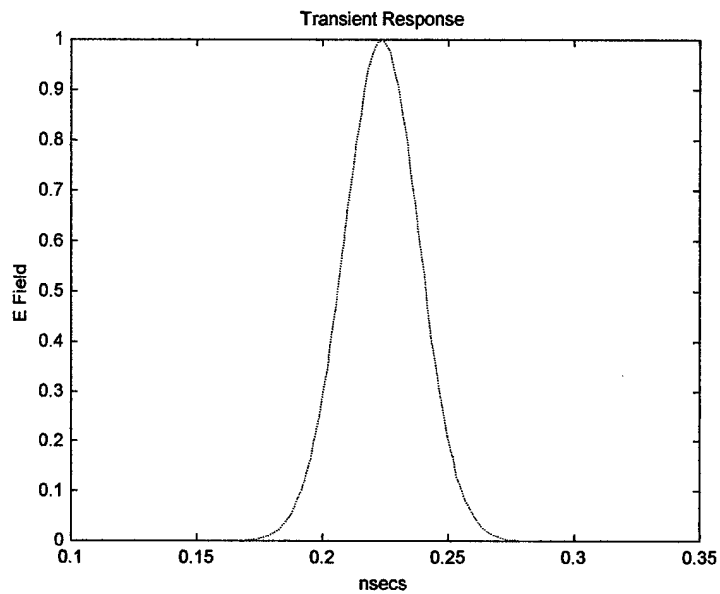


Figure 8. Gaussian Input Pulse

The ideal PSD is shown in Figure 9 and would be generated with the unrealizable impulse function shown in Figure 10.

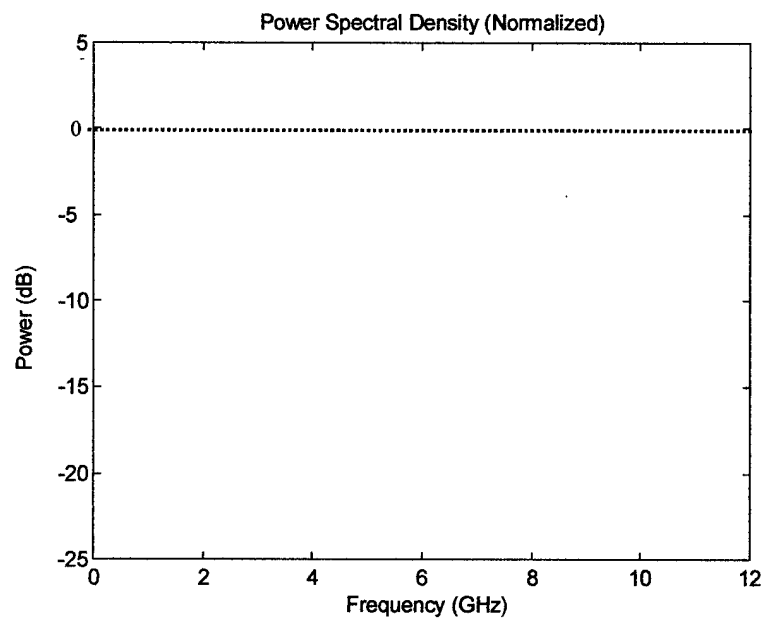


Figure 9. PSD for Ideal Impulse Input Pulse

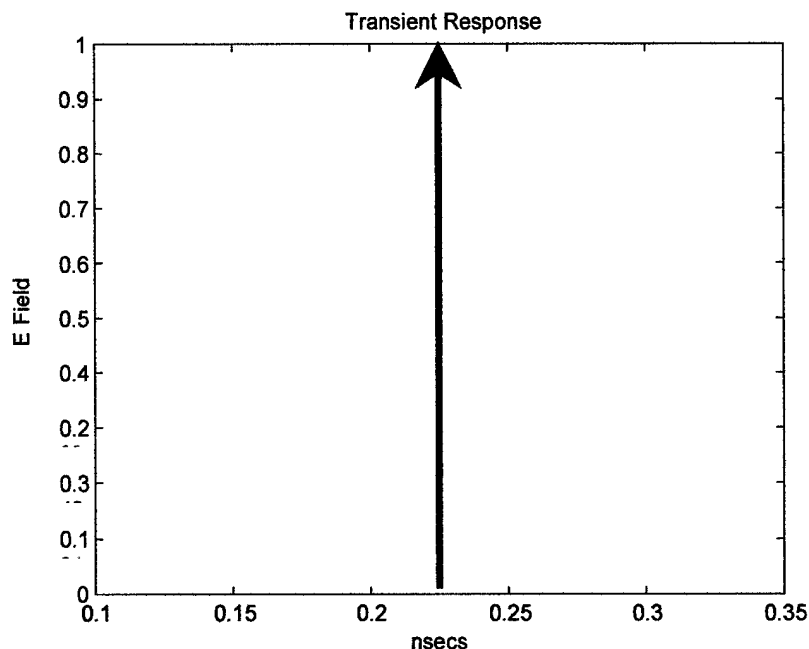


Figure 10. Ideal Input Pulse

TEM Horns and Transient Arrays

Single Element

It is well known that if a short pulse of electromagnetic energy is to be radiated out to long distances, while maintaining pulse fidelity, the TEM horn is an excellent choice of radiator. In addition to being robust and having a physically simple design, it displays low dispersion characteristics and high directionality. However, it is pointed out in [2], that to date, no full theoretical analysis of this type of structure has been accomplished. The paper goes on to describe how the simplest analyses assumes a TEM mode field in the aperture and open spaces along the sides of the horn that would exist if the horn were infinite in length, and neglects the modes due to reflections at the aperture end. Huygen's principle is then applied to predict the radiated field of the horn [2], [12]. Another analysis technique that has been applied makes use of a thin-wire V-antenna and

proceeds by performing a one-dimensional analysis. This method assumes a current on the antenna or solves for the current by a numerical method [13], [14].

Design Considerations

The TEM horn can be thought of as a TEM transmission line with almost constant impedance. Since the width-to-height ratio of the aperture determines the impedance of the antenna (or conversely the desired impedance determines the width-to-height ratio), it is necessary to maintain this ratio from the aperture to the feed. This allows the antenna to be matched to the feed. The increase in conductor spacing in the same proportion as the increase in the width of the plates gives it the constant impedance transition necessary to make the match between the feed line impedance and the desired antenna impedance. This gives rise to the triangle-shaped plates that are almost synonymous with TEM horns.

The height of the aperture determines, in two ways, the highest frequency that is able to propagate within the horn. Firstly, if the horn length is to remain constant, and any increase in height requires the width to increase (in order to maintain the width-to-height), then the path length from center of aperture to feed following the longitudinal edge also increases. This would be acceptable if it weren't for the fact that when the difference between this path length and the path length down the center of the horn results in a phase difference. When the difference in path lengths is greater than one-half the wavelength of all frequencies of operation, destructive interference results between components departing at different times. This manifests itself by decreasing the amplitude of the frequencies with wavelengths twice or greater than the difference in path lengths. The second aspect that reduces the high-frequency operation results from when the TM_{02} mode is excited. Applying parallel plate waveguide theory, the frequency will be inversely proportional to the height of the aperture. Thus the frequency that the TM_{02} mode will propagate at will decrease with an increase in aperture height. This becomes a design trade-off factor because some figures of merit improve with an increase in height, such as sensitivity [15].

A rough design equation for determining the high-frequency cut-off, f_{high} , at the -6dB point is

$$f_{high} = \frac{.604}{T} = \frac{(.604)c}{2L \sin^2\left(\frac{\beta}{2}\right)}. \quad (3)$$

The pulse duration, T , is determined by

$$T = \frac{L}{c} - \frac{L}{c} \cos \beta = \frac{2L}{c} \sin^2\left(\frac{\beta}{2}\right), \quad (4)$$

and the dimensions for the TEM horn shown in Figure 11 [1], [3].

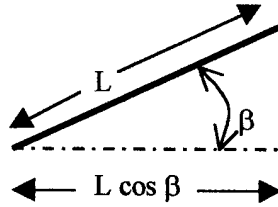


Figure 11. Determination of High Frequency Cutoff

The length of the horn's conducting plates determines the low frequency cut-off,

$$f_{co} = \frac{c}{2L}, \text{ where } c \text{ is the speed of light.} \quad (5)$$

The length, L , must be at least one-half wavelength long at the lowest frequency of interest. This insures a smooth transition from the transmission line to freespace [14].

The low frequency performance of the horn can be explained by modeling the horn as a transmission line. Looking at Figure 12, one sees the high-frequency model and its independence from frequency up to high frequency cut-off discussed above. The antenna appears as a resistive load and the coupling to the fields as a resistive source.

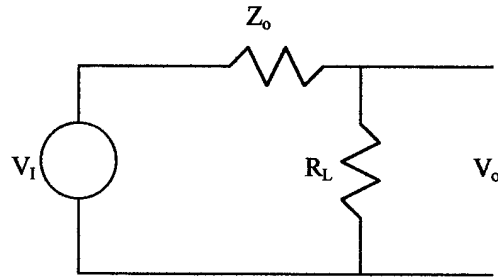


Figure 12. High Frequency Transmission Line
Model of TEM Horn

The TEM horn's low frequency model, shown in Figure 13, illustrates the low frequency dependence. The antenna responds like a voltage source with a capacitive load and its amplitude response is similar to that of a simple RC filter. By terminating the antenna with a capacitive load, frequency independence is gained [1].

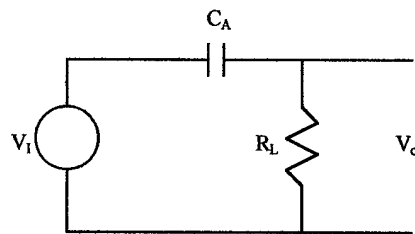


Figure 13. Low Frequency Transmission Line
Model of a TEM of Horn

Design Improvements

The authors in [1] advocate parallel plate extensions as a means of capacitively terminating the antenna to improve the low frequency performance. It was also determine experimentally in [1] that the optimum performance occurs when the ratio of extension area to the conducting plate area is 4 to 1.

Another problem experienced by these horns, due to their open circuit nature at low frequencies, is the reflection of the pulse back towards the source. For high power systems this could result in damaged sources. One solution given in [16] and [17] is a resistive termination loop that orients the electric and magnetic dipole moments so that their magnitudes and directions are matched. The low-frequency radiation is directed forward and the low-frequency radiation in the backward direction is canceled. The resulting antenna pattern has the familiar cardioid shape.

TEM horns are popular subjects for resistive loading or tapering. The abrupt changes in the characteristics between the lossy-TEM-horn plates and freespace cause dispersions and reflections. Each of which can adversely influence the operation of the antenna by redirecting energy in directions other than boresight. Several techniques for resistively loading an antenna have been employed to reduce these effects. In [1] the recommended method is cutting slots in the parallel extension and bridging these slots with ceramic chip or carbon resistors. The experimental horn used in [14] was made by sputtering copper on polycarbonate substrates. In [18], the optimum loading parameter was given as

$$Z'(z') = \frac{\alpha_0}{(1 - |z'|/L)} \left[\frac{\Omega}{m} \right] \quad -L \leq z' \leq L, \quad (6)$$

where α_0 is some critical value which causes an antenna to sustain a single wave of current.

In addition to the theoretical and experimental considerations discussed in the papers presented in the preceding paragraph, several published papers describe the exploration of resistively loaded antennas with the FDTD method [2], [19]. These

investigations have shown resistive loading to be an effective method for reducing reflection from pulse radiating antennas.

There is a price to pay for reducing reflections using this technique. The efficiency of the antenna is reduced considerable. An example provided in [20] and echoed in [3], describes the efficiency issue of this method. In the example the loading dissipated 88% of the incident pulse. In [3] the point is made that if pulse fidelity, in a low power application, is the most critical figure of merit, this method of reflection reduction is acceptable, but for high power applications the antenna might suffer heat damage due to the energy dissipation.

An alternative to resistive loading is presented in [3]. Linear and exponential tapered periodic surfaces (TPS) are applied to the ends of a TEM horn in an effort to reduce reflections and diffractions. This report demonstrated that TPSs reduced off boresight radiation and increased the peak-to-peak field on boresight.

Transient Arrays

The goal of more energy across a wider spectrum has driven researchers to arrays of TEM horns. There are several advantages that contribute to pursuit [21], [22].

1. The beam from a transient array can be steered by properly timing the application of pulses to individual elements.
2. Faster risetimes from multiple sources producing less voltage/source.
3. Mutual coupling between elements increases low-frequency performance.

A thorough development of the theory is given in [21], and [22] investigates the proper element arrangement. A third source investigates the use of sparse arrays to reduce the complexity and electronics required to produce UWB signals [23]. In [24], 2 and 4-element arrays of TEM horns are constructed in various configurations and numerically analyzed using the FDTD method. The studied concluded that the stacked horn configuration, shown on the right side of Figure 14, demonstrated significant

performance improvement over a single element. The *rain gutter* configuration, shown on the left, exhibited no contributions over the single element TEM horn. The authors attributed the enhanced performance of the stacked configuration to the charge cancellations that takes place between the element [24].

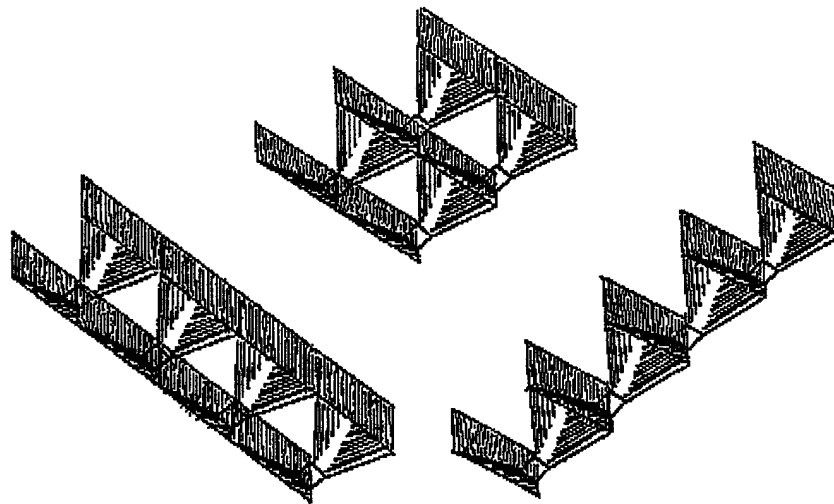


Figure 14. Various Configurations of Four
Element Arrays of TEM Horns

Time-Domain to Frequency-Domain and Back

Now that the benefits of UWB High Power Microwave DEW systems are understood as well as how UWB signals are generated and the requirements put on the signals, it is apparent why these systems are operated in the time-domain verses the frequency domain. The problem now is that much of the antenna theory and analysis

techniques developed and understood to date concern antennas operated in the frequency domain. One can, of course, pick a single frequency and apply the Fourier transform relationship between the time domain waveform $f(t)$, given by

$$f(t) = \frac{1}{2\pi} \int_{-\infty}^{\infty} F(\omega) \exp(j\omega t) d\omega, \quad (7)$$

and its spectrum, $F(\omega)$, where

$$F(\omega) = \int_{-\infty}^{\infty} f(t) \exp(-j\omega t) dt. \quad (8)$$

This must be done for each frequency of interest and becomes a cumbersome feat in mathematical manipulations when the different frequencies of interest range into the thousands. This method is often referred to as wide-band analysis. Fortunately the Fast Fourier Transform (FFT), based on a discrete Fourier transform, allows an easy go between. Now a numerical method is needed to determine the time-domain electromagnetic responses to these types of problems [11].

Finite-Difference Time-Domain Method

A method to fill this need was first proposed over thirty years ago. In 1966 Yee [25] described a simple, yet elegant routine for incrementally time stepping electromagnetic fields through a grid. This numerical method was affectionately dubbed the Finite-Difference Time-Domain (FDTD) method by its followers. In its infancy, the FDTD method did not spawn much interest. The major problem it suffered from was that the medium of operation was also in its own infancy. Computational costs of the day were the major limiting factor. Using the growth in the number of publications concerning FDTD in recent years as a measuring stick, it is evident that the advances seen in computing power have also been realized by the FDTD method [26].

A thorough literature review of the FDTD method is presented in [26]. Only the articles that have direct relevance to the research presented in this report, along with a very quick look at the method itself, are highlighted. The reader is referred to [26] for further reading on the published applications and improvements to the FDTD method.

The following description gives the basic idea behind the popular Yee FDTD algorithm. The algorithm uses a set of finite-difference equations for the time-dependent Maxwell's curl equations, given as

$$\frac{\partial H_x}{\partial t} = \frac{1}{\mu} \bullet \left(\frac{\partial E_y}{\partial z} - \frac{\partial E_z}{\partial y} - \rho' H_x \right), \quad (9)$$

$$\frac{\partial H_y}{\partial t} = \frac{1}{\mu} \bullet \left(\frac{\partial E_z}{\partial x} - \frac{\partial E_x}{\partial z} - \rho' H_y \right), \quad (10)$$

$$\frac{\partial H_z}{\partial t} = \frac{1}{\mu} \bullet \left(\frac{\partial E_x}{\partial y} - \frac{\partial E_y}{\partial x} - \rho' H_z \right), \quad (11)$$

$$\frac{\partial E_x}{\partial t} = \frac{1}{\varepsilon} \bullet \left(\frac{\partial H_y}{\partial z} - \frac{\partial H_z}{\partial y} - \sigma E_x \right), \quad (12)$$

$$\frac{\partial E_y}{\partial t} = \frac{1}{\varepsilon} \bullet \left(\frac{\partial H_z}{\partial x} - \frac{\partial H_x}{\partial z} - \sigma E_y \right), \text{ and} \quad (13)$$

$$\frac{\partial E_z}{\partial t} = \frac{1}{\varepsilon} \bullet \left(\frac{\partial H_x}{\partial y} - \frac{\partial H_y}{\partial x} - \sigma E_z \right) \quad (14)$$

to solve for both the electric and magnetic fields in time and space.

The algorithm centers its \mathbf{E} and \mathbf{H} components in the three-dimensional space so that every \mathbf{E} component is surrounded by four circulating \mathbf{H} components, and every \mathbf{H} component is surrounded by four circulating \mathbf{E} components as shown in Figure 15. One of the major benefits to this arrangement is that continuity of the tangential \mathbf{E} and \mathbf{H} fields are maintained across an interface of dissimilar materials as long as the interface is parallel to one of the grid coordinate axes.

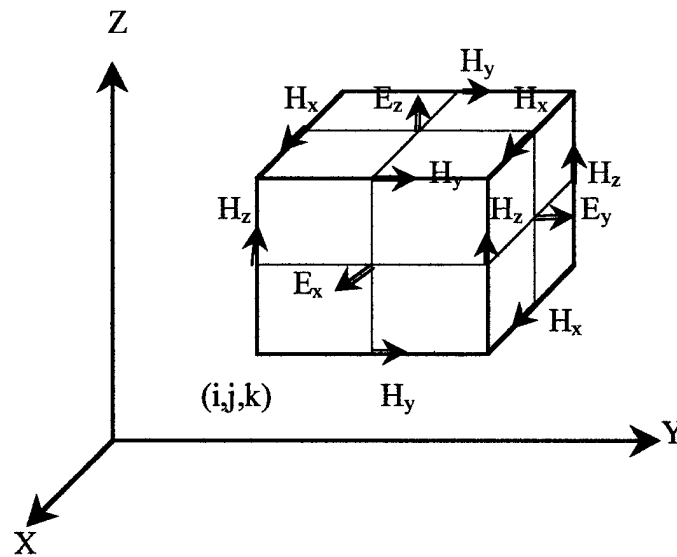


Figure 15. Field Vector Components in FDTD Cell

The time components of the E and H fields are also arranged in a staggered fashion. This creates the *leapfrog* effect, which allows the E field components to be computed from the H components previously calculated and, in turn, the H components from the E components just calculated. This cycle is repeated until the predetermined stop time [27].

A descriptive derivation of the numerical approximation of Maxwell's curl equations is given in [27], and the results presented in the following equations;

$$H_x \Big|_{i,j,k}^{n+1/2} = \left(\frac{1 - \frac{\rho'_{i,j,k} \Delta t}{2\mu_{i,j,k}}}{1 + \frac{\rho'_{i,j,k} \Delta t}{2\mu_{i,j,k}}} \right) H_x \Big|_{i,j,k}^{n-1/2} + \left(\frac{\frac{\Delta t}{\mu_{i,j,k}}}{1 + \frac{\rho'_{i,j,k} \Delta t}{2\mu_{i,j,k}}} \right) \left(\frac{E_y \Big|_{i,j,k+1/2}^n - E_y \Big|_{i,j,k-1/2}^n}{\Delta z} - \frac{E_z \Big|_{i,j+1/2,k}^n - E_z \Big|_{i,j-1/2,k}^n}{\Delta y} \right), \quad (16)$$

$$H_y \Big|_{i,j,k}^{n+1/2} = \left(\frac{1 - \frac{\rho'_{i,j,k} \Delta t}{2\mu_{i,j,k}}}{1 + \frac{\rho'_{i,j,k} \Delta t}{2\mu_{i,j,k}}} \right) H_y \Big|_{i,j,k}^{n-1/2} + \left(\frac{\frac{\Delta t}{\mu_{i,j,k}}}{1 + \frac{\rho'_{i,j,k} \Delta t}{2\mu_{i,j,k}}} \right) \left(\frac{E_z \Big|_{i+1/2,j,k}^n - E_z \Big|_{i-1/2,j,k}^n}{\Delta x} - \frac{E_x \Big|_{i,j,k+1/2}^n - E_x \Big|_{i,j,k-1/2}^n}{\Delta z} \right), \quad (17)$$

$$H_z \Big|_{i,j,k}^{n+1/2} = \left(\frac{1 - \frac{\rho'_{i,j,k} \Delta t}{2\mu_{i,j,k}}}{1 + \frac{\rho'_{i,j,k} \Delta t}{2\mu_{i,j,k}}} \right) H_z \Big|_{i,j,k}^{n-1/2} + \left(\frac{\frac{\Delta t}{\mu_{i,j,k}}}{1 + \frac{\rho'_{i,j,k} \Delta t}{2\mu_{i,j,k}}} \right) \left(\frac{E_x \Big|_{i,j+1/2,k}^n - E_x \Big|_{i,j-1/2,k}^n}{\Delta y} - \frac{E_y \Big|_{i+1/2,j,k}^n - E_y \Big|_{i-1/2,j,k}^n}{\Delta x} \right), \quad (18)$$

$$E_x \Big|_{i,j,k}^{n+1} = \left(\frac{1 - \frac{\sigma_{i,j,k} \Delta t}{2\varepsilon_{i,j,k}}}{1 + \frac{\sigma_{i,j,k} \Delta t}{2\varepsilon_{i,j,k}}} \right) E_x \Big|_{i,j,k}^n + \left(\frac{\frac{\Delta t}{\varepsilon_{i,j,k}}}{1 + \frac{\sigma_{i,j,k} \Delta t}{2\varepsilon_{i,j,k}}} \right) \left(\frac{H_z \Big|_{i,j+1/2,k}^{n+1/2} - H_z \Big|_{i,j-1/2,k}^{n+1/2}}{\Delta y} - \frac{H_y \Big|_{i,j,k+1/2}^{n+1/2} - H_y \Big|_{i,j,k-1/2}^{n+1/2}}{\Delta z} \right), \quad (19)$$

$$E_y \Big|_{i,j,k}^{n+1} = \left(\frac{1 - \frac{\sigma_{i,j,k} \Delta t}{2\varepsilon_{i,j,k}}}{1 + \frac{\sigma_{i,j,k} \Delta t}{2\varepsilon_{i,j,k}}} \right) E_y \Big|_{i,j,k}^n + \left(\frac{\frac{\Delta t}{\varepsilon_{i,j,k}}}{1 + \frac{\sigma_{i,j,k} \Delta t}{2\varepsilon_{i,j,k}}} \right) \left(\frac{H_x \Big|_{i,j,k+1/2}^{n+1/2} - H_x \Big|_{i,j,k-1/2}^{n+1/2}}{\Delta z} - \frac{H_z \Big|_{i+1/2,j,k}^{n+1/2} - H_z \Big|_{i-1/2,j,k}^{n+1/2}}{\Delta x} \right), \quad (20)$$

and

$$E_z \Big|_{i,j,k}^{n+1} = \left(\frac{1 - \frac{\sigma_{i,j,k} \Delta t}{2\varepsilon_{i,j,k}}}{1 + \frac{\sigma_{i,j,k} \Delta t}{2\varepsilon_{i,j,k}}} \right) E_z \Big|_{i,j,k}^n + \left(\frac{\frac{\Delta t}{\varepsilon_{i,j,k}}}{1 + \frac{\sigma_{i,j,k} \Delta t}{2\varepsilon_{i,j,k}}} \right) \left(\frac{H_y \Big|_{i+1/2,j,k}^{n+1/2} - H_y \Big|_{i-1/2,j,k}^{n+1/2}}{\Delta x} - \frac{H_x \Big|_{i,j+1/2,k}^{n+1/2} - H_x \Big|_{i,j-1/2,k}^{n+1/2}}{\Delta y} \right). \quad (21)$$

If the computational volume is divided into cubic cells, then $\Delta x = \Delta y = \Delta z = \Delta$, and Δt , in order to guarantee stability, is chosen to satisfy Courant stability condition

$$\Delta t \leq \frac{\Delta}{c\sqrt{3}}, \quad (15)$$

where c is the speed of light [28].

The notation in the above equations is most easily describe with

$$u(i\Delta x, j\Delta y, k\Delta z, n\Delta t) = u_{ij,k}^n \quad (22)$$

where u is any function, Δx , Δy , and Δz are the space increments, i , j , and k are integers, Δt is the time increment, and n is an integer. This equation represents a function of space and time evaluated at a discrete point in the grid and at a discrete point in time [27].

Application Found In Literature

Now that a quick look at the FDTD method has been presented, attention is redirected back to some of its applications found in the literature. One of the first FDTD looks at antennas was reported in [29]. In this report two- and three-dimensional waveguides, flared horns, a two-dimensional parabolic reflector, and a two-dimensional hyperthermia application were studied and the results compared to results from the method of moments. In [30] Vivaldi flared antennas were studied using FDTD, as well as arrays Vivaldi of antennas. This work achieved a number of firsts; the first *exact* computational model of a single quad Vivaldi slot antenna; the first *exact* computational model of a phased array of Vivaldi quad elements; and the first FDTD model to demonstrate grating lobes for a phased array antenna of any sort.

The authors in [31] studied the implications of the staircase representation created when the conductor of a TEM does not lie in a single plane of a Cartesian grid. By comparing the FDTD results to those of the analytic solution, they established a rule-of-thumb for how the coarseness of the grid representation influences the results. Their rule-of-thumb as stated is "...staircasing errors are small when the staircase diagonal (the hypotenuse of the right triangle created by the stairstep) is smaller than half a wavelength at the highest significant frequency in the excitation."

In [2] several TEM horn designs are analyzed with the FDTD method. The results are compared to the experimental data that exists for each design. Their conclusion is that the FDTD method provides an accurate analyzes tool for these types of

problems. One of the horns analyzed was design to continuously change the characteristic impedance of the equivalent transmission line over the length of the antenna by shaping the conducting plates. The intentions of this design were to set the feed-end impedance equal to the feeding transmission line and the aperture end to the wave impedance of free space in order to reduce reflections. Additionally, the original designers added a resistive pad at to the end of the horn. During the FDTD study the simulations were conducted with and without the pad. Their conclusion was that the plate shaping did not reduce reflections and that the resistive pad was successful. What they did not show, at least in the article, is what effect the shaping did have on the output. This design is discussed further in the next section.

Plate Shaping and Exponential Tapers

Designers call the horn discussed in the previous section a tapered impedance traveling-wave antenna (TWIT), and put it in a class of radiators labeled “non-uniform propagating systems [13].” The top and side view of the TWIT are shown in Figure 16.

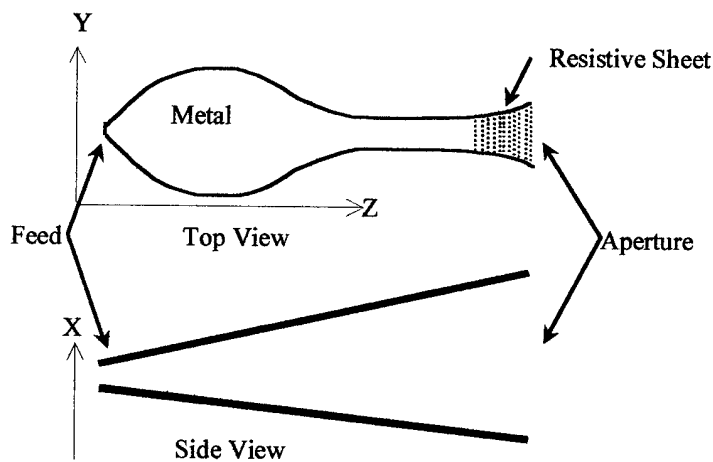


Figure 16. The Top and Side View of the TWIT

The authors, supported with the theory developed in [32], develop the theory and design equations used in the design of the TWIT. They give a good description of the

antenna in the paper and then report on the experimental results. As with the FDTD simulation of this design, the authors do not quantify the effects of the taper design. They only compared it to the results of the runs with the resistive pad.

One paper does report on the effects of applying only a taper to the plates of a TEM horn. In [33] two tapered plate configuration are compared experimentally. The tapers used in the comparison are based on the impedance seen at the aperture.

Optimization of the tapers to reduce reflection is a topic of interest in [13], [32], and [33]. The approach in each is either experimental or theoretical in nature. What if the optimum taper could be designed on the fly? What if reflections could be reduced and the answer wasn't tapering in one direction only? These are questions that motivate the next section.

Optimization Routines and FDTD

Interest has been expressed in taking advantage of the computing power available and taking FDTD to a new level. This level involves interfacing FDTD with some type of optimizing routine, such as a genetic algorithm to accentuate some feature of an UWB antenna. Unfortunately, depending on the size of the problem, FDTD runs can be very time consuming. This, combined with the fact that optimizing routines generally require many iterations, each with an associated run time, prohibits the prospect of a union unless something is done to reduce the FDTD run time.

Past efforts have demonstrated the ability to interface a computational electromagnetic engine, a method of moments (MoM) code, with an evolutionary algorithm (EA). The case in point was able to design an optimal wire antenna for performance at low elevation angles in the presence of a lossy half-space [34]. In this application of an EA speed was not a hampering factor. The MoM code was able to perform its computations and deliver a solution to the EA in at the most a few minutes.

To demonstrate the time involved a quick and simple example is given: If a MoM run took 1 minute to produce and deliver an answer to the EA, resulting in the entire process taking one hour to obtain an optimum solution, an acceptable period of operation is achieved. Increasing the process of delivering of an answer to the EA to 24 hours would increase the entire process of producing an optimum solutions to 60 days. This was beyond the reach of this effort.

The FDTD method has 2 apparent time drivers; the size of the computational problem, and processor speed. The FDTD method lends itself readily to parallel processing, so a solution exists for the latter. If increasing the processing speed is not an option, one must turn toward the former for a solutions. The following are areas where solutions may be found:

1. Number of time-steps
2. Size of object under investigation
3. Grid cell size
4. Area external to the object
5. Computer memory available

The run-time can be reduced just by carefully specifying what is desired from a simulation. For instance, if only the early time response is desired, the number of time-steps can be reduced. In the case of the size of the object, the use of image planes is a possibility. The standard for determining the grid resolution is 10 cells/wavelength of the highest significant frequency [27], so by determining the bandwidth of interest a larger cell size maybe an option. If only the near-field response is required, the computational area only needs to include the object and the point at which the fields are desired. This same volume can be used to determine far-fields using near-to-far field transforms, which are easily integrated into the FDTD method. Each of the first four in the list, besides driving the number of computations, also drives the amount of memory required.

In the FDTD method, the fields, shown in Figure 15, must be computed at each time step for each space location and stored for calculations at the next time step, at which time they can be discarded. If the internal memory reserve does not allow the entire problem to be stored at once, the processor must resort to writing to and reading from external memory (virtual memory). The process adds additional time to the total run time.

The examples provided above are not all-inclusive. Basically it is a list of things controllable by the user. There are other methods that increase the computational efficiency, which are already incorporated into commercial codes.

Chapter Review

This chapter gives an overview of the topics encountered in this research effort. The use of UWB signals and the requirements put on them are discussed in some detail as are the TEM horns and arrays used to radiate these types of signals. A cursory look at the FDTD method was presented along with current applications of the method. Application of tapered plates to TEM horns was gleaned over. The chapter wrapped up by posing the problem of interfacing an EA with the FDTD method.

Because of the numerical nature of this research topic, the theory presented was intentionally sparse. Again, the reader is encouraged to visit the bibliography for additional information.

Chapter 3: Methodology

This chapter describes the design and development of the models. Because the study is concerned primarily with the differences between the models and the results these differences produce in the output, a lot of time is spent describing the process of model generations. The input pulses are described with focus on the experimental pulse, which requires some alterations. Some of the other input parameters required by TSAR are also described as well as the data collection process. A quick look at theory behind the near-to-far transform used in this code is presented. The chapter wraps up with a look at the methods used to reduce the run-times and the analysis techniques.

Descriptions of Antennas and Models

The antennas under investigation are two dimensionally different variations of the same TEM horn. The dimensions of the horns were specified in advance by the sponsoring agency. Experimental data exists for the large double-linear tapered horn and its arrays. A slight modification to the two and four-element arrays of this horn were required in order to more closely model the experimental arrays, thus there are two versions of the large double-linear taper two and four-element arrays. Details of the modification and the reason for it will be provided later. A top view and side view of the basic TEM horn is shown in Figure 17 and Figure 18, respectively, with the corresponding dimensions provided in Table 1.

Table 1. Summary of Horn Dimensions

		Horn 1 (Large Horn)	Horn 2(Small Horn)
Length	L	0.2975 m	0.0300 m
Aperture Width	W_a	0.3000 m	0.0300 m
Feed Width	W_f	0.0760 m	0.0100 m
Aperture Height	H_a	0.0760 m	0.0300 m
Feed Height	H_f	0.0190 m	0.0100 m

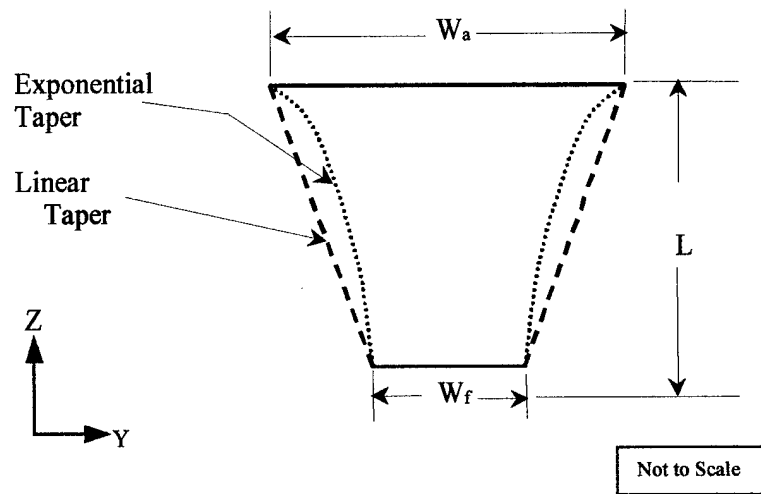


Figure 17. Top View TEM Horn

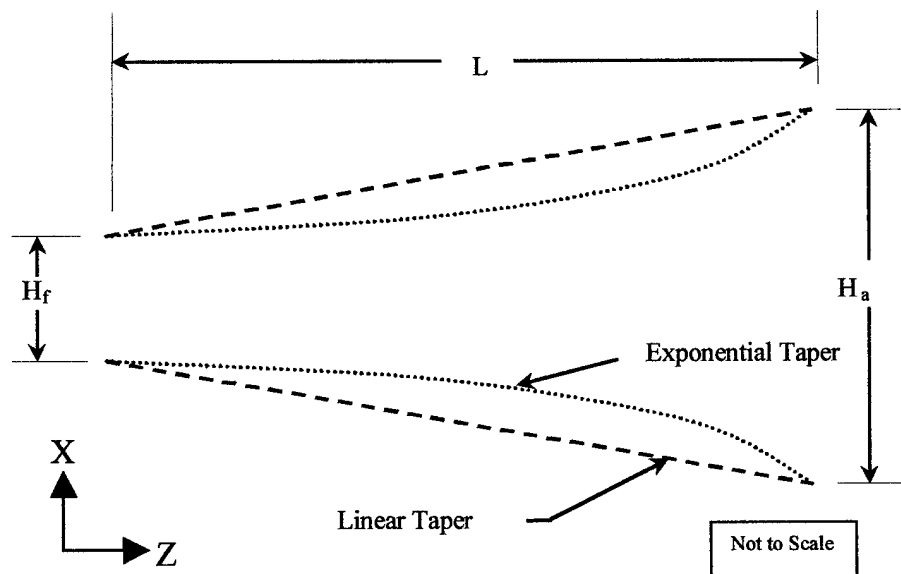


Figure 18. Side View TEM Horn

Exponential Taper Design

The x-directed (height direction) exponential taper in each case is determined by

$$H(z) = \frac{H_f}{2} \exp \left\{ \frac{z}{L} \ln \left(\frac{H_a}{H_f} \right) \right\}. \quad (23)$$

Similarly, the y-directed (width direction) exponential taper is calculated with

$$W(z) = \frac{W_f}{2} \exp \left\{ \frac{z}{L} \ln \left(\frac{W_a}{W_f} \right) \right\}. \quad (24)$$

Model Generation

Creating the CAD Model

Before continuing with the development of the specific research models, it is necessary to understand how objects are created using the MGED portion of the BRL-CAD package. The brief explanation that follows was extracted from the MGED User's Manual [35].

In BRL-CAD objects are constructed using a technique known as "Combinatorial Solid Geometry" or "Constructive Solid Geometry" or simply "CSG". This technique involves creating objects by combining primitive shapes together to form complex objects. The primitive shapes are called "solids". Each one occupies a volume of three-dimensional space... These primitives can be combined using Boolean operators to create complex shapes. The three Boolean operations supported are union, difference (or subtraction), and intersection. Any number of primitives may be combined to produce a shape. The union (u) of two solids is defined as the volume in either of the solids. The difference (-) of two solids is the volume of the first solid which is not in the volume of the second solid. The intersection (+) of two solids is the volume that is contained in both solids. The result of performing a set of Boolean operations is a new shape. The new shape is known as a "combination". When the desired shape of an object is attained, a special combination called a "region" is created. A "region" represents an actual material component of the model. It represents an item which is made from a homogeneous type of material.

For a simple example of creating a hollow cylinder, with a skin thickness of 2 units, you would specify two solid concentric cylinders. The outer cylinder would have a radius 2 units larger than the inner. You would then create the hollow cylinder by subtracting the inner cylinder from the outer.

Setting Material Properties

If the scattering properties of this cylinder were to be analyzed with TSAR, you would have to define it as a region and create the link that allows you to set the material properties in TSAR. This link is created by using MGED's "mater" command and setting the material property to fd=M, where M is an integer. TSAR then lets you set the material properties of material M. If you have more than 1 material, say a cylinder coated in radar absorbing material, in MGED you would specify a different fd number for each material. In TSAR you specify the material properties such as conductivity, permittivity, and permeability. If no properties are set for a material, they default to freespace values. For the purpose of this research effort, the antennas conducting elements are assumed to be perfect electric conductors(PEC). This is accomplished within TSAR by setting the electric conductivity, σ , to approximately infinity. Past researchers have set the electric permittivity, ϵ , to a specific value when simulating PEC conducting plates [24], but this is unnecessary. A quick look at one of the E Field FDTD equations reveals that $\sigma \approx \infty$ dominates the ϵ term and the updated E field is the negative of the previous time step (the response to a PEC boundary) [30]. Observing the FDTD equation,

$$E_x^{n+1}_{i,j,k} = \left(\frac{1 - \frac{\sigma_{i,j,k} \Delta t}{2\epsilon_{i,j,k}}}{1 + \frac{\sigma_{i,j,k} \Delta t}{2\epsilon_{i,j,k}}} \right) E_x^n_{i,j,k} + \left(\frac{\frac{\Delta t}{\epsilon_{i,j,k}}}{1 + \frac{\sigma_{i,j,k} \Delta t}{2\epsilon_{i,j,k}}} \right) \left(\frac{H_z^{n+1/2}_{i,j+1/2,k} - H_z^{n+1/2}_{i,j-1/2,k}}{\Delta y} - \frac{H_y^{n+1/2}_{i,j,k+1/2} - H_y^{n+1/2}_{i,j,k-1/2}}{\Delta z} \right), \quad (25)$$

illustrates this point.

Development of the Double-Linear Models

Similar to the hollow cylinder example, the double-linear taper model was generated by creating two collocated solids. The inner solid is fashioned to have the same dimensions as the feed and aperture. This is shown in Figure 19.

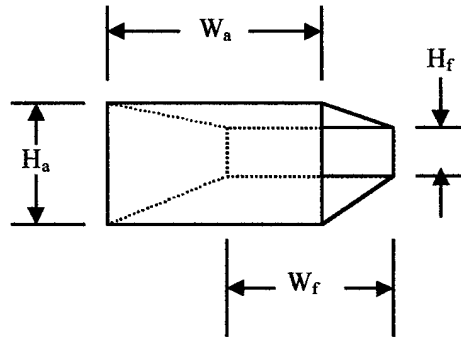


Figure 19. Inner-Solid Used to Form
TEM Horn in MGED

The width is maintained on the second solid but the height is increased in both directions. This increase is dependent on the cell size that is going to be used for the meshing process, and should be one to two cells thick. Once the outer solid is created, the inner is subtracted from the outer leaving a void. The subsequent solid becomes the conducting plates of the horn. The resulting plates are shown in Figure 20. To generate the 4-element array the new solid is copied and translated, in the height direction, to the pre-determined location of the element. This is repeated 2 more times for the other elements, and the original shifted half the horn's height so that boresight of the array is located at the origin. It is not necessary to create a 2-element array for analyzes. The 4-element configuration is utilized for this purpose by only exciting the two inner elements. The 4-element array is shown in Figure 21.

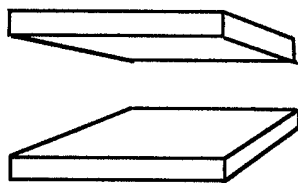


Figure 20. MGED Solid Representation of
Double-Linear TEM Horn

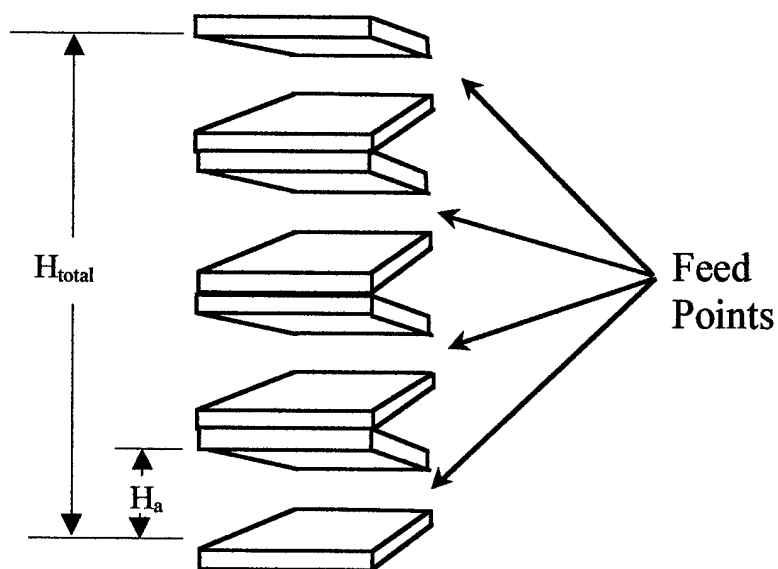


Figure 21. MGED Representation of Four-Element
Array of TEM Horns – First Version

The configuration shown in Figure 21 does not accurately model the array used to produce the experimental data. The experimental 4-element array was designed so that the total aperture height, H_{total} , was approximately 0.3 m. The total height will be

approximately 0.3 m only when the thickness of the plates is ≈ 0 . In the case shown above, with a plate thickness of 5 mm (5mm is determined by the mesh cell size), H_{total} is ≈ 33 cm. In a effort to reduce H_{total} , the model was redrawn as shown in Figure 22. This reduces H_{total} , to 31.5 cm. This is the closest approximation that can be achieved with a 5mm-cell size. The redrawn large double-linear taper array is used for the experimental comparisons and the reduction of run-time study. All the other comparisons are conducted with the first version, except the one presented in Figure 23. This illustrates how the time-domain response is influenced by height variations.

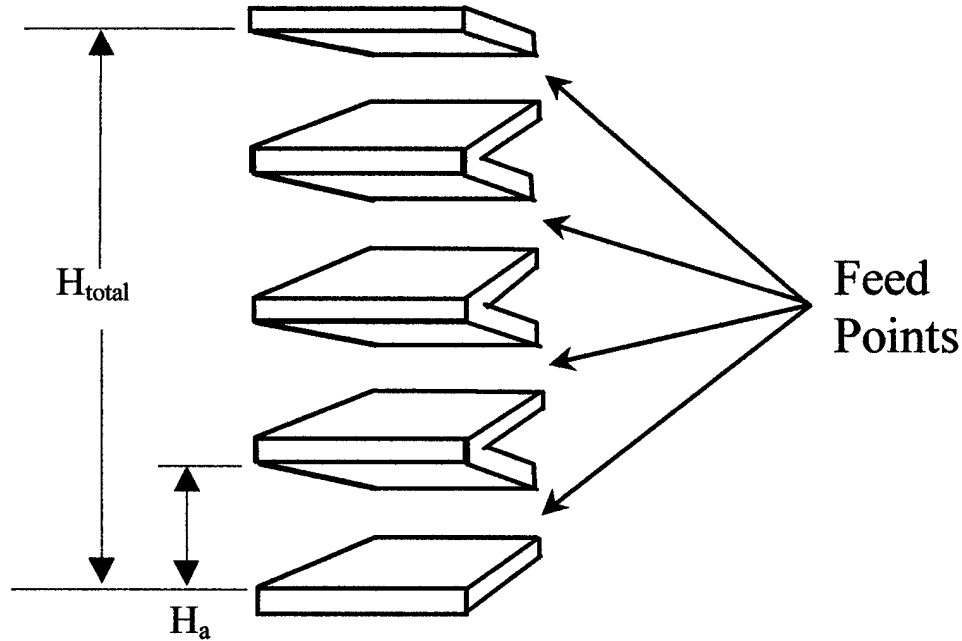


Figure 21. MGED Representation of Four-Element
Array of TEM Horns – Redrawn Version

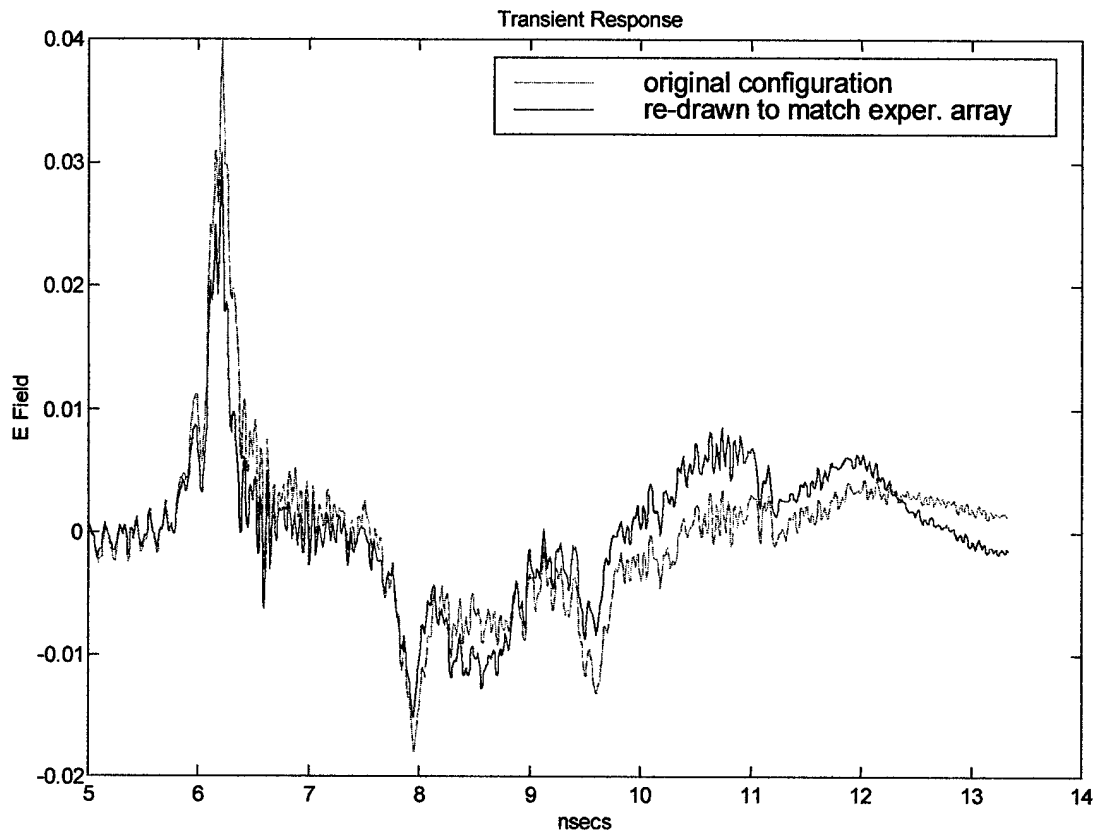


Figure 22. First Version Transient Responses vs.
Redrawn Version (Version Two)

Development of Y-Directed (Width) Exponential Taper Horn

The exponential curve applied to the width of the horn, as shown in Figure 17, was determined from Equation 24. The end points of this curve, along with one additional point from curve, were placed into the equation for a circle. This provided three equations with three unknowns, resulting in the equation of a circle whose curvature matches the curvature of the exponential curve. The center point's coordinate location and radius became the bases for a cylinder. The height of the cylinder is dependent on the total external height dimensions of the horn or array. The cylinder is created in

MGED and subtracted from both sides of the horn. An illustration of this procedure as applied to one side of the single horn is shown in Figure 23.

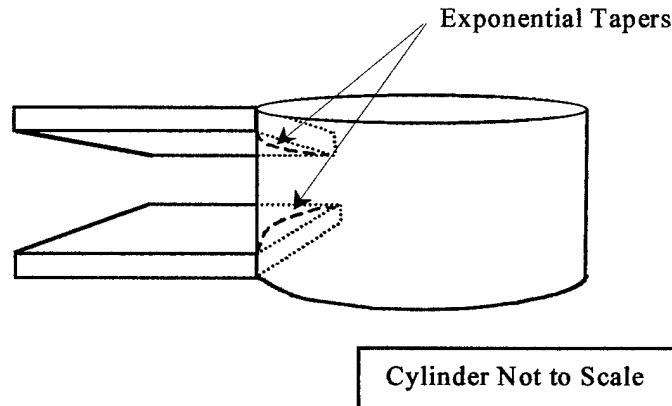


Figure 23. MGED Method of Y-Directed
Exponential Taper Construction

Development of X-Directed (Height) Exponential Taper Horn

The exponential curve applied to the height of the horn, shown in Figure 18, was determined from Equation 23. Following the procedure developed above, 2 pairs of concentric cylinders are developed in MGED, one pair above the y-z plane and one below. The radius of the outer cylinder correlates to the aperture and feed heights and the inner radius is one or two cells less. The inner cylinder is subtracted from the outer, leaving a hollow cylinder. The length of the cylinder is unimportant as long as it is greater than the width of the horn and parallel to the y-axis. Using the outer solid developed in the double-linear case, an intersection is created between the two hollow cylinders and the solid. The result is two exponentially curved plates with the correct dimensions and an exponential flare. A side view is given in Figure 24. The plates are highlighted with bold lines.

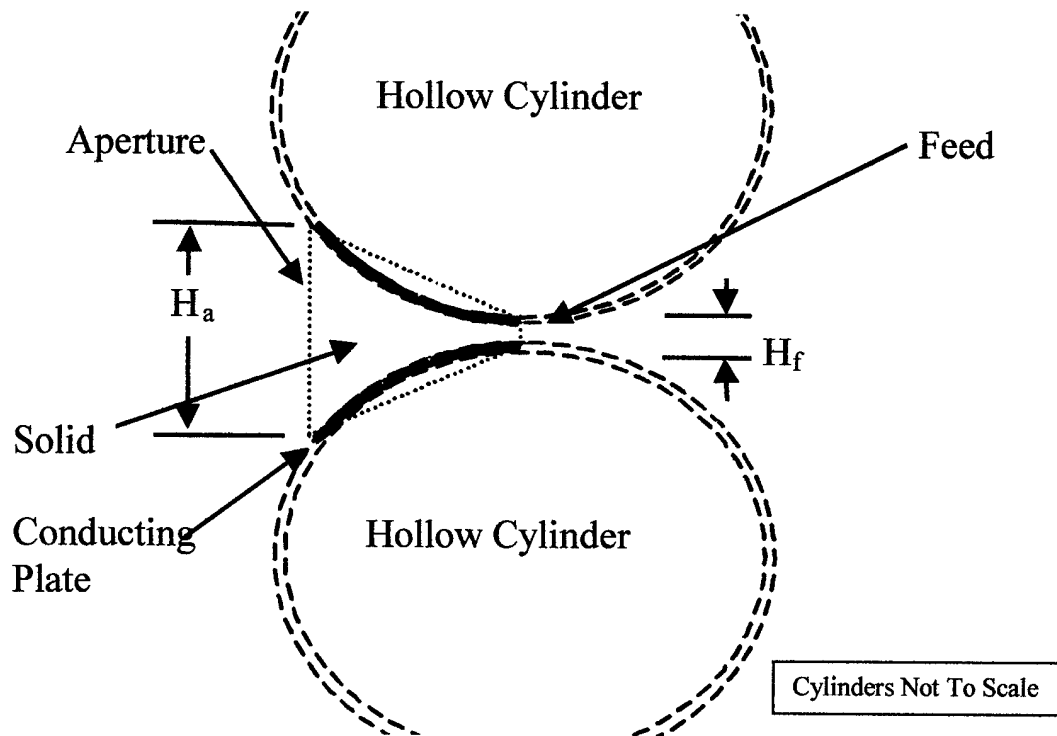


Figure 24. MGED Method of X-Directed Exponential
Taper Construction – Side View

Development of Double-Exponential Taper Horn

Just as the name applies this horn is a combination of the two previously discussed horns. The method of MGED development is also the combination of the two processes. The two cylinders that were calculated for and applied to the double-linear model to generate the y-directed exponential model are applied in the same manner to the x-directed model. This creates the double-exponential model, and completes the model development. The exact procedure is followed to generate the set of smaller horns.

Meshing

The meshing is accomplished with Anastasia (Ana). Ana was specifically developed to generate three-dimensional finite-difference meshes from the solid models generated with MGED. The output files are in the ASCII Cell I/O format used by

TSAR. The process is relatively automated, and only requires the user to specify a few parameters. Everything is kept constant throughout this process with the exception of cell size and bounding volume.

Determination of Cell Size

Size of object, details of the object, run-time, frequency content of the excitation pulse, and available computer memory are all issues involved in determining a suitable cell size. Ideally, the smallest grid size possible should be used. The criteria most often touted as being a determiner of grid resolution, in order to avoid numerical phase errors, is $\Delta = \lambda_0/10$.

Originally, the largest antenna under consideration, the large 4-element array, was meshed at a grid resolution of 10mm, 7mm, and 5mm. The concern was that the 5mm grid would result in prohibitive run-times. Results and run-times from three mesh sizes were compared. A comparison of the transient responses exhibited slight differences, especially in late time response and amplitude as illustrated in Figure 25. Since the run times were manageable and the computational resources available, combined with the fact that the smaller cell size is theoretically more accurate, it was determined that the 5mm grid would be used for the larger horn grid.

Because of the physical size of the smaller horn, it was easier to determine the cell size. A cell size of 5mm would only allow the horn to be modeled with 6 cells in the lengthwise direction; far too few for an accurate model. A 2mm grid was considered, but again the resources allowed for the finest grid possible, 1mm.

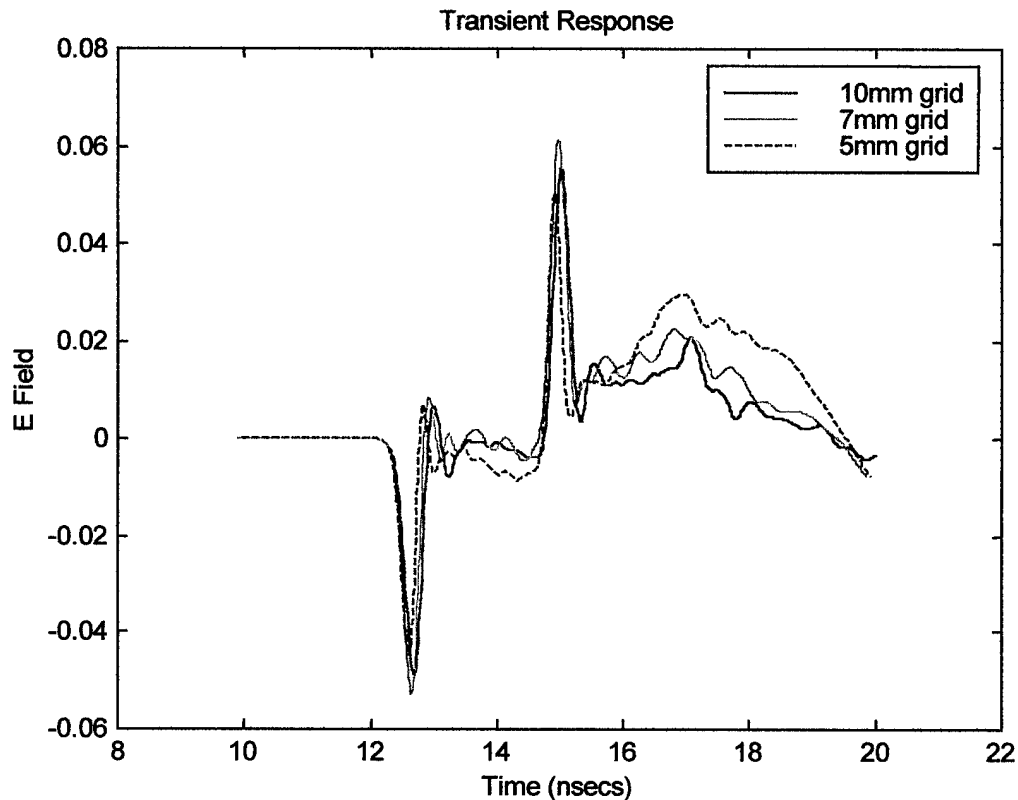


Figure 25. Transient Responses for 5mm, 7mm, and 10mm Grid Resolutions

Figures 26 - 37 shows the meshed models used during this research effort. Figure 33 and Figure 34 give a good illustration of the difference between the verification version and the test model version.

Every effort was made to keep the models independent of variations, especially dimensional variations. The mesh viewer, Image, was used to zoom in on the apertures and feeds of each horn to insure the meshed model met the desired specifications. In addition to dimension verification, Image was used to determine the location of the source within the feed.

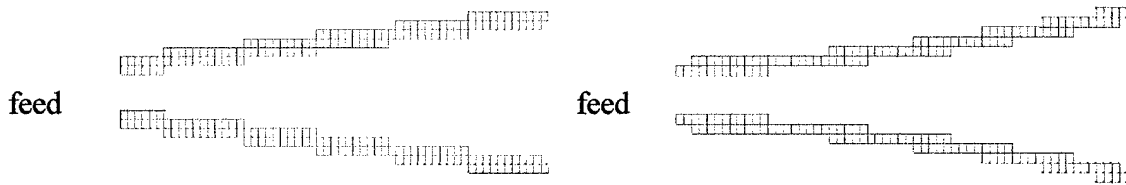


Figure 26. Meshed Model, Side View, Large Horn, X-Directed Linear Taper(left),
X-Directed Exponential Taper (right)

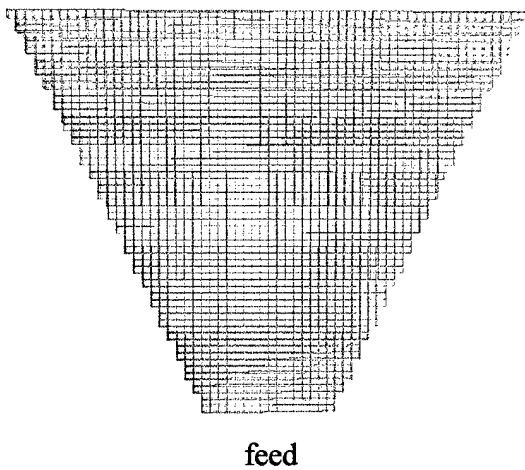


Figure 27. Meshed Model, Top View, Large
Horn, Y-Directed Linear Taper

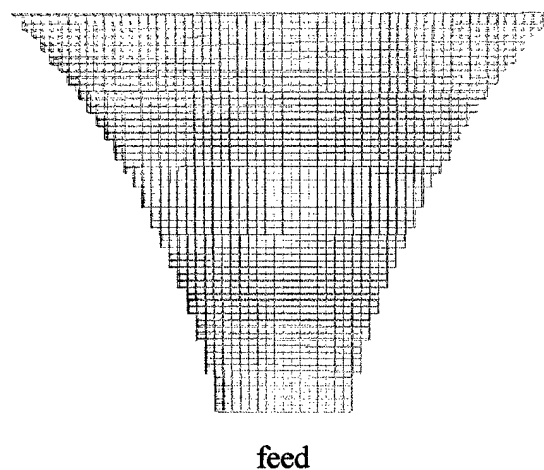


Figure 28. Meshed Model, Top View, Large
Horn, Y-Directed Exponential Taper

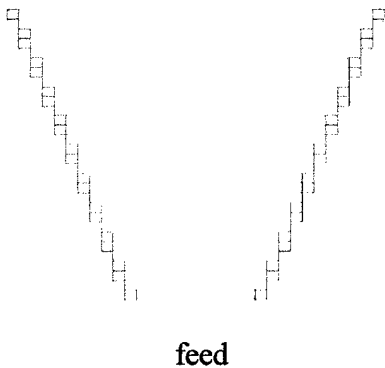


Figure 29. Meshed Model, Side View, Small
Horn, X-Directed Linear Taper

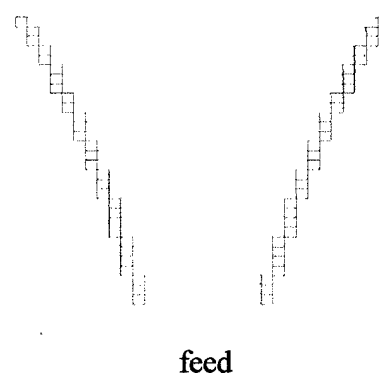
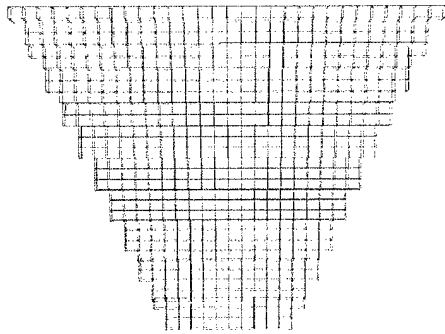
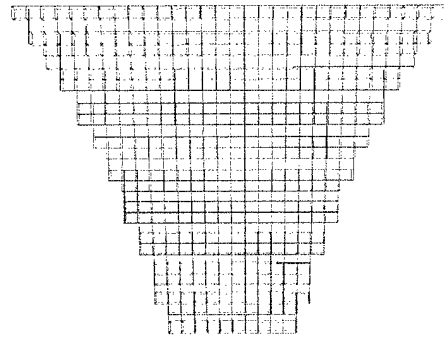


Figure 30. Meshed Model, Side View, Small
Horn, X-Directed Exponential Taper



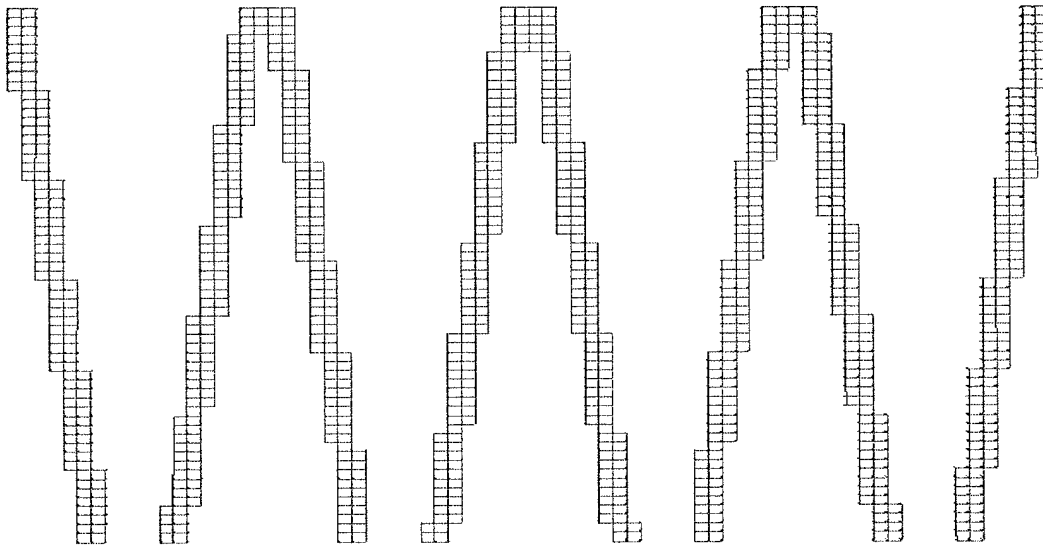
feed

Figure 31. Meshed Model, Top View, Small
Horn, Y-Directed Linear Taper



feed

Figure 32. Meshed Model, Top View, Small
Horn, Y-Directed Exponential Taper



feed

feed

feed

feed

Figure 33. Meshed Model, Side View, Large
4-Element Array, Linear Taper

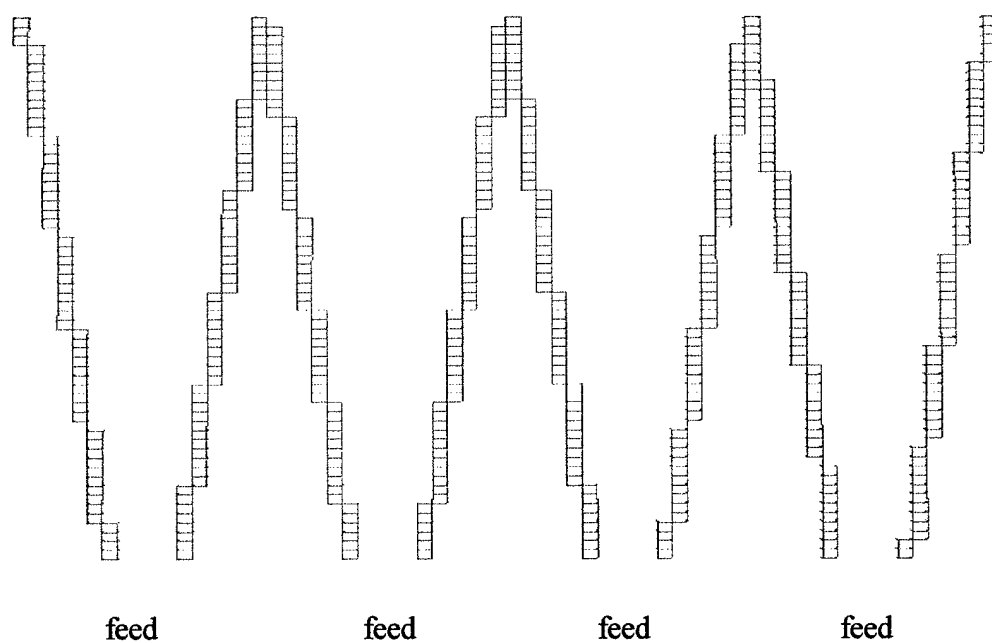


Figure 34. Meshed Model, Side View, Large
4-Element Array (Version 2), Linear Taper

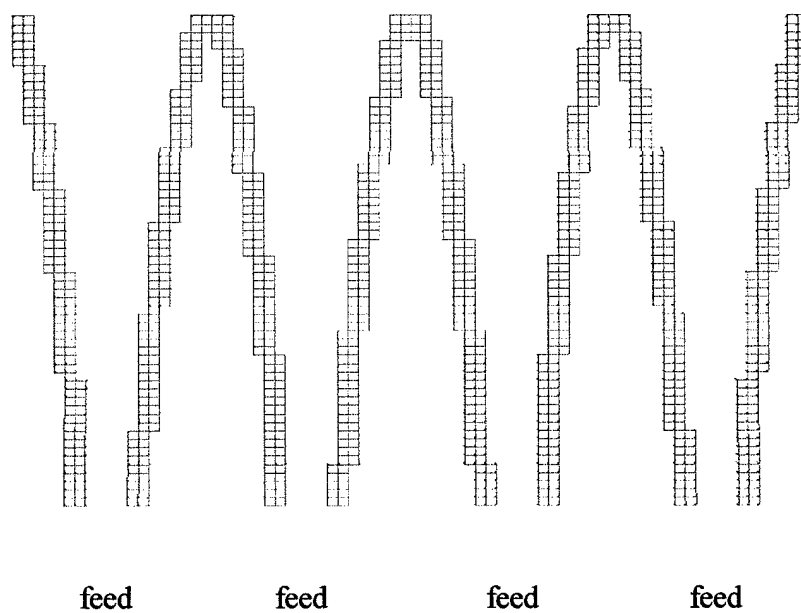


Figure 35. Meshed Model, Side View, Large
4-Element Array, Exponential Taper

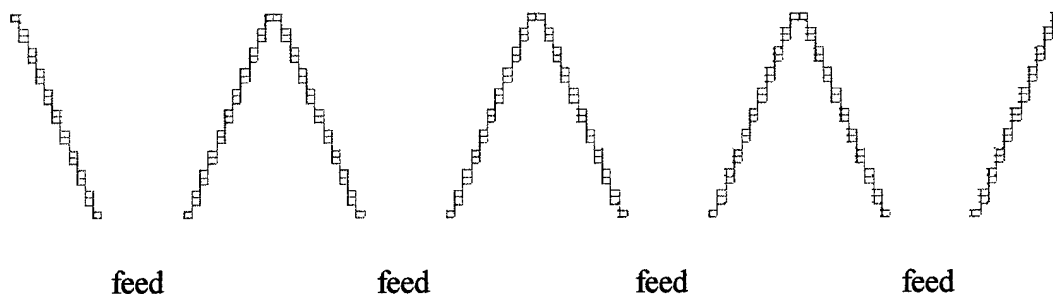


Figure 36. Meshed Model, Side View, Small
4-Element Array, Linear Taper

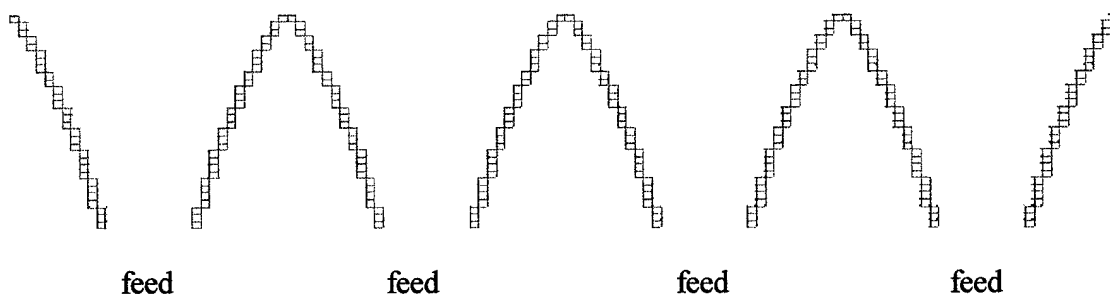


Figure 37. Meshed Model, Side View, Small
4-Element Array, Exponential Taper

Excitation of the Antenna

A x-directed electric field, perpendicular to the plane of propagation, is established in the feed-end of the horn. This is accomplished by specifying the locations of individual point radiators. It is important to note at this point that the radiators become a *hard* source as the field strength goes to zero. This creates a PEC-like boundary condition, which will reflect any field incident to it. This effect will be seen in the late time response. An excellent description of this phenomenon is given in [4].

The pulse shape can be chosen from a set of pre-established pulses generated by TSAR or by user-defined pulse shapes. Both options are exercised in this report.

Experimental Pulse and Modifications

The first pulse shape used in the simulations is an actual experimental pulse generated during laboratory testing of the double-linear horn and its arrays. Several modifications needed to be accomplished before the experimental pulse, shown in Figure 38, could be applied to the models. The original pulse was sampled with a Δt of $1.95503\text{e-}11$ seconds, and contained 511 sample points. Through the Courant criteria, TSAR requires a Δt of $8.33910121\text{e-}12$ for a 5mm cell size. Using an interpolation function in MatLab the pulse was re-sampled with a Δt of $8.33910121\text{e-}12$ secs. The second modification was to trail the data back down to zero gradually. As seen in Figure 38, the pulse doesn't return to zero and abruptly ends at 10 nanoseconds. When the pulse is feed into TSAR as it is, TSAR returns it to exactly zero the very next time step. This would be equivalent to a step function and provide erroneous time and frequency data. To remedy this situation the end of the pulse was backed up and brought down to zero in a gradual manner. The original and final tails are shown in Figure 39.

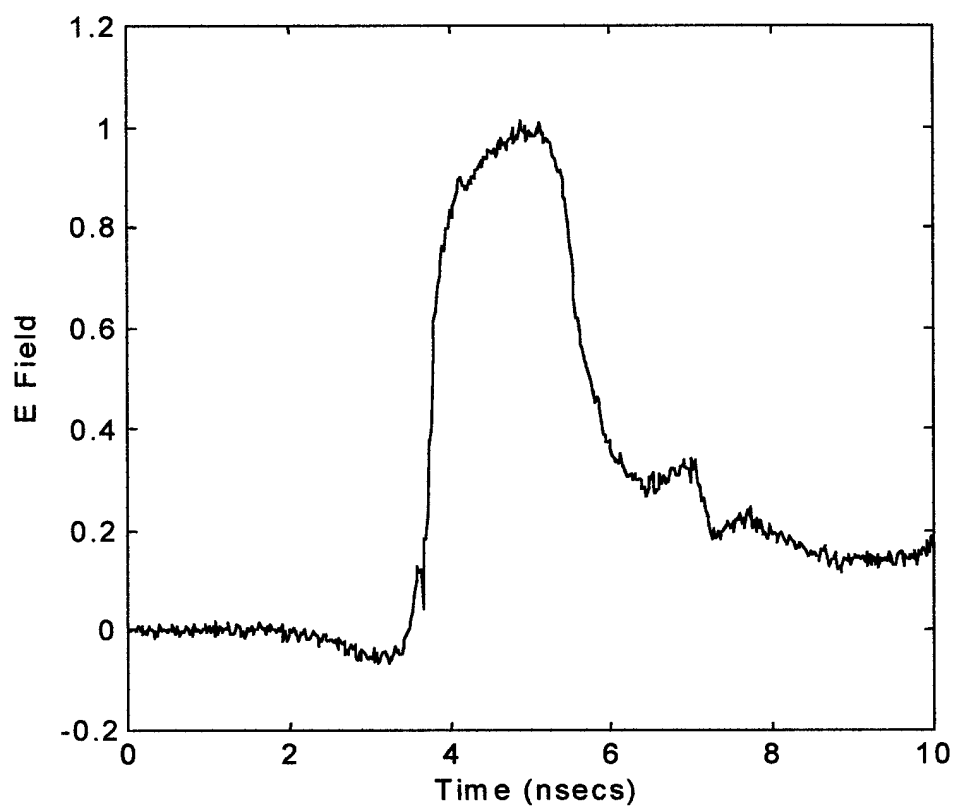


Figure 38. Experimental Pulse Before Modifications

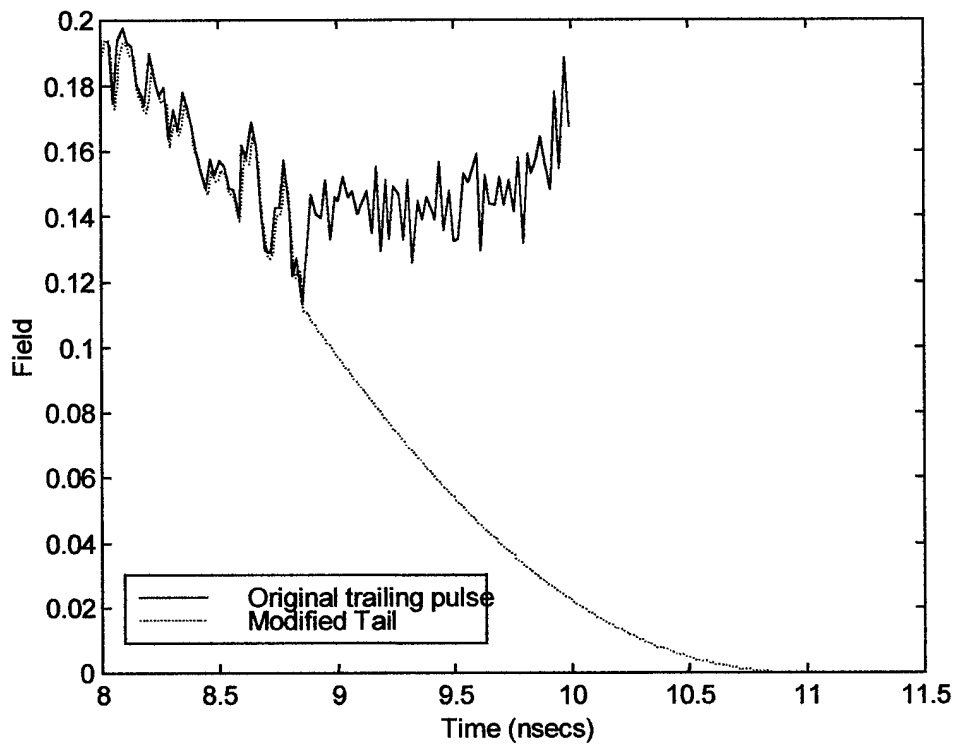


Figure 39. Modification of Trailing End of Experimental Pulse

The modified pulse is shown in Figure 40. This pulse has an approximate 10-90% rise time of 300 pico-seconds and a width of 2 nano-seconds. This pulse is read into TSAR through an external file, whereas the next pulses described are generated internal to TSAR.

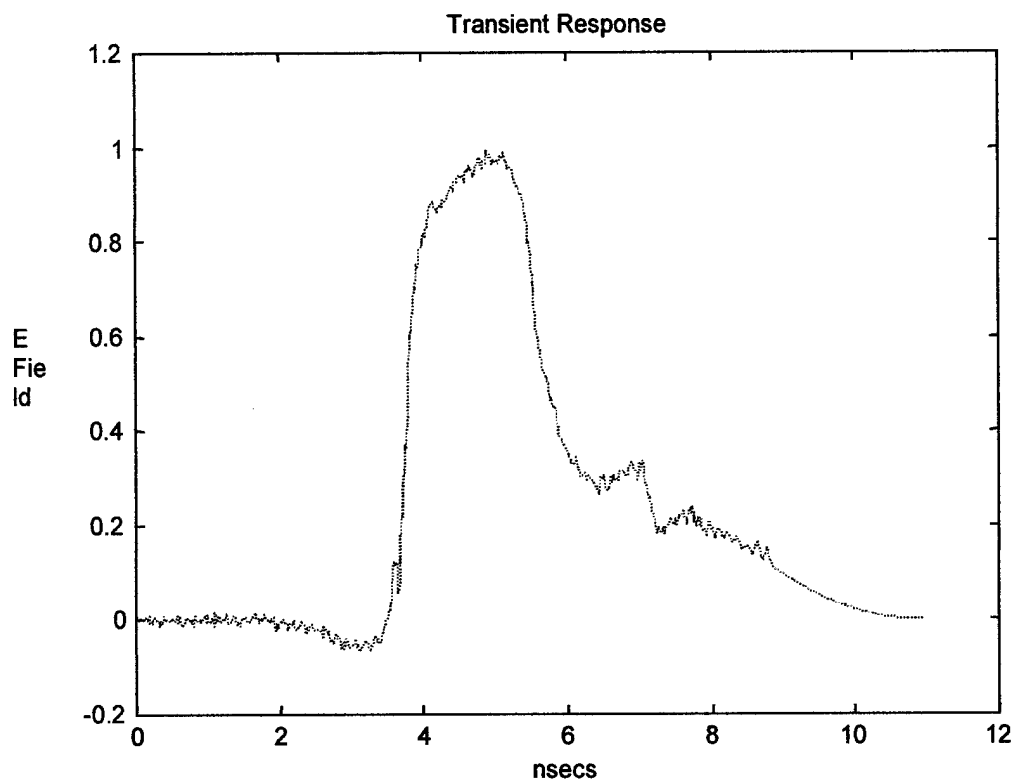


Figure 40. Final Input Pulse Form

Gaussian Pulse

The remaining two pulses are gaussian. TSAR allows the specification of the rise-time and the full width at halfmax. For the pulse used in the larger horn a rise-time (10 – 90%) of 80 pico-seconds and a width of 100 pico-seconds were specified. This pulse is shown in Figure 41a. The pulse applied to the smaller horn having a rise-time of 25 pico-seconds and a halfmax width of 35 pico-seconds, is shown in Figure 42b.

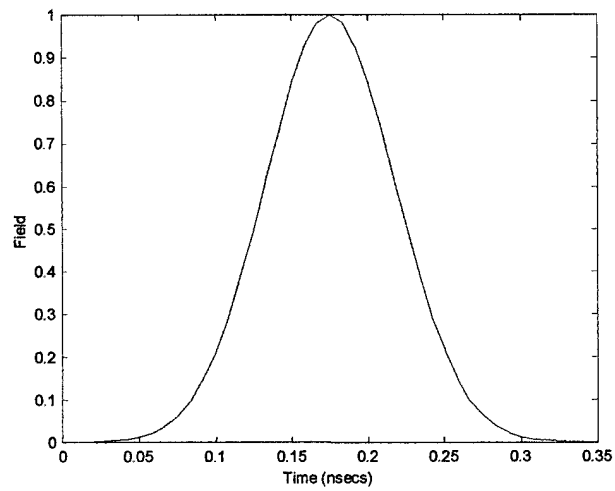


Figure 41a. Guassian Pulse Applied to Large Horn
 (80 picosec risetime, 100 picosec width)

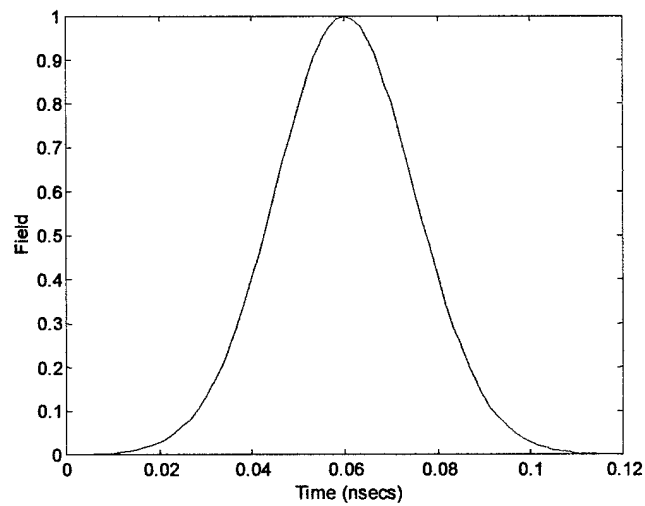


Figure 41b. Guassian Pulse Applied to Small Horn
 (25 picosec risetime, 35 picosec width)

Determination of Simulation Time

Three considerations were taken into account when the simulation times were determined:

- 1) The period required for the entire pulse to propagate to the measurement point.
- 2) The round-trip transit time (period for the electromagnetic wave to travel the length of the horn and back), 2τ . For the small horn 2τ is .2 nanosecs or $120\Delta t$ ($\Delta t = 1.667820242e-12$), and for the large horn, 2 nanosecs or $240\Delta t$ ($\Delta t = 8.33910121e-12$).
- 3) Time to run a simulation.

To accommodate all three considerations, the total simulation time for the large horn was chosen to be 25 nanosecs ($3000\Delta t$), and 3.33 nanosecs ($2000\Delta t$) for the small horn. These simulated times resulted in run times between 5-48 hours on the Sun UltraSparc workstations. There were also some variations to the number of time steps used, depending on the data of interest.

The Collection of the Data of Interest

TSAR allows data (electric, magnetic, and conduction current density) to be collected in two ways. The first is through the use of point sensors. Point sensors can be specified at any grid location within the computational volume. The user also specifies the sensor's orientation and desired field.

The second method allows fields to be determined outside of the computational volume through the use of a near-to-far field transform. The following is the documentation accompanying the transform routine within TSAR's source code. It gives a brief description of theory and the method utilized by TSAR.

The equivalence principal is invoked over a rectangular surface bounding the scattering area. On this surface, electric and magnetic fields are equivalenced to magnetic and electric currents, respectively. These currents are then treated as dipole radiators whose far-field patterns are known. The total far-field pattern is then the sum of all the dipole patterns. Since the far-field pattern of a dipole is proportional to the time derivative of its currents, the derivative must be taken...The equivalence principal requires a single surface on which E and H are known. Since, in the Yee grid, the E and H fields are staggered in space, it is necessary to interpolate the H fields to be in the E field plane.

Using the spherical coordinate system and the transform described above, the far-field quantity can be determined for any θ and ϕ , at any R.

Again, this research effort makes use of both methods for determining E-field quantities. Using the transform method, the far-field transient response is determined at $\theta=90^\circ$, and $\phi=0^\circ, 15^\circ, 30^\circ, 45^\circ, 60^\circ, 75^\circ, 90^\circ, 105^\circ, 120^\circ, 135^\circ, 150^\circ, 165^\circ$, and 180° . The $(\theta=90^\circ, \phi=0^\circ)$ location is boresight of the antenna. The fields are also calculated at $\phi=0^\circ$, and $\theta=0^\circ, 30^\circ$, and 60° . The distance, R, is set at 1.25 meters. The distance is really insignificant in the research effort. Only the relative amplitudes are of concern, and R just turns out to be the scaling factor ($1/R$). Figure 42 shows the coordinate convention used throughout this investigation.

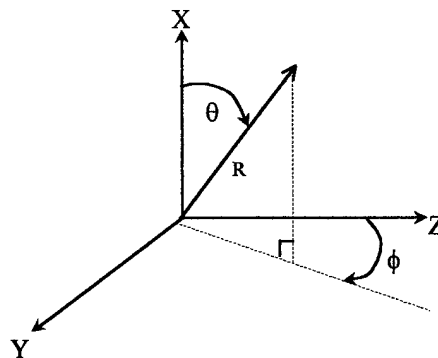


Figure 42. Coordinate Convention

The point sensors are distributed along the boresight axis of the antenna. Some are set in the far-field, some in the near, and some inside the horns themselves. The point sensors report the actual field strength at that point.

Analysis Technique

Time-Domain

Each run produces approximately 100 time history pictures. Half of these reports are collected with the point sensors and half with the transform method. Some show obvious differences in field strengths and patterns, other are less insightful. A select few are chosen for analyzes purposes. Each pattern is analyzed for obvious deviations from the established baseline antenna, double-linear (version 1). Because the goal is to determine if the exponential curves produce desirable affects in the UWB characteristics, the transient responses is taken to the frequency domain and the power spectral density analyzed.

Frequency-Domain

The frequency analyses is limited by the accuracy of the FDTD method as determined by the cell size. Working backwards from the established criteria of $10\Delta/\lambda_o$, where λ_o is the highest frequency with a significant contributions, the frequency bandwidth is assumed reliable up to 6 GHz for the 5mm grid and up to 30 GHz for the 1mm grid.

Reduction of Run-Time Study

The reduction of run-time part of the study involves two aspects that decrease the computational volume. The first is cell size, therefore the second version of the big horn is re-meshed at a cell size of 10mm. Now there are two new versions of the second version of the big horn, a 5mm-meshed version and a 10mm-meshed version.

The second aspect involves applying image theory to the symmetrical horns. Applying a PEC surface to the horizontal center plane creates the first set of configurations. Applying a PMC surface along the vertical center plane in addition to the PEC mirror boundary creates the second set of configurations. The result is an electrically equivalent quarter horn or arrays of horns, and a reduction in the

computational volume of 75%. Figure 43 illustrates the application of the mirror boundary conditions to a four-element array.

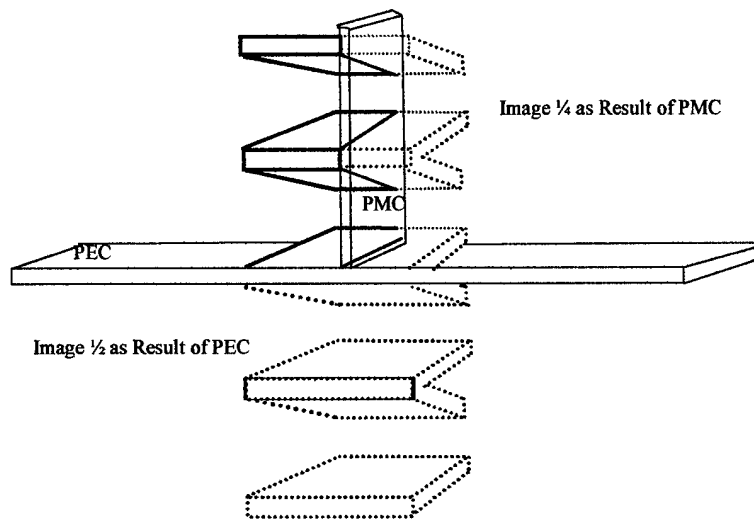


Figure 43. Application of Mirror Boundary Conditions

Each run-time is computed from the initial start time (recorded manually) and the ending time as record by the last file write. The analysis techniques discussed earlier are applied to the results in order to determine the accuracy of the reduced models.

Chapter Review

This chapter details the design and development of the models, the input pulses and other input parameters required by TSAR. A quick look at theory behind the near-to-far transform used in this code is presented. The method of analyze is describe, as is the technique for reducing the computational volume.

Chapter 4: Results and Analysis

The first section of this chapter establishes the double-linear design as the baseline. This is accomplished in two steps. In establishing the baseline, some of the possible reasons for the variation between the experimental data and the FDTD simulations are presented. The next sections attempt without much success to identify any reduction in late time reflections between the baseline model, and the exponential taper designs. The advantages of the transient arrays are explored and the last section is devoted to the reduction of run-time study.

Establishing the Base Line

The first step is to validate that the models' and the FDTD code's ability to represent what has been determined experimentally. This is the reason for the second version of the double-linear array models, of which every attempt is made to accurately model the physical antennas. Because the aperture dimensions of the single-element horn remain unchanged between version one and version two, only version one is considered.

FDTD simulations were performed on the large single-element double-linear taper horn as well as each of the two versions of the 2 and 4- element arrays. The experimental pulse (altered as described in Chapter 3) was fed into the simulations. Each simulation was run for $3000\Delta t$ ($\Delta t=8.3391$ psecs), or the equivalent of 25 nsecs. The FDTD data, used for the validation, was collected with the transform method. A bounding surface enclosing the horn was established 1 cell out (in all three directions) from the horns' outer-dimensions. The time-domain comparisons of the experimental runs verses the computational results from the large double-linear horn are shown Figure 44-46. Their respective power spectral density plots accompany them.

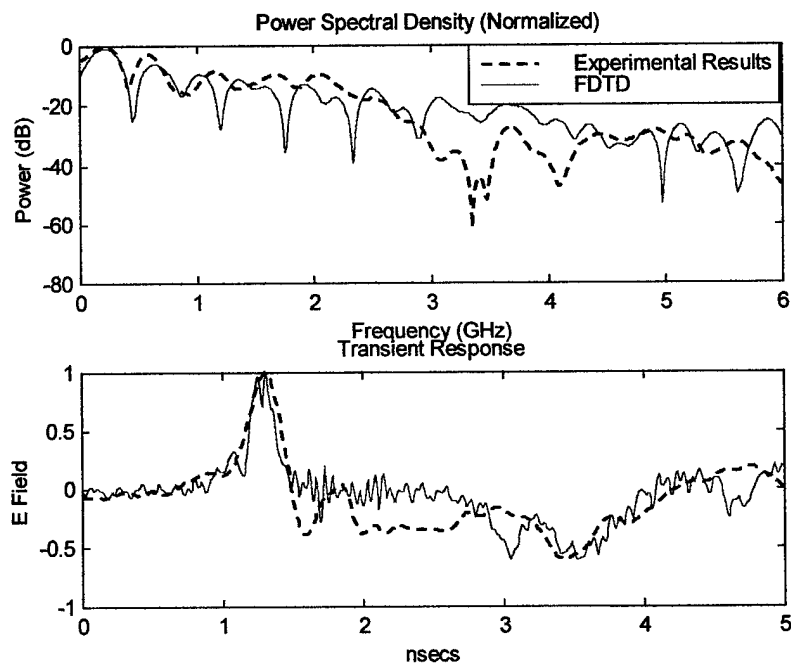


Figure 44. Single-Element Double-Linear Horn, Experimental Results vs. Simulated – PSD and Transient Response

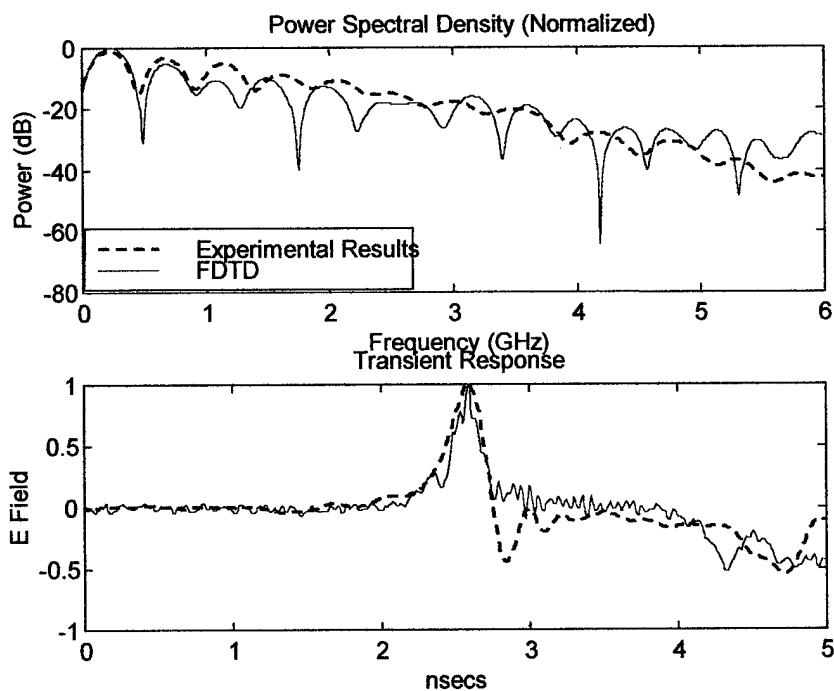


Figure 45. 2-Element Array Double-Linear Horn (version 2) Experimental Results vs. Simulated – PSD and Transient Response

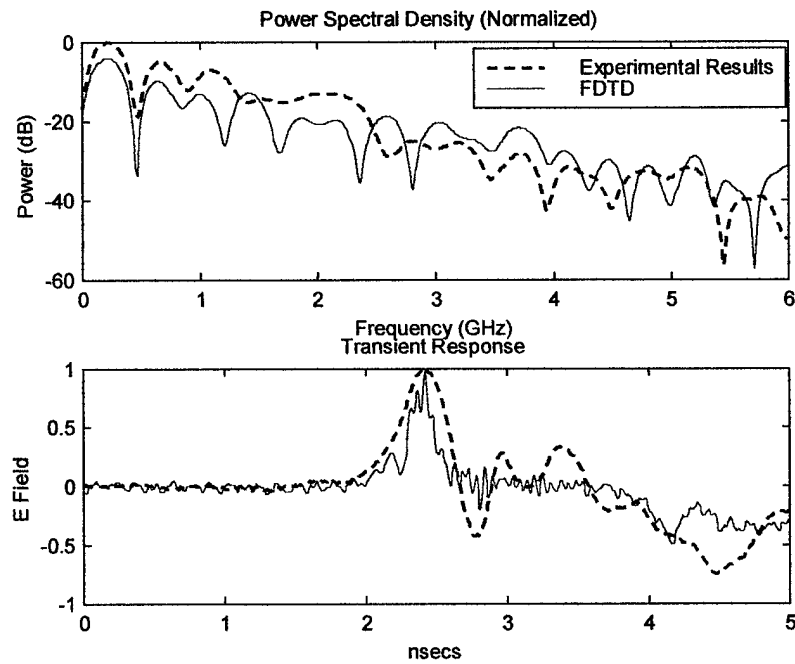


Figure 46. 4-Element Array Double-Linear Horn (version 2) Experimental Results vs. Simulated – PSD and Transient Response

Because the first version of the double-linear model is considered the baseline for the remainder of the study, a similar comparison is accomplished between version one and the experimental data. The results are shown in Figure 47 and 48.

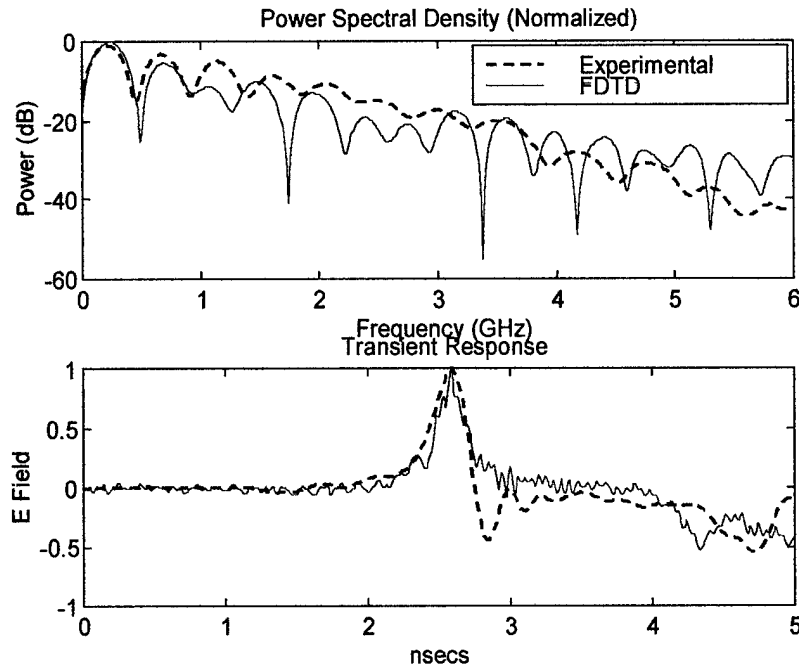


Figure 47. Two-Element Double (version 1)-Linear Horn, Experimental Results vs. Simulated – PSD and Transient Response

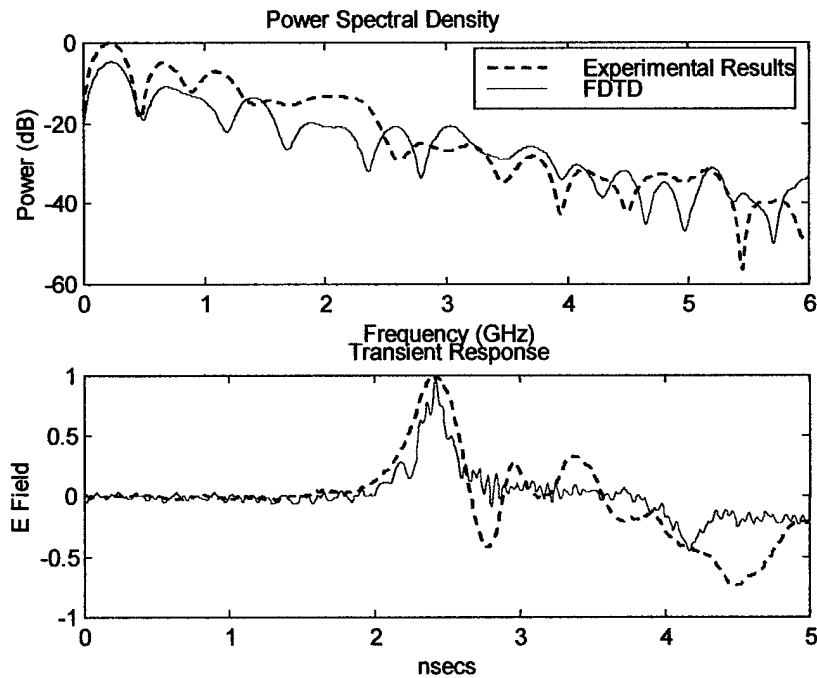


Figure 48. Four-Element Double-Linear Horn(version 1), Experimental Results vs. Simulated – PSD and Transient Response

Version 1 appears to follow the experimental results relatively well, and from this point on all three antennas (double-linear horn, and 2- and 4-element arrays of the double-linear horn) are considered reasonably accurate models. The differences seen between experimental and numerical results can be attributed to several variables.

Differences Between Model and Experiment

The first, of course, are the obvious limitations of the FDTD's numerical approximations and the ability to resolve details of the antennas using a cubic mesh. Not so visible is the fact that the input pulse used to excite the FDTD models is not the same pulse used to excite the experimental horns. The experimental pulse was measured while a *dummy* load was applied to the source. Although repeatability for this type of source is good, some differences may exist between successive shots. There is also the alteration made to the tail (explained in Chapter 3) of the experimental pulse fed into TSAR. The finite conductivity of the experimental horn verses the PEC plates used in the model is another variation, as is the method of feeding the conducting plates. In the experiment the horns are feed with a parallel plate transmission line, and in the simulations the field is created just inside the mouth of the feed. The final discrepancy is the rate at which the experimental results were sampled at. The FDTD results are sampled at Δt (8.33910121e-12 secs), the experimental output is sampled at a Δt of 4.88759e-12 secs.

Pulse and Bandwidth Limits

The transform of the experimental input pulse to the frequency domain reveals a maximum power content in the lower frequencies as demonstrated in Figure 49. This maximum is also exhibited in the output response of the double-linear single-element horn and is also shown in the figure. The negative spikes appearing in the output spectrum are also attributed to the input pulse. In order to fully realize the bandwidth of the horn, a gaussian pulse (wide bandwidth) is applied to the horn. The results are displayed in Figure 49.

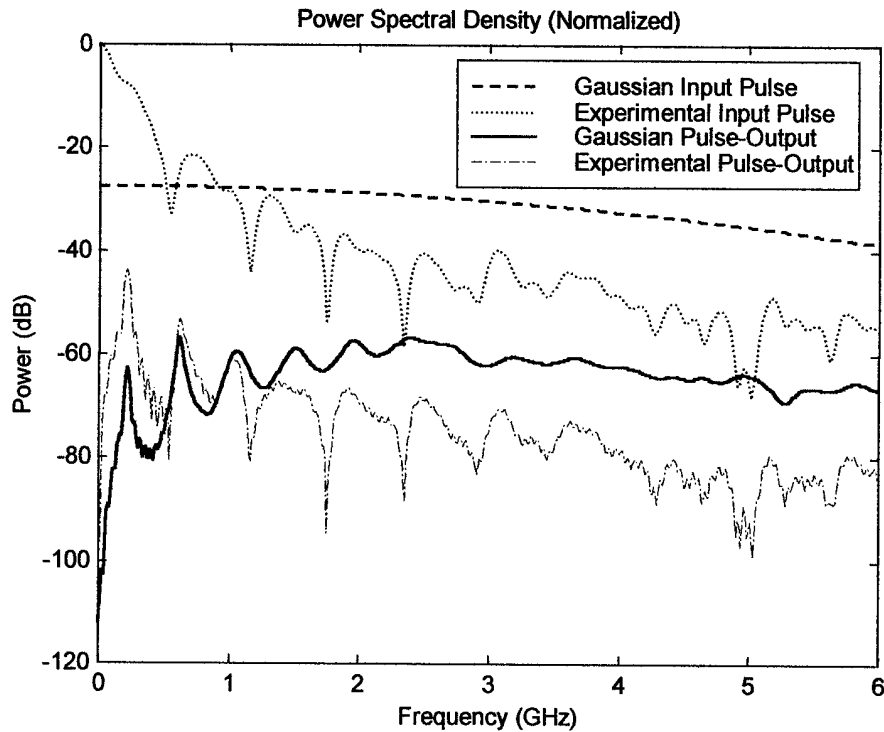


Figure 49. PSD of Experimental and Gaussian Input pulse and the Corresponding Outputs from the Single-Element Double-Linear Horn

The output of the horn excited with the gaussian pulse shows a low-frequency roll off as expected, but with two predominate upward spikes at approximately 300 and 600 MHz. These fluctuations are also manifested in the output produced with the experimental pulse, the increase over the gaussian output due to the high low-frequency content of the experimental input pulse.

An investigation reveals that the low-frequencies spikes are the results of standing waves created within the horn, as well as other reflections. Figure 50 shows the creation of the standing wave inside the double-linear horn. Notice the propagation of the pulse and the fixed nulls of the standing wave.

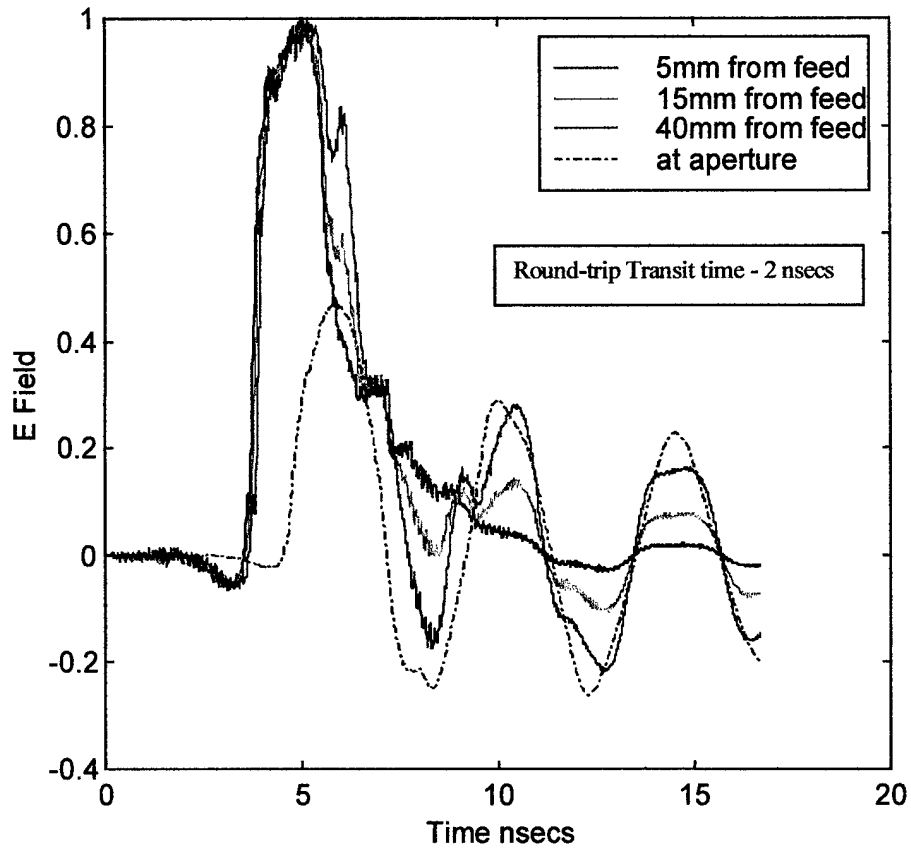


Figure 50. Creation of the Standing Wave

A frequency analysis of the far-field confirms the that the late-time field values dominate the low-frequency spectrum. To perform this analysis, the total pulse is divided into three sections, and each section independently transformed to the frequency domain. The far-field transient response to the gaussian input pulse is shown in Figure 51. The first part is the initial pulse (time steps 1-360). Because the width of this pulse is narrow ($60 \Delta t$ at the base), it is assumed free of reflections. The field strength of the middle section (time steps 360-900) is assumed to be predominately from the reflections of the field due to the abrupt transition from horn impedance to the impedance of free space. The length is of this section is chosen to be 4τ or 2 roundtrip-transit times (τ is approximately $120\Delta t$ or 1 nsec for the large horn). The late-time section is the remainder of the pulse and assumed to be dominated by the ringing effect of the standing wave.

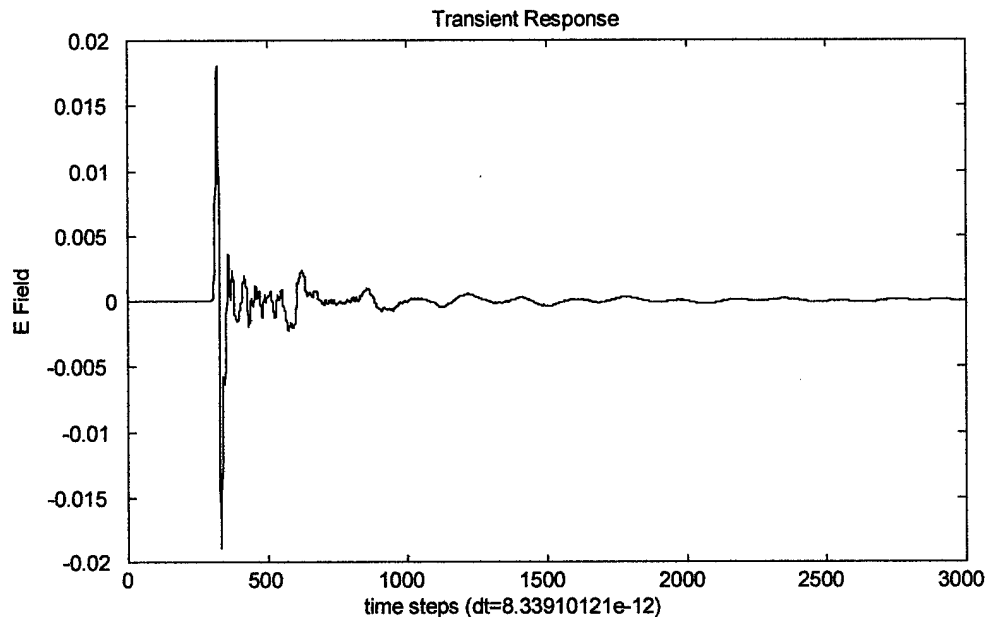


Figure 51. Transient Response Resulting from Gaussian Pulse
Excitation of the Double-Linear Single-Element Horn

Figure 52 shows the frequency results of segmenting the transient response. The early time frequency response is flat and has a low-frequency roll off as predicted. The frequency response of the total wave-form transform closely follows the early time response, but predominate features from the mid-time section appear in the total frequency response. An example is the 1.9 GHz to 3.2 GHz. The two magnitudes appear to add constructively. This makes sense seeing this section contains the first and second reflections from the aperture, as seen in the time-domain. These frequencies also show up in the late time response but are greatly reduce in magnitude. The mid-time region also shows the increase in the low-frequencies, but this feature is dominated by the late time response. The spikes in the low-frequency regions of the total response are clearly the results of the late time response. The periodic ringing in the horn, caused by reflecting surface currents, is responsible for this portion of the frequency response. An easy to understand explanation of this phenomenon is given in [1].

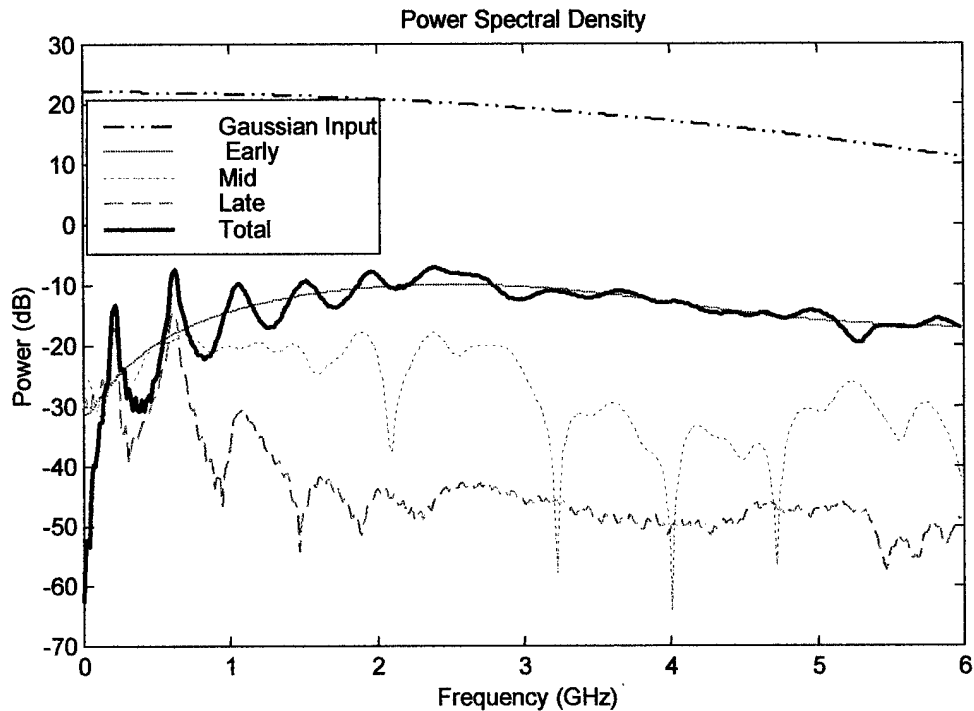


Figure 52. Frequency Response Resulting from Segmentation of Total Transient Response

A similar segmentation analysis was conducted on the transient response of the single-element double-linear horn excited with the experimental pulse. Although not as clear as the results produced with the gaussian pulse, the same conclusions are met. The graphical results are found in Appendix A.

Now that the baseline is established, the study turns towards the exponential curved designs.

Exponential Curves - Peak Field Values Dominate

Time-Domain

When observing the transient response, the most visible feature is the amplitude of the early time pulse. In the far-field zone of the antenna, the radiated pulse is the first

time-derivative of the excitation pulse. The peak E-field values shown in Table 2 are the result of each simulation. Also shown in the table is a relative comparison, in decibels, of the double-linear field strengths and the exponentially curved designs. These values were calculated as follows:

$$Increase(dBs) = 20 \log \left(\frac{Field_{ExponentialCurve}}{Field_{Double-Linear}} \right). \quad (26)$$

Table 2. Peak Field Strengths and Design vs. Baseline Comparisons

	Dbl- Linear Field V/m	X-dir Exp Field V/m	Increase (dB)	Y-dir Exp Field V/m	Increase (dB)	Dbl-Exp Field V/m	Increase (dB)
Large Horn, Experimental Pulse							
Elements							
1	7.4149e-3	7.7730e-3	4.0967e-1	7.3166e-3	-1.1586e-1	7.4822e-3	7.8538e-2
2	2.0939e-2	2.2034e-2	4.4277e-1	2.0339e-2	-2.5252e-1	2.1588e-2	2.6511e-1
4	3.9895e-2	4.1454e-2	3.3282e-1	3.8723e-2	-2.5894e-1	4.0457e-2	1.2155e-1
Large Horn, Gaussian							
1	1.8074e-2	1.7345e-2	-3.5763e-1	1.8674e-2	2.8381e-1	1.7933e-2	-6.8027e-2
2	3.8649e-2	3.9672e-2	2.2690e-1	3.9946e-2	2.8671e-1	4.1060e-2	5.2576e-1
4	7.5705e-2	7.6644e-2	1.0709e-1	7.8106e-2	2.7121e-1	7.9381e-2	4.1189e-1
Small Horn							
1	5.4367e-2	5.7404e-2	4.7225e-1	5.4064e-2	-4.8410e-2	5.7937e-2	5.5253e-1
2	1.1770e-1	1.2543e-1	5.5238e-1	1.1743e-1	-2.0076e-2	1.2656e-1	6.3038e-1
4	2.3087e-1	2.4514e-1	5.2118e-1	2.3007e-1	-3.0097e-2	2.4779e-1	6.1451e-1

Identifying and Quantifying Reflections

The fact that the peak values are different in each case makes the identification of reflection-alterations (either increase or decrease) difficult. This proves itself in the examination of the transient responses. In each case, when and if, the reflections are

identified, the ratio between base-line and exponential-taper design also exists between initial and reflected pulses. This is shown in Figure 53 and 54. Figure 53 displays the transient responses collected with a point sensor approximately one quarter down the length of the large-horn (from feed and on boresight). In this example, the horn was excited with the experimental pulse.

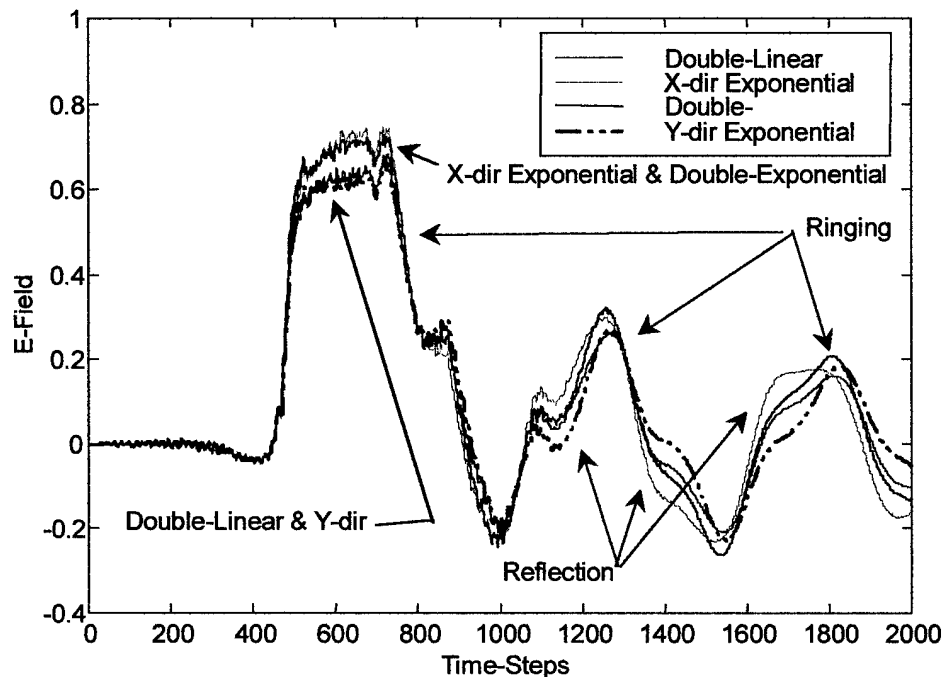


Figure 53. Looking Inside the Large Horn – $\frac{1}{4}$ the Length from the Feed and On Boresite – Experimental Input Pulse

The same phenomenon is manifested in the ringing characteristic. The added issue of the FDTD *hard-source* acting like a PEC surface as the pulse returns to zero, coupled with the apparent phase shifting between designs and between the two sources of late-time responses, contributes negatively to this analysis technique. The issue of the reflected waves and initial waves having the same ratio leads to the conclusion that reflections are not reduced from design to design. Again, this is concluded with no enthusiasm in the confidence level. Figure 54 is a second example, but this time it is the

small horn excited with gaussian pulse. The discussion above applies to this figure as well.

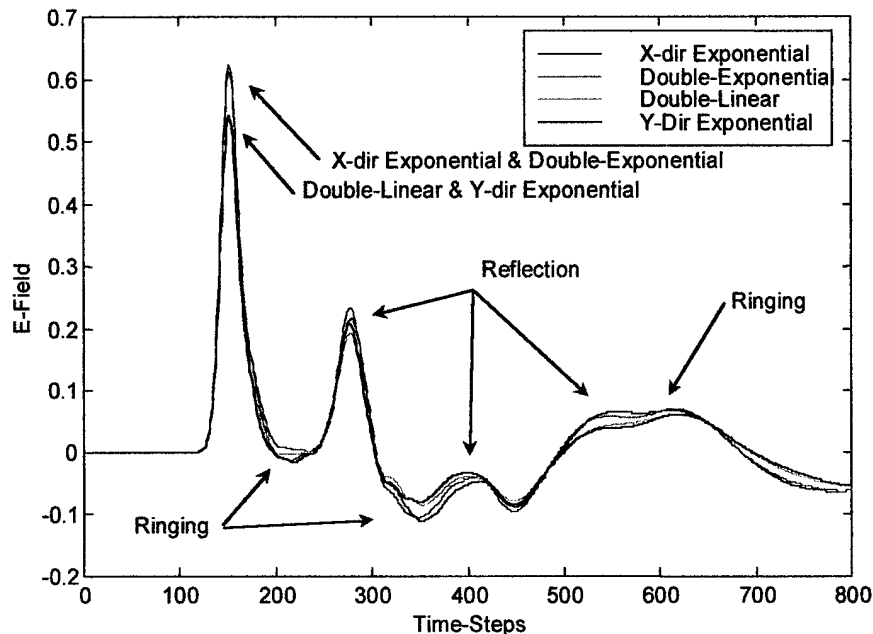


Figure 54. Looking Inside the Small Horn – $\frac{1}{2}$ the Length from the Feed and On Boresite – Gaussian Input Pulse

Frequency-Domain Analysis

The time-domain data is transformed to the frequency-domain to see if this technique provides any insight. The segmentation process described earlier is accomplished on each response. The same conclusions are formed. The initial pulse's strength is repeated in the reflections. The 2-element array excited with gaussian pulse was randomly selected from the test matrix as an example. Figures 55-58 demonstrate the difficulty in quantifying the effects of the exponential curves. Figure 55 shows the positive swing of the initial pulse and Figure 56 shows the negative. Figure 57 is the PSD of this portion of the pulse, and Figure 58 is the PSD of the entire transient response. Once again the peak values in the transient response dominate and no useful information on the reflections is gleaned. This process produces similar results in each design comparison.

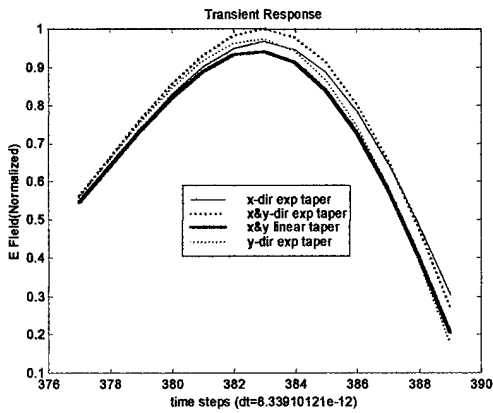


Figure 55. Positive Portion of Initial Gaussian Pulse
Large 2-Element Array

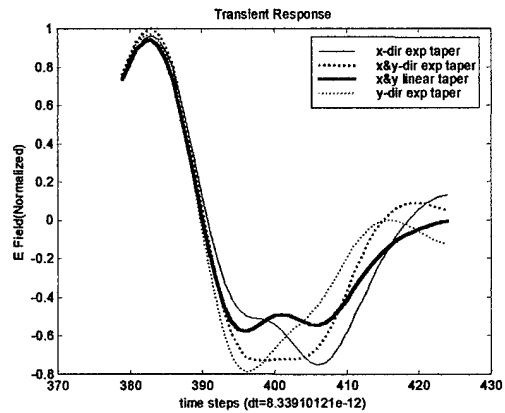


Figure 56. Negative Portion of Initial Gaussian Pulse
Large 2-Element Array

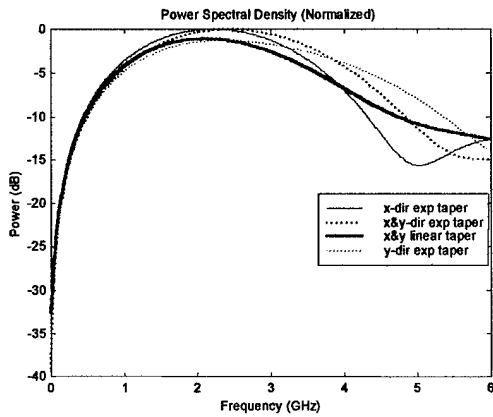


Figure 57. PSD of Entire Initial (Early) Gaussian Pulse
Large 2-Element Array

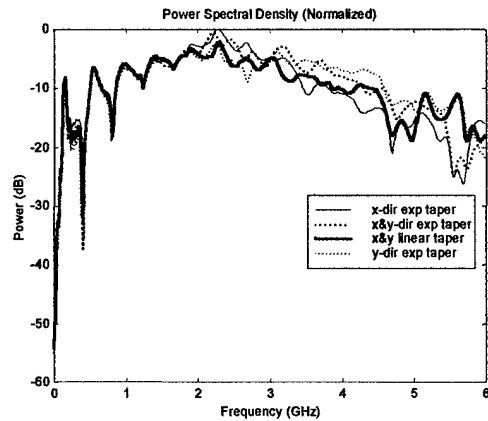


Figure 58. PSD of Entire Transient Response
Gaussian Pulse, Large 2-Element Array

Arrays

Up to this point, except for the increased peak field value, the results indicate a need for further research. The study now turns toward the arrays to see if the advantages discussed in the literature can be realized with the FDTD method.

Figure 59 is a comparison of the transient responses of the 1-element, 2-element, and 4-element double-linear array. The 2-element has been scaled down by a factor of 2 and the 4-element has been scaled down by a factor of 4.

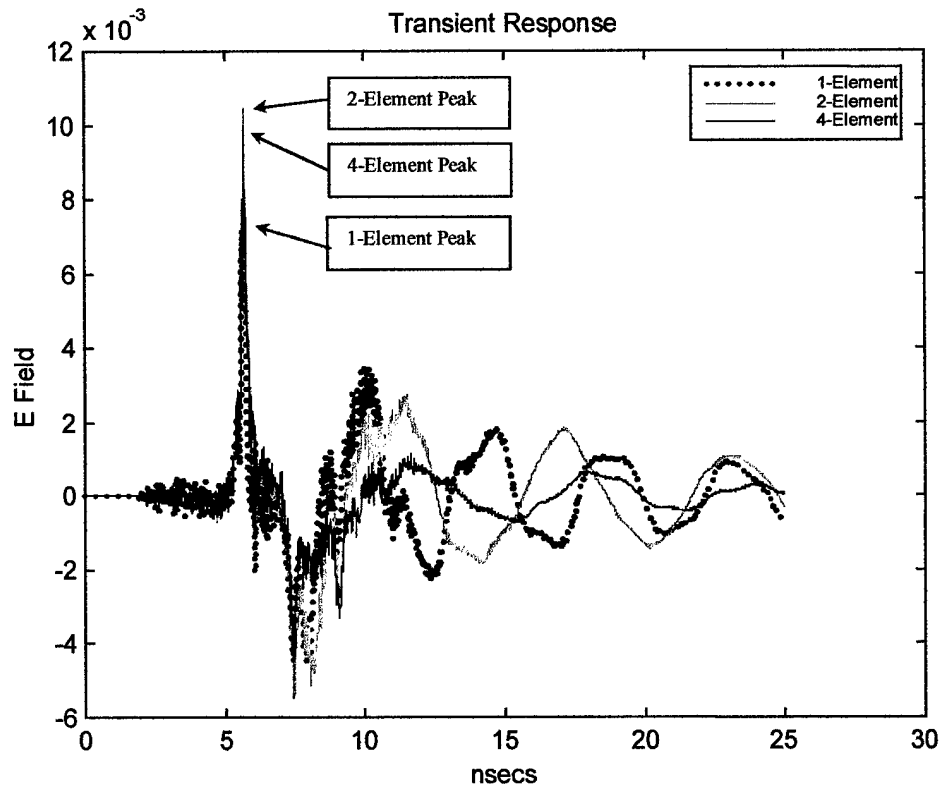


Figure 59. Comparison of Transient Response of 1-Element, 2-Element, and 4-Element Double-Linear Configurations

Figure 59 reveals the reduction of the ringing between the one, two, and four-element configuration. Another point to note is that even with the scaling the peak field strengths are increased in the arrays. Both attributes demonstrate the mutual coupling effects of the array. The frequency-domain confirmed the time-domain investigation and the PSD plot is shown in Appendix A. Similar investigations were conducted for each design, each producing similar results. The results of the large double linear horns, excited with the gaussian pulse, and the small double-linear configurations are displayed in Appendix A.

Figure 60 is a look inside each element of the large 4-element double-linear array. The data collected at the same location in the single-element horn is also shown in the figure. The plots of the inner elements show the effects of having adjacent elements on both sides, whereas the outer elements, with only one-side adjacent to another element, appears to have a combination of the effects. The outer-elements contain the same spike as the single-element simulation, and the pulse begins to widen as it sees the effect of the adjacent element (delayed by the propagation time).

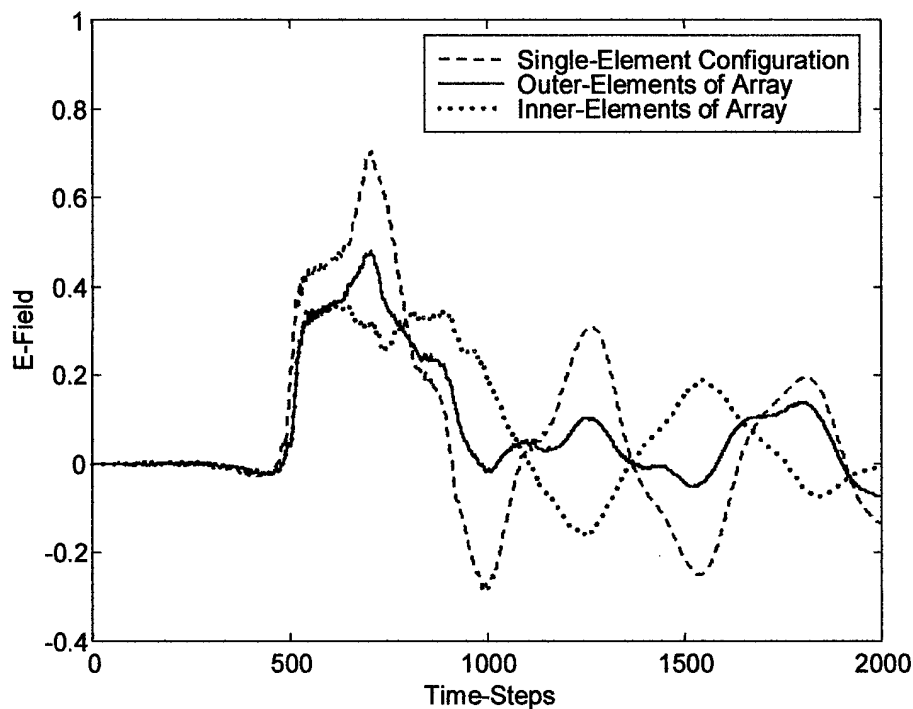


Figure 60. A Comparison of Each Element of the 4-Element Array and the Single-Element Horn of the Same Design

The multiply elements have demonstrated their worth in UWB radiation, some different element designs have been tried with limited success, now the attention turns to

optimizing the designs for optimum success. The results of the next section are only the first steps in the process.

Reduction In Run-Time Study

The single-element double-linear is the test subject for this section. It is meshed at two resolutions; 5mm and 10mm. PEC and PMC boundaries are applied in the appropriate manner to simulate the full horn. Data is collected with the near to far-transform. The computational volume is set just large enough to include the surface-enclosing boundary and the absorbing boundaries.

Full vs. Quarter – 5mm Grid

Figure 61 gives the results of the full and the quarter-horn (with a 5mm grid) comparisons. The quarter-horn's transient response shows a decrease in late time ringing, probably the result of a $\frac{3}{4}$ reduction in conductor plates and consequently surface currents. The variation also shows up below 250Mhz in the PSD plot, as expected.

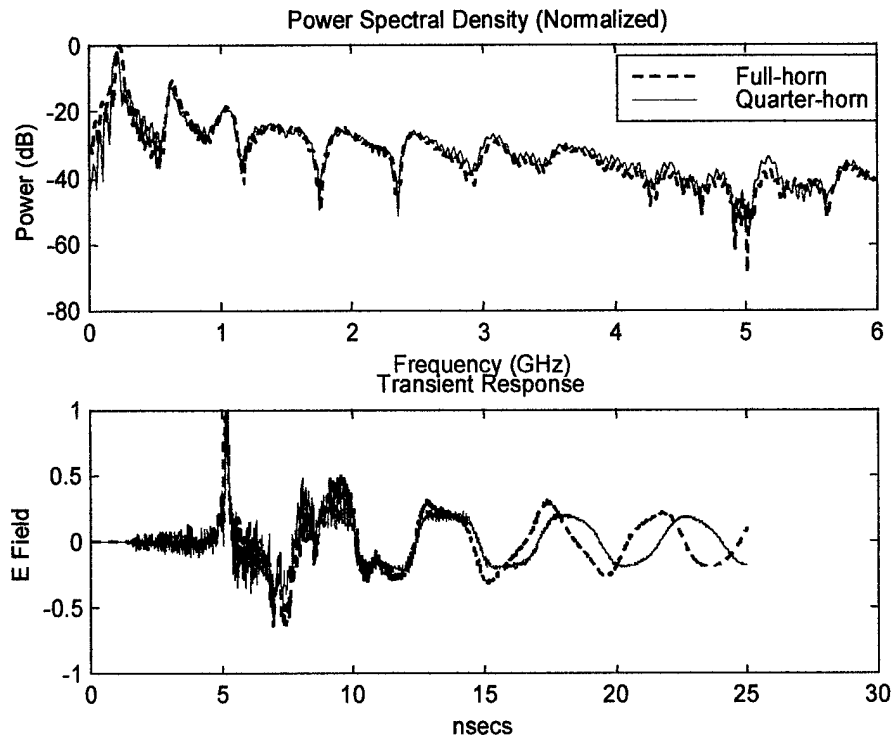


Figure 61. Full and Quarter Horn Comparison
(5mm Cell Size)

Full Horn – 5mm vs. 10mm

The same full horn is re-meshed with a 10mm cell size. The comparison is shown in Figure 62. Once again the early-time pulse, up to about 12 nsecs, follows the 5mm response. Past that point the ringing effect becomes more pronounced. In the frequency domain the 10mm horn drops approximately 10 dB through the pass-band of the horn (1.5 – 4 GHz).

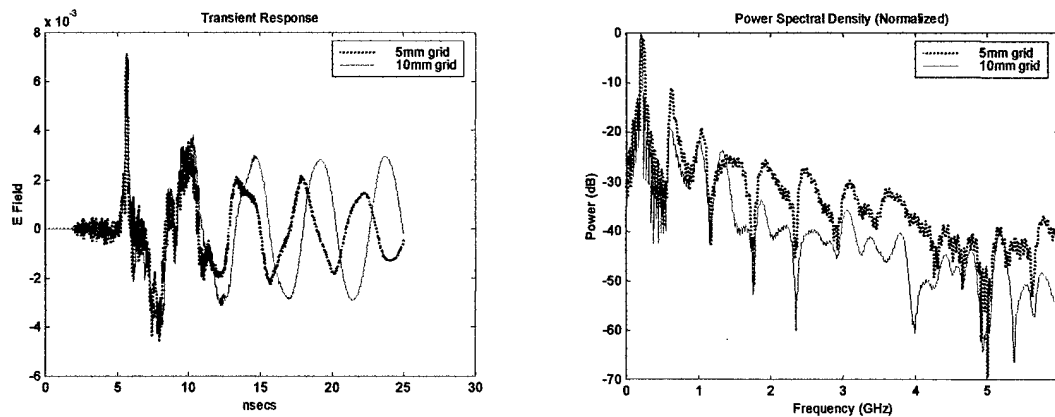


Figure 62. Full - 5mm vs. 10mm Comparison

Full vs. Quarter – 10mm Grid

The final comparison is shown in Figure 63. The results are similar to those found in the 5mm full and quarter-horns analyzes. Notice that the ringing is dampened as with the first comparison. The early-time pulse matches almost exactly up to the first zero crossing. The 5 – 6 GHz range shows the largest discrepancy, 10 – 20 dB. For a 10mm grid the highest frequency of accuracy is 3 GHz, so this range should not be considered anyway.

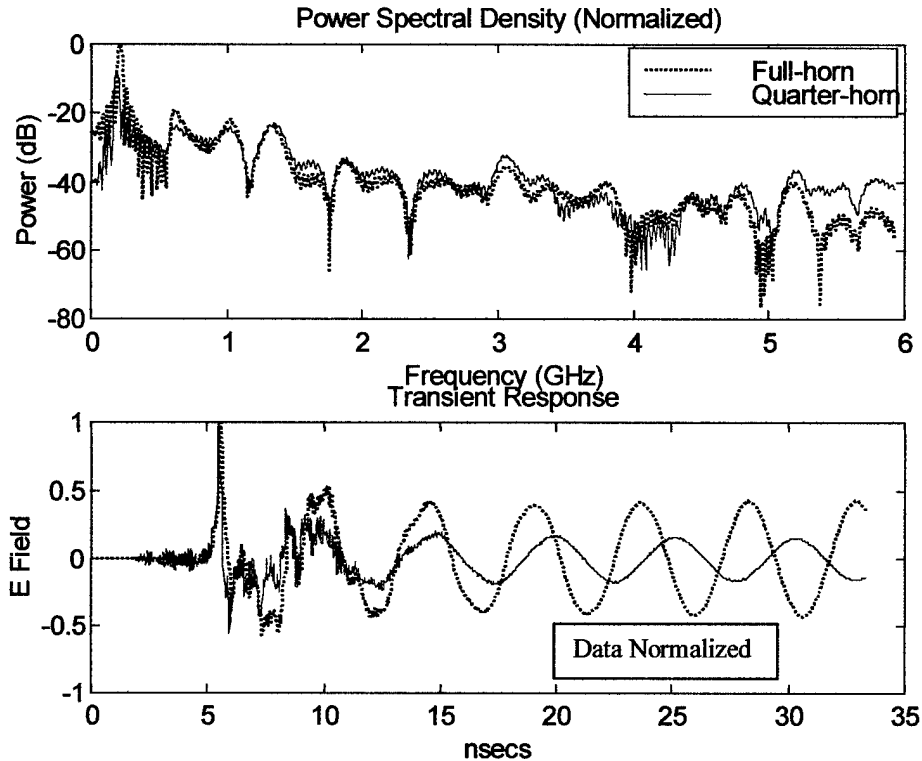


Figure 63. Full and Quarter Horn Comparison
(10mm Cell Size)

Early-Time

In the examples above the 5mm-meshed horns ran for 3000 time-steps (equivalent to 25 nsecs), and the 10mm-meshed horns ran for 2000 time-steps (equivalent to 33.4 nsecs). To simulate equal periods of time, the 10mm-mesh should be run for 1500, time-steps. For the purposes of this study it was intentionally chosen longer in order to put the emphasis on the cell size and not the number of times the fields are calculated for.

Going the other direction, the number of time-steps is reduced in order to gather only the prompt time portion of the transient response. If only the early-time (initial) pulse is of interest, the run-time can be reduced considerable. In the following example the number of time-steps is chosen to be 800. This is approximately the number required for the entire pulse to travel from the feed to 1 meter. It also includes 3 roundtrip transit

times. The results of this run are not displayed, but the result can be seen in the first 13 nsecs of the quarter-horn response shown in Figure 63.

Summary of Time-Reduction Study

The results of this part of the study are displayed in Figure 64. Although this section only displayed the results of the single-element problem, the same process was accomplished for the 4-element double-linear array. The run-time was reduced from 17.5 hours to 4 hours.

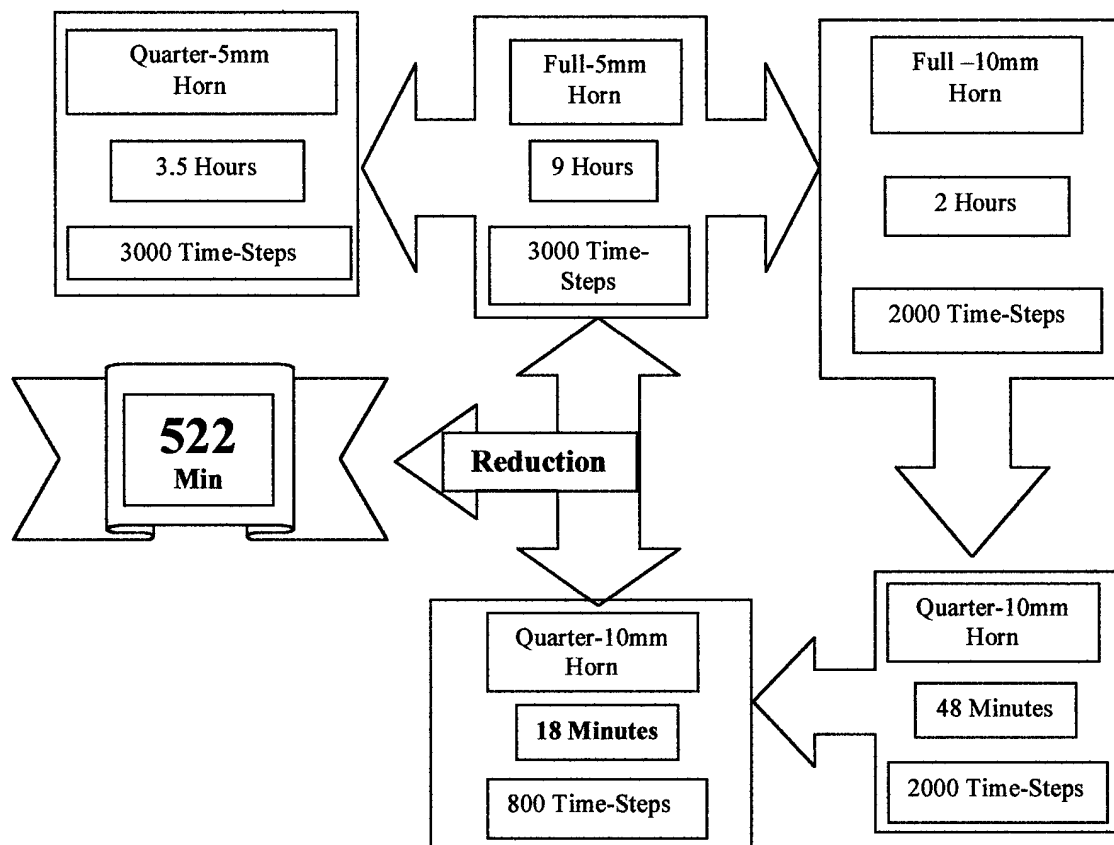


Figure 64. Summary of Reduction of Run-Time Study

Chapter Review

This chapter is the culmination of the work accomplished in this research effort. Because of the extent of the test beds and the mass of data collected, examples have been randomly selected and placed in this report to demonstrate the results. The peak values were increased in all but a few cases, which leads to some weak conclusions. These conclusions are presented in the next chapter. The significant contribution is the FDTD confirmation of the advantages enjoyed by the transient arrays. The final section demonstrated taking advantage of the symmetry of the TEM horns and applying image theory to reduce run-times significantly.

Chapter 5: Conclusions and Suggestions

This chapter provides a summary of the research conducted up to this point and provides a springboard for further research. The opportunities are spawned by observations made during this research endeavor, as well as the continuation of the possibilities presented in the beginning. Some conclusions are drawn based on the numerical data, while others based on logic and intuition. Every effort is made distinguish between them and show the areas requiring further research.

Conclusions

The original objective was to determine how the exponential curves influenced the UWB characteristics of various TEM horns configurations. The original thinking was that the late-time reflections produced by horns with different design variations and fed with different pulses, could be used as a measuring stick for the effects of the exponential curves. When a reflection's amplitude was reduced, as compared to the reflection of the baseline model, the exponential curve provided a smoother transition to free space.

This thinking is not necessarily flawed, but the effects unobservable using the analysis techniques employed. One of the difficulties in analyzing the late time reflections is that the ratio between the baseline's initial pulse and the exponential design's initial pulse also existed in the late-time reflected pulses. The fact that the ratio is maintained leads to a weak conclusion - the exponential tapers do not reduce reflections resulting from the abrupt transition to free space. It also leads to the second conclusion – the exponential curves do influence the UWB radiation characteristics, depending on the pulse employed to excite the horn. The basis for this conclusion is described below.

A constant throughout the investigation is that the peak values of the initial pulses are different from design to design, horn to horn, and pulse to pulse. A comparison of the peak values of the responses from the exponential curves, as compared to the established

baselines, was made in Chapter 4 and shown in Table 2. Based on the relative comparisons in Table 2 the values are ranked in two manners and presented in Table 3. The first ranking is according to the number of elements and the second is according to design.

Table 3. Ranking of Designs According to Peak Field Strengths.

		X-dir Exp		Y-dir Exp		Dbl-Exp	
Elements							
Large Horn, Experimental Pulse Transit Time \approx 1 nsec, Pulse Width \approx 2 nsecs							
Ranking by:		# Elements ↓↑	Design ↔	# Elements ↓↑	Design ↔	# Elements ↓↑	Design ↔
1		2	1	1	3	3	2
2		1	1	2	3	1	2
4		3	1	3	3	2	2
Large Horn, Gaussian Transit Time \approx 1 nsec, Pulse Width \approx .1 nsecs							
Ranking by:		# Elements ↓↑	Design ↔	# Elements ↓↑	Design ↔	# Elements ↓↑	Design ↔
1		3	3	2	1	3	2
2		1	3	1	2	1	1
4		2	3	3	2	2	1
Small Horn Transit Time \approx .1 nsec, Pulse Width \approx .035 nsecs							
Ranking by:		# Elements ↓↑	Design ↔	# Elements ↓↑	Design ↔	# Elements ↓↑	Design ↔
1		3	2	3	3	3	1
2		1	2	1	3	1	1
4		2	2	2	3	2	1

Observing the data in this fashion leads to two conclusions. The first is that the peak field value is dependent on the pulse width and the transit time of the horn. The second is that the benefits by the 2-element exponential designs over the baseline design consistently exceed the benefits that the 1-element and 4-element exponential designs experienced over their respective baseline.

Exponential Curves

The data shows that the wider the pulse is, compared to the transit time (as with the large horn excited with the experimental pulse), the greater the influence of the X-directed (height) taper has on the peak field value. Conversely, the Y-directed (width) taper, produces a negative consequence. The double-exponential is a combination of the affects.

When the pulse width is narrow in relationship to transit time (as with the large horn excited with the gaussian pulse), the Y-directed taper has a positive affect, and the X-directed taper a negative influence. The double-exponential advantage is once again a combination of affects.

The final situation results somewhere in between the two above cases (as with the smaller horn). The Y-directed tapered horn only performs slightly poorer then the double-linear model. The X-directed taper drastically improves the performance. The combination of the two tapers improves the performance further.

Transient Arrays

In chapter 4 it is shown that the four-element arrays substantially reduce the ringing affect. The reduction is not as significant between the one and two-element designs. This is also brought to surface in the table. In every case, except one, the two-element arrays had a greater increase over their respective baselines, than did the 4-element arrays over their respective baselines. In some cases, after scaling down of the four-element, the two-element had a higher peak value. An example is shown in Figure 59. This confirms the conclusion that the higher peak values are the result of the ringing.

Reduction in Run-Time Study

It was demonstrated that the time for running a full problem could be reduced from 9 hrs to 18 mins, a decrease of approximately 500 minutes. The problem size was reduced from a full horn with a 5mm cell size to a quarter of the horn with a 10mm cell size. The transient response showed a fairly accurate reproduction for the early time portion of the pulse. In the frequency-domain, the PSD showed an approximate 10 to 15 dB decrease in the frequencies between 1.4GHz and 4GHz, but the pattern is maintained.

Summary of Conclusions

The ringing affect made it difficult to identify reductions in reflections. When they could be identified the same ratios (between baseline and exponential design) were maintained between initial and reflected pulses. The difference in field strengths is attributed to the timing between the initial pulse and the peak of the periodic ringing. The transit times (a function of conductor lengths) and the pulse width create the timing issue. Additional elements decrease the ringing affect. The decrease between one-element horns and 2-element horns is not that significant, but the jump to 4-element reduces the ringing dramatically.

Suggestions for Further Research

Although the taper designs were not optimized in any fashion, great care was taken to model them as accurately as possible. The limitation is the stair-step representation. A finer grid may enhance the characteristics of each configuration. Care in choosing a mesh size would have to be exercised. Run-times may become prohibitive. Anastasia meshed the small horn at the smallest cell size allowable, so another meshing method would need to be employed.

Assuming the exponential models accurately represent the desired design, optimizing the tapers according to the curves theoretically determined in [33] and

repeating the procedure developed in this effort would prove an interesting research topic.

The results of this project may have demonstrated the reduction of reflections between designs if the ringing affect had not hampered this effort. Further research would require the use of one of the methods described in Chapter 1 to eliminate the reflections, which cause the ringing affect. To the contrary, another interesting topic maybe to try and optimize the ringing affect to increase peak field strength.

The entire study focused on the boresight radiation in the far-field zone. Further study could include determining which designs have the best off-boresight performance.

The final suggestion has been alluded to throughout this document; combining the FDTD method with an evolutionary algorithm (EA) in order to optimize some feature of these antennas. Some potential areas that affect performance that could be optimized are the aperture dimensions and the length. Following in the path of this research effort, the tapers could be optimized, as well as the pulse-transit time-ringing effect described in the preceding section. Before these numerical methods could be interfaced a further reduction in run-time would be required. Parallel processing may be the answer.

Summary

The goal of this research effort involved the designing, modeling, and numerical testing of 4 different TEM models. The goal was to demonstrate the effects that exponential tapers have on these UWB radiators and their respective arrays using the FDTD method. By using 2 dimensionally different TEM horns and three excitation pulses, characteristic of each were compared. This was accomplished after it was determined that base-line models produced results similar to the experimental data.

Comparing the exponential-designs to their respective baselines led to three conclusions.

- 1) The exponential designs did not reduce reflections.
- 2) Reflecting surface currents produced a ringing affect in the antenna.
Depending on the pulse width and the transit time, the field created by the ringing could enhance peak field strengths. The pulse width and exponential taper could be combined to optimize the peak value.
- 3) Four-element arrays reduce the ringing effect substantially over single element horns and 2-element arrays. Going from a one element to 2-elements does not provide an equivalent reduction.

This study also took the first steps towards optimizing the horns with an EA by showing that significant reductions in run-times could be achieved by using mirror boundary conditions, different cell sizes, number of time-steps, and specification of desired output.

Appendix A

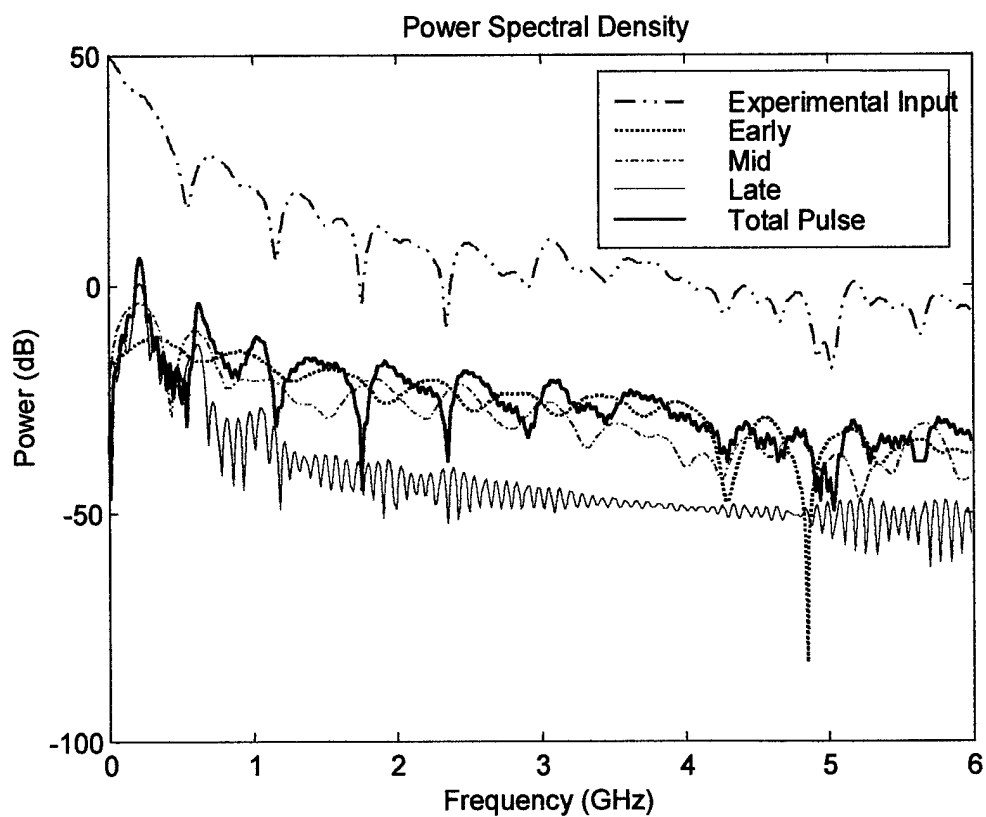


Figure A-1. Frequency Response Resulting from Segmentation of Total Transient Response (Experimental Pulse)

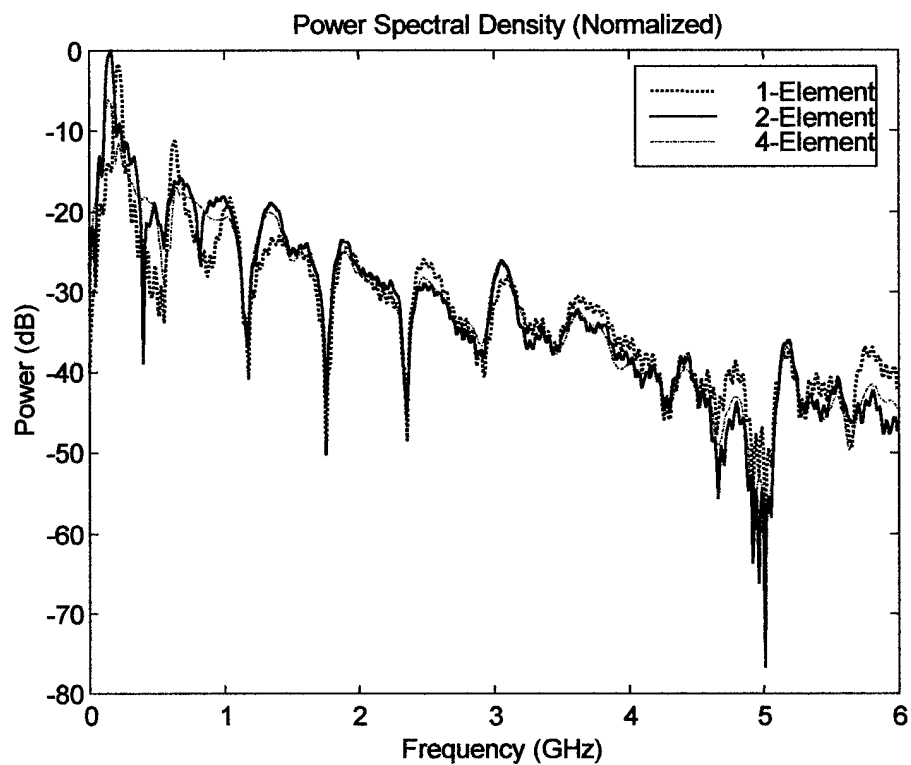


Figure A-2. PSD Comparison of 1, 2, and 4 Element Arrays
Large Horn (Experimental Input Pulse)

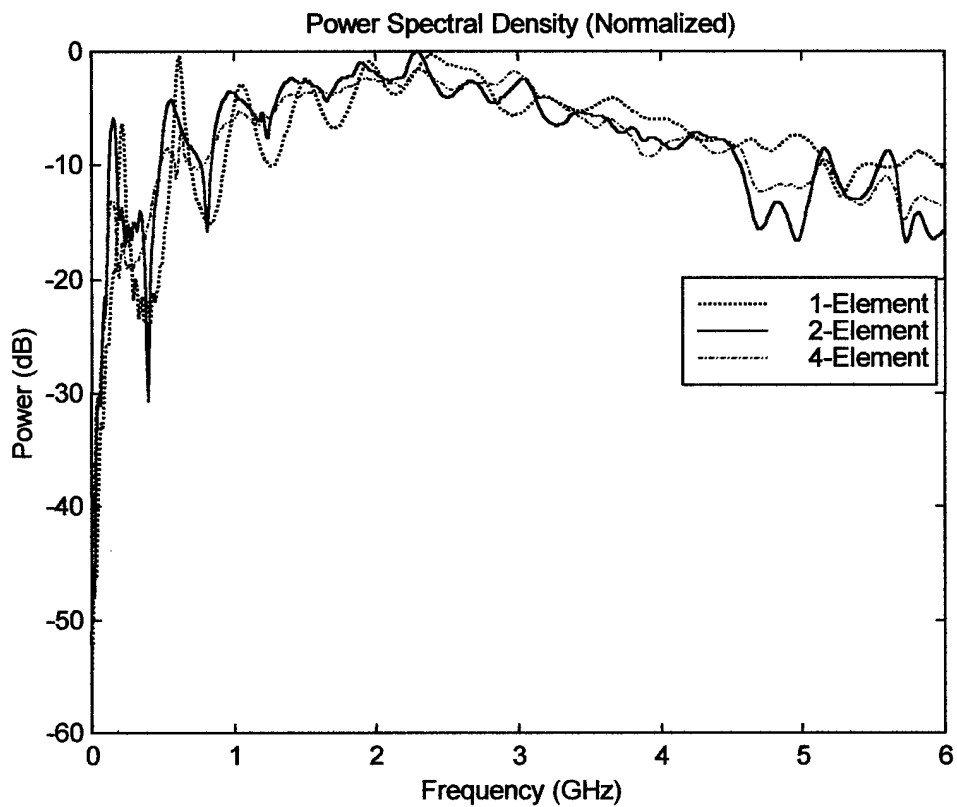


Figure A-3. PSD Comparison of 1, 2, and 4 Element Arrays
Large Horn (Gaussian Input Pulse)

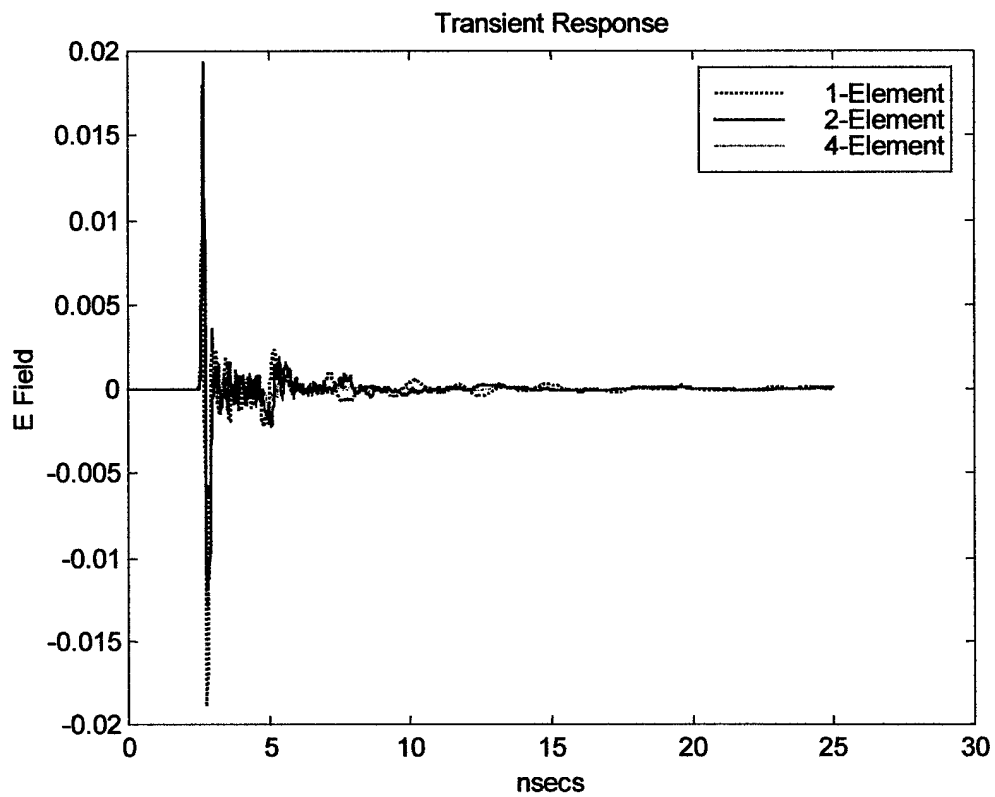


Figure A-4. Transient Response Comparison of 1, 2, and 4 Element Arrays
Large Double-Linear (Gaussian Input Pulse)

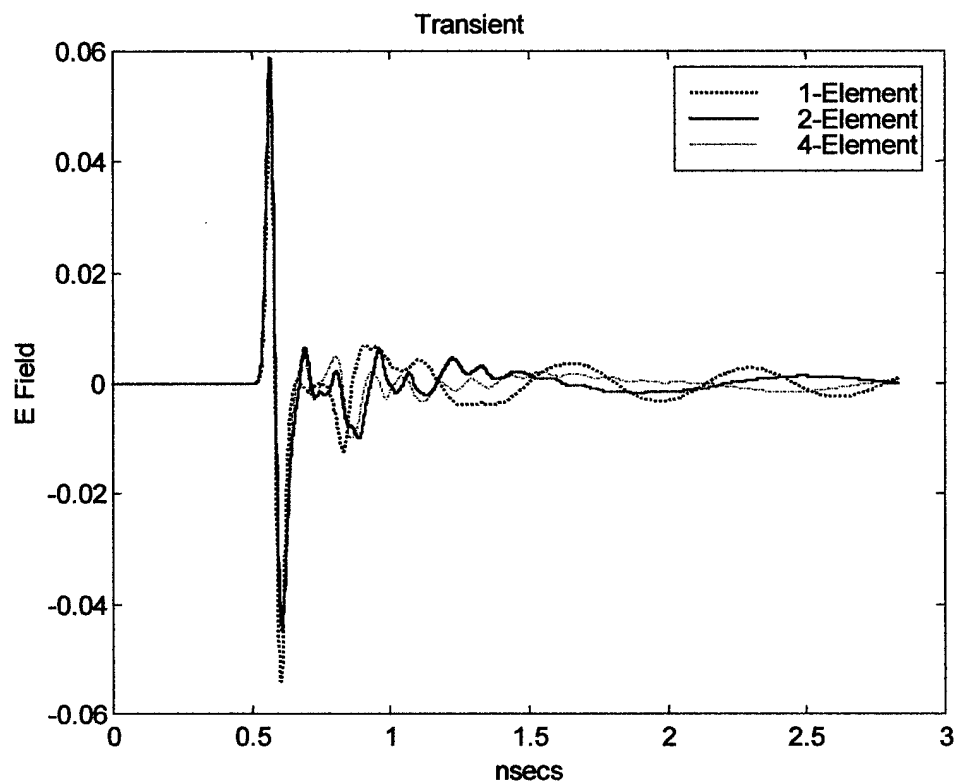


Figure A-5. Transient Response Comparison of 1, 2, and 4 Element Arrays
Small Double-Linear (Gaussian Input Pulse)

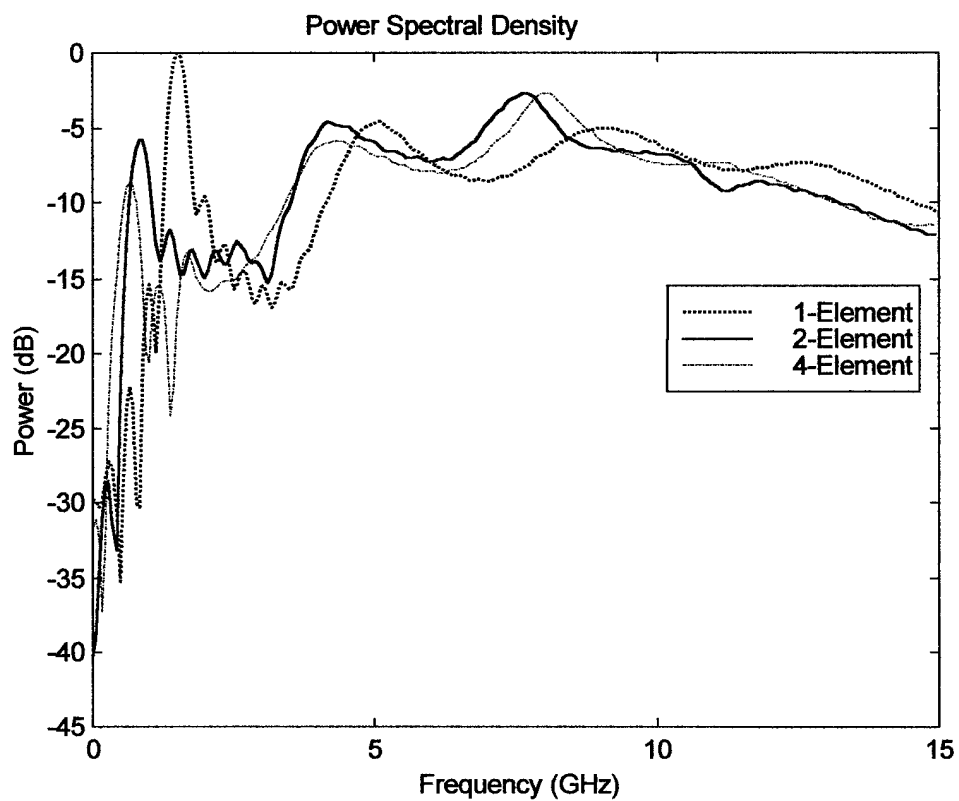


Figure A-6. PSD Comparison of 1, 2, and 4 Element Arrays
Small Horn (Gaussian Input Pulse)

Appendix B

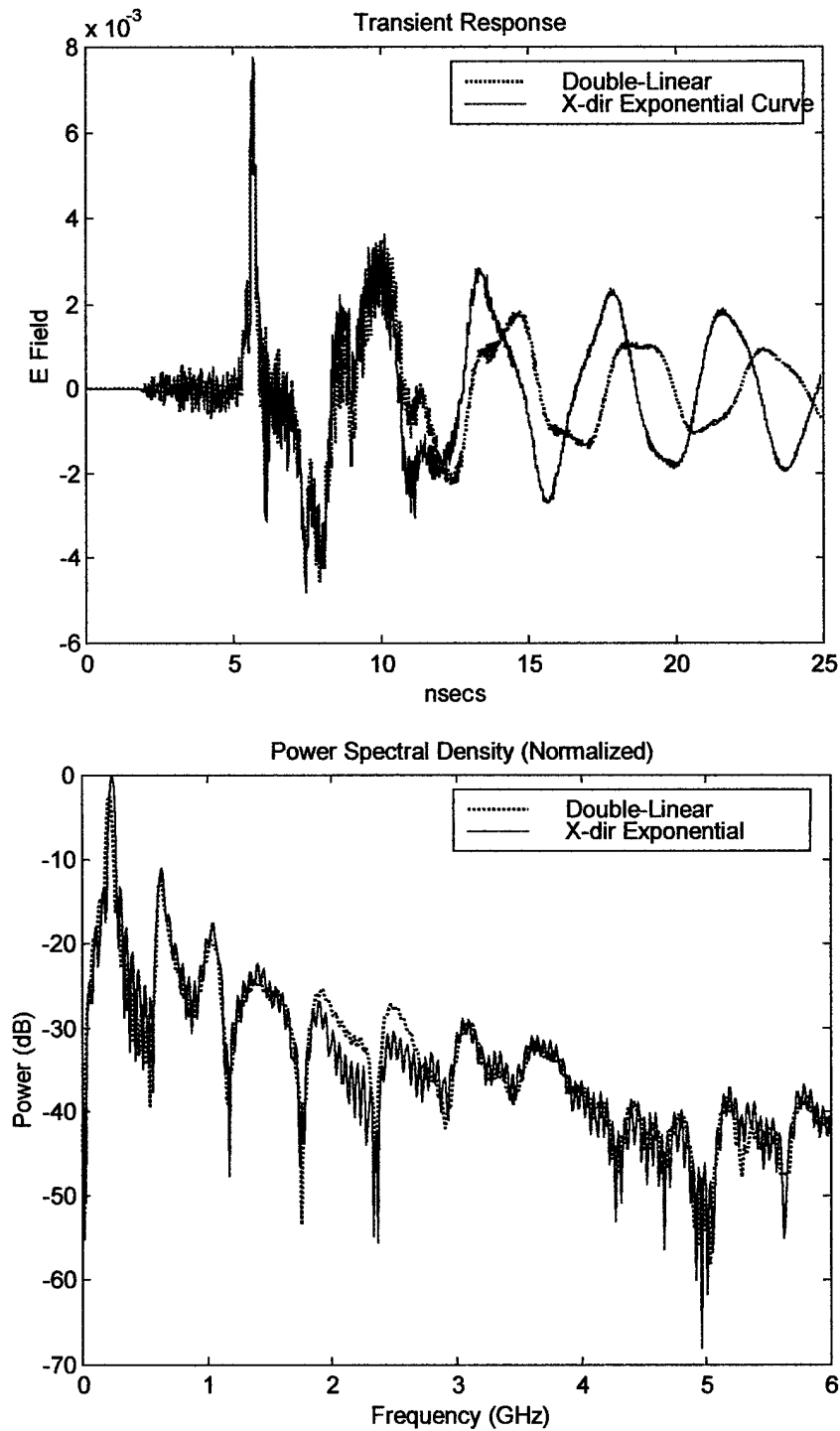


Figure B-1. Comparison of Double-Linear and X-dir Exponential Taper Curve (1-Element, Large Horn, Experimental Input Pulse)

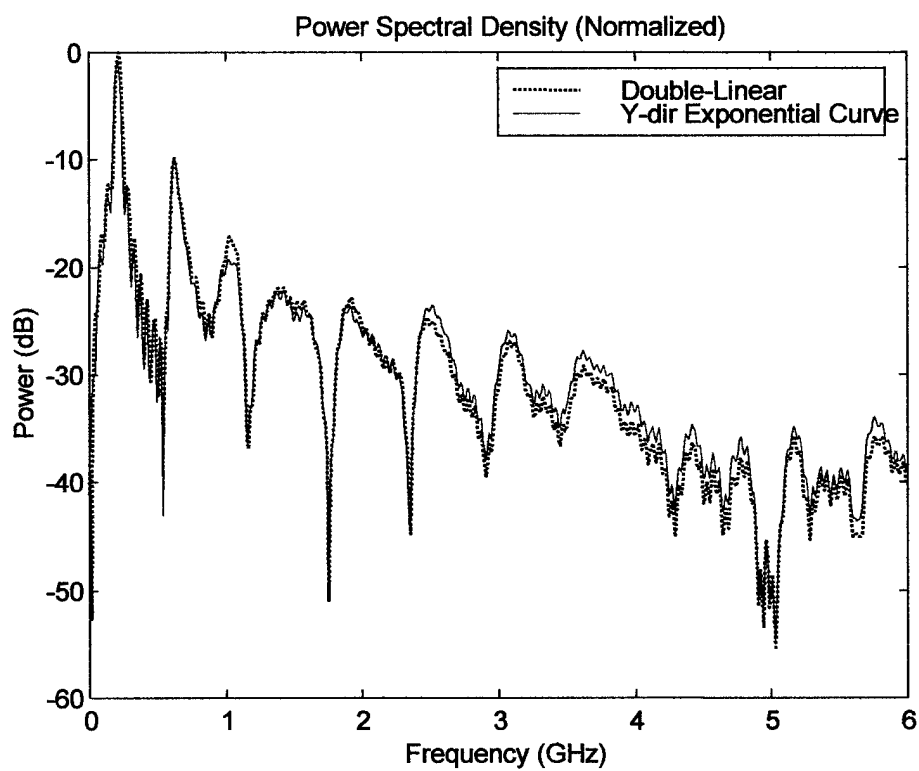
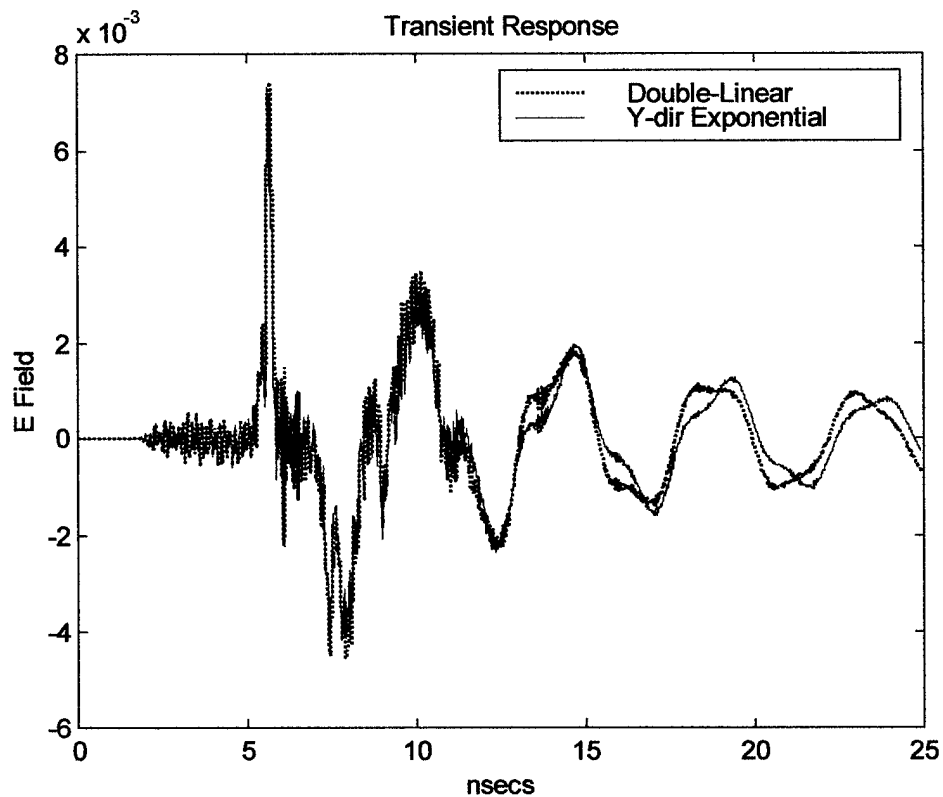


Figure B-2. Comparison of Double-Linear and Y-dir Exponential Taper Curve
(1-Element, Large Horn, Experimental Input Pulse)

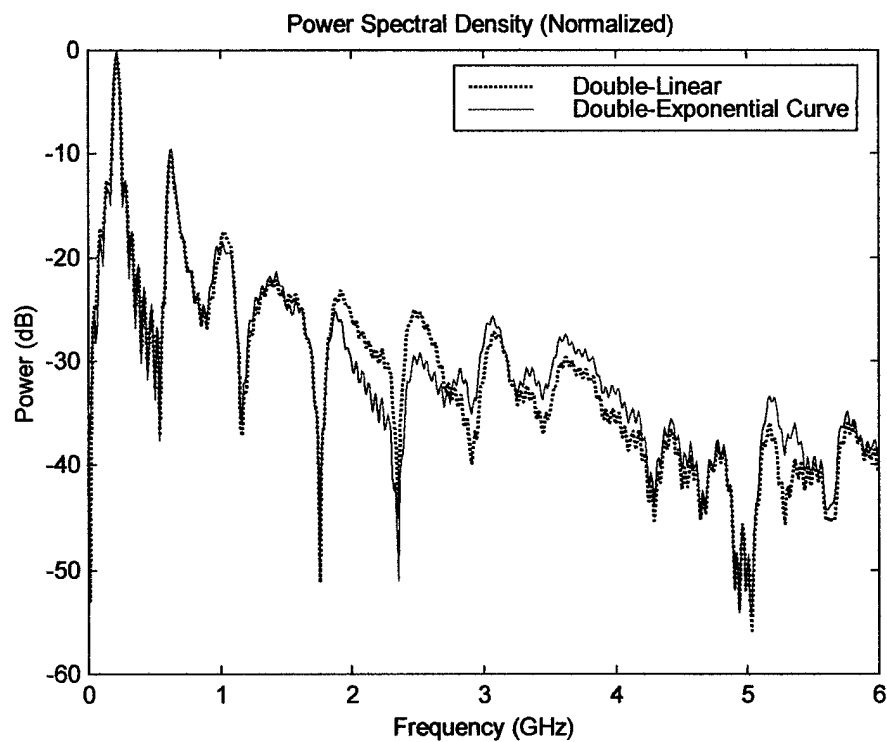
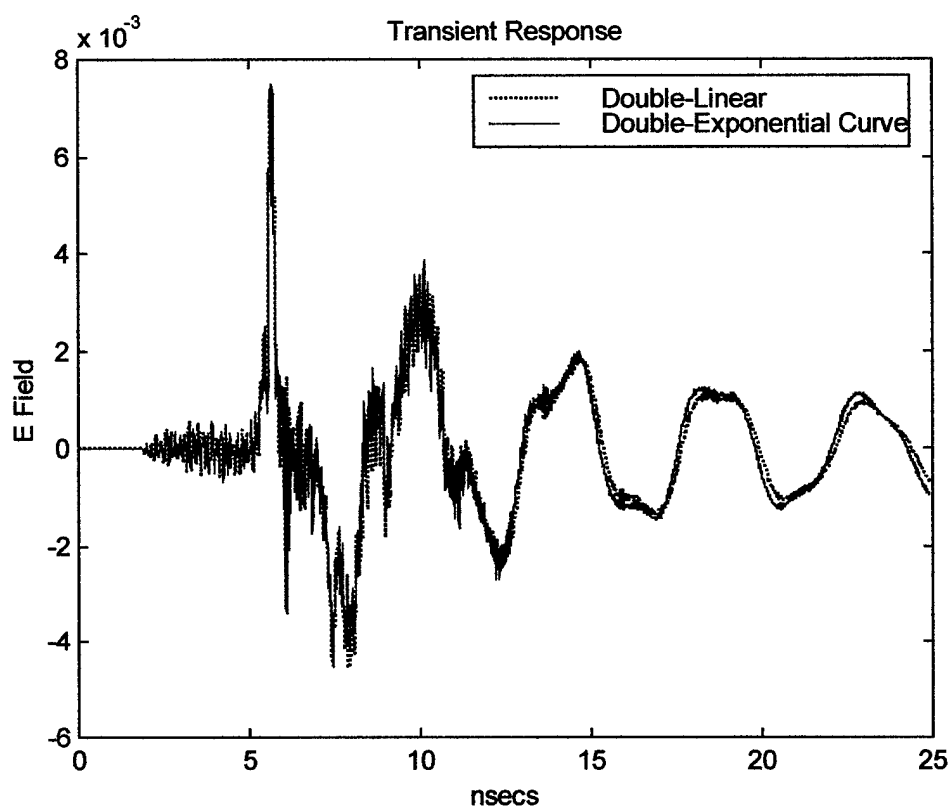


Figure B-3. Comparison of Double-Linear and Double-Exponential Taper Curve
(1-Element, Large Horn, Experimental Input Pulse)

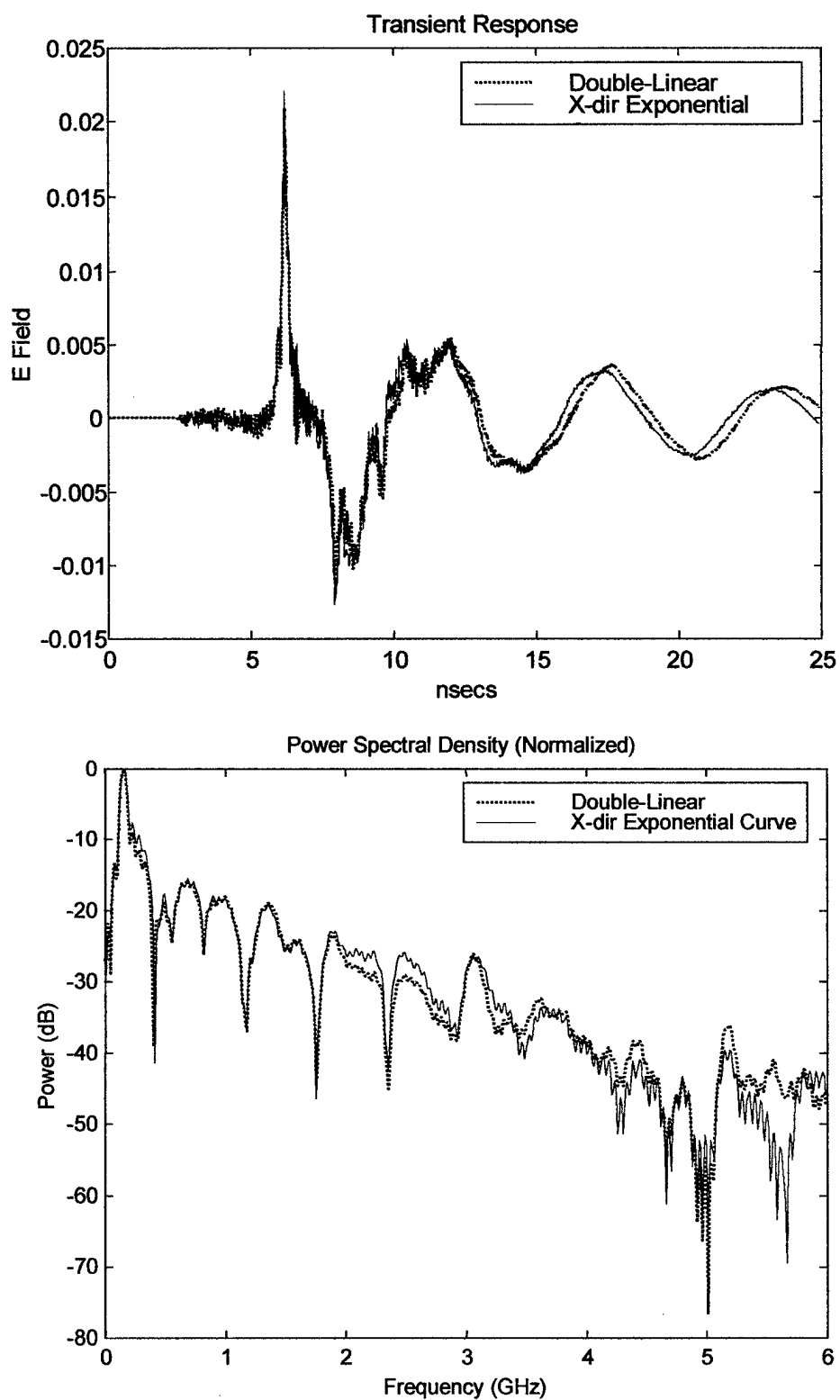


Figure B-4. Comparison of Double-Linear and X-dir Exponential Taper Curve (2-Element, Large Horn, Experimental Input Pulse)

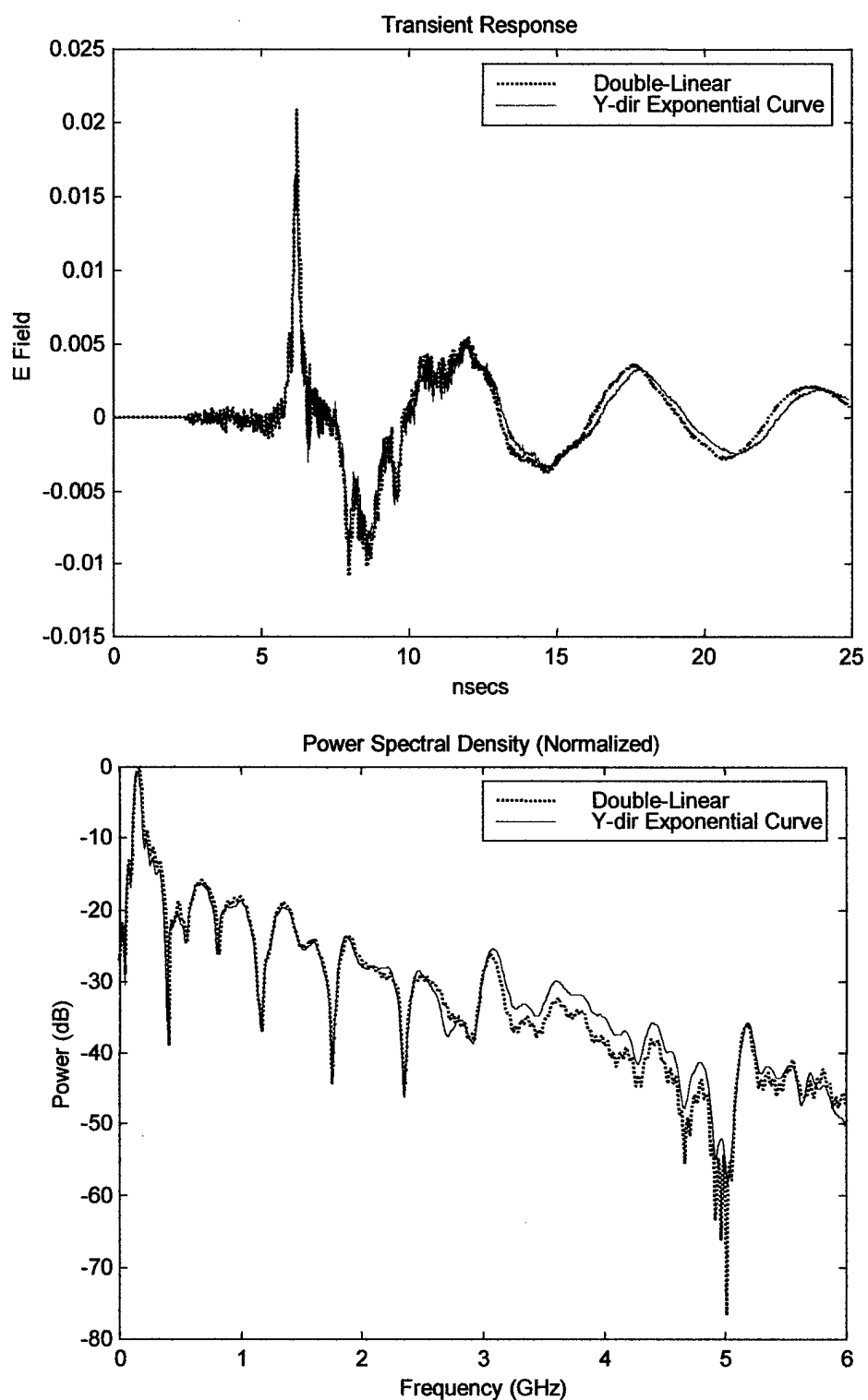


Figure B-5. Comparison of Double-Linear and Y-dir Exponential Taper Curve (2-Element, Large Horn, Experimental Input Pulse)

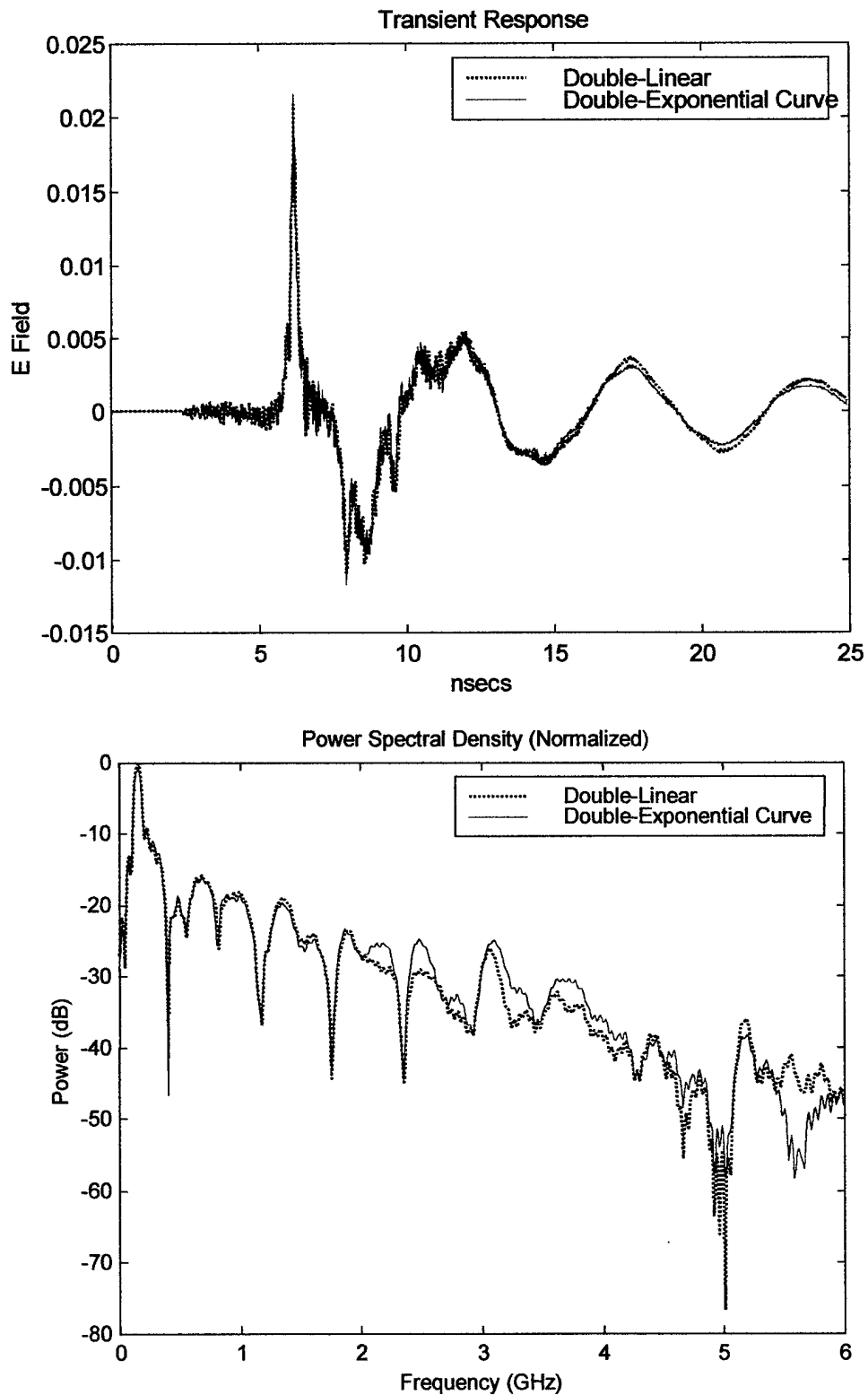


Figure B-6. Comparison of Double-Linear and Double-Exponential Taper Curve (2-Element, Large Horn, Experimental Input Pulse)

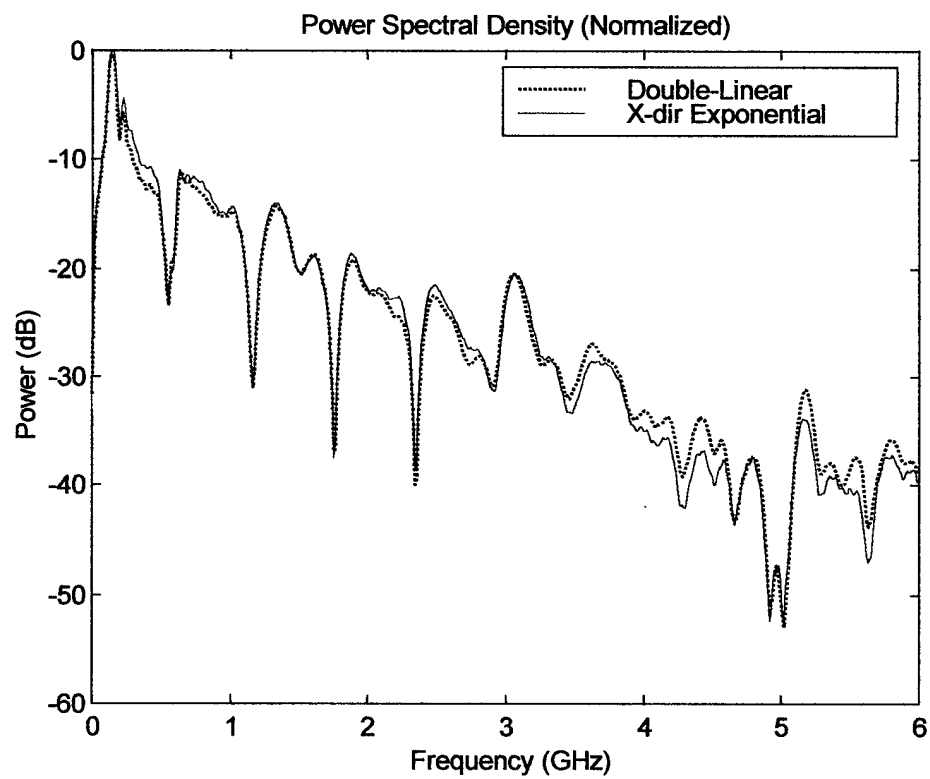
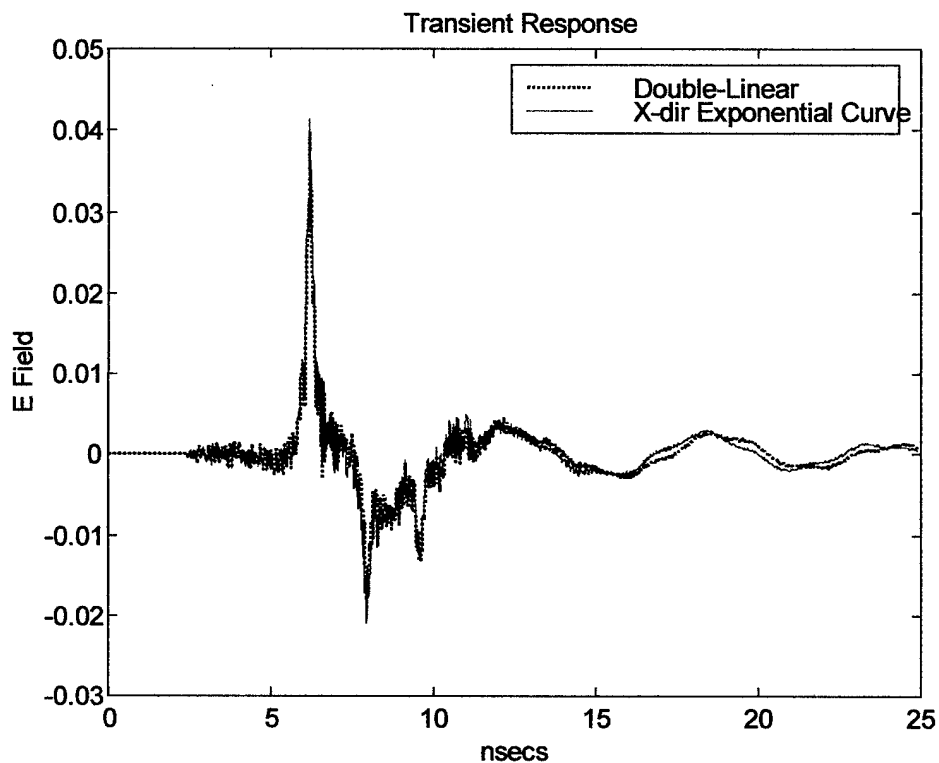


Figure B-7. Comparison of Double-Linear and X-dir Exponential Taper Curve (4-Element, Large Horn, Experimental Input Pulse)

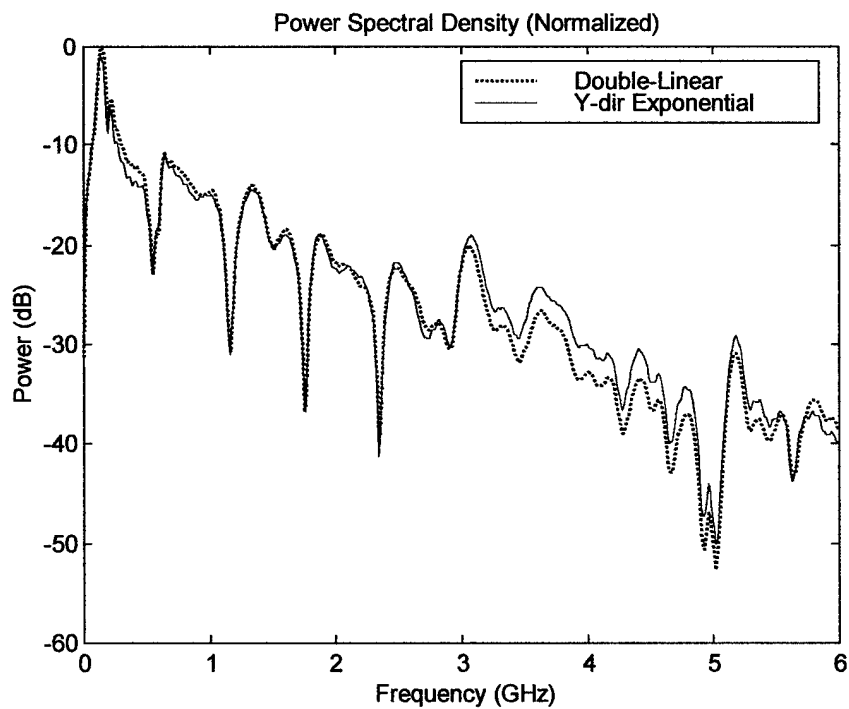
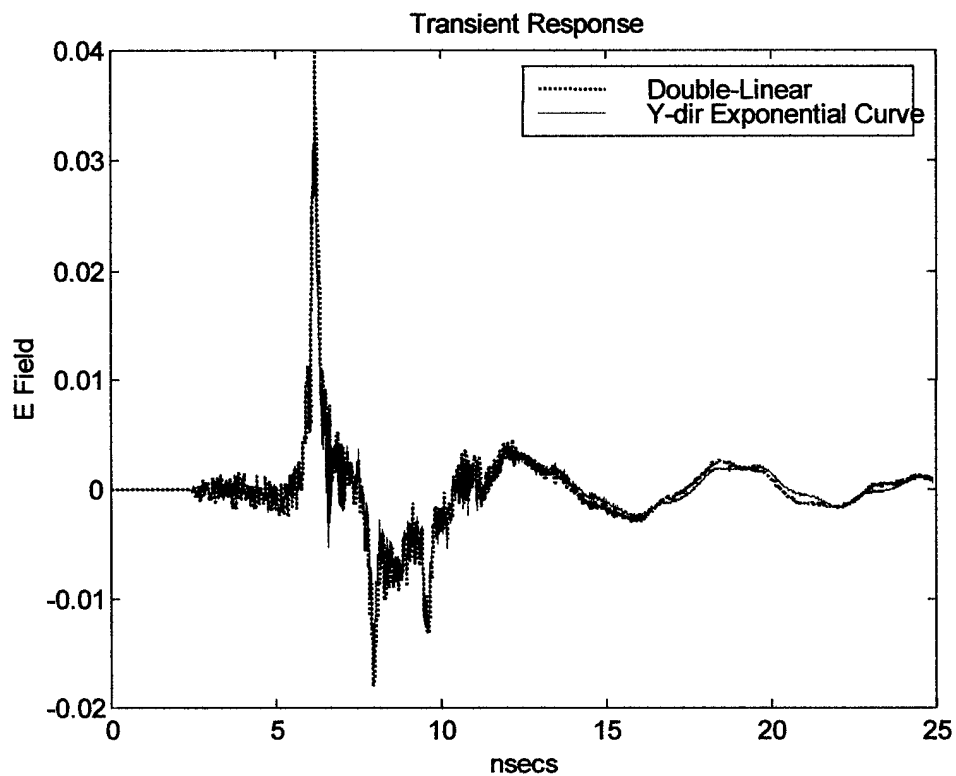


Figure B-8. Comparison of Double-Linear and Y-dir Exponential Taper Curve
(4-Element, Large Horn, Experimental Input Pulse)

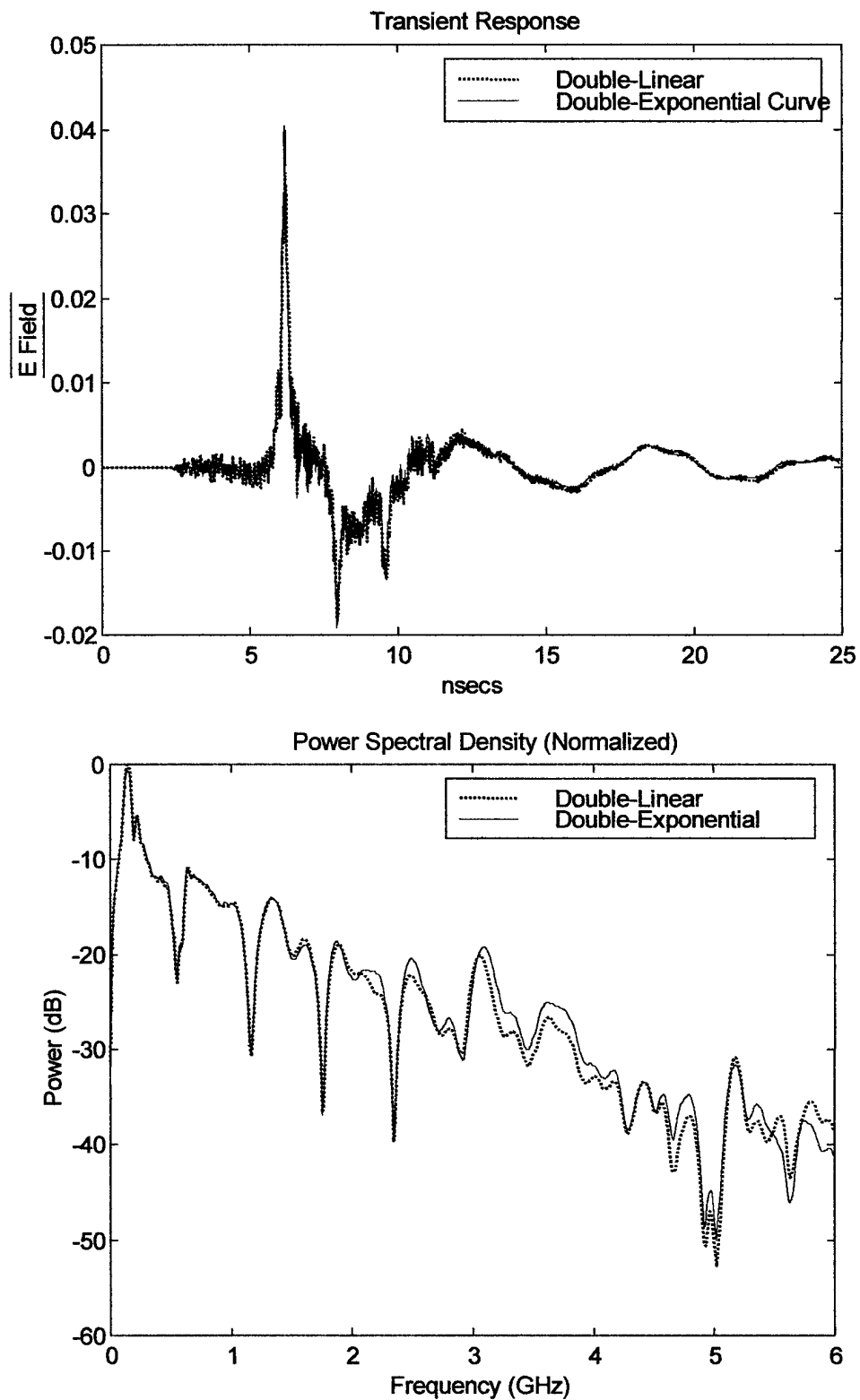


Figure B-9. Comparison of Double-Linear and Double-Exponential Taper Curve (4-Element, Large Horn, Experimental Input Pulse)

Appendix C

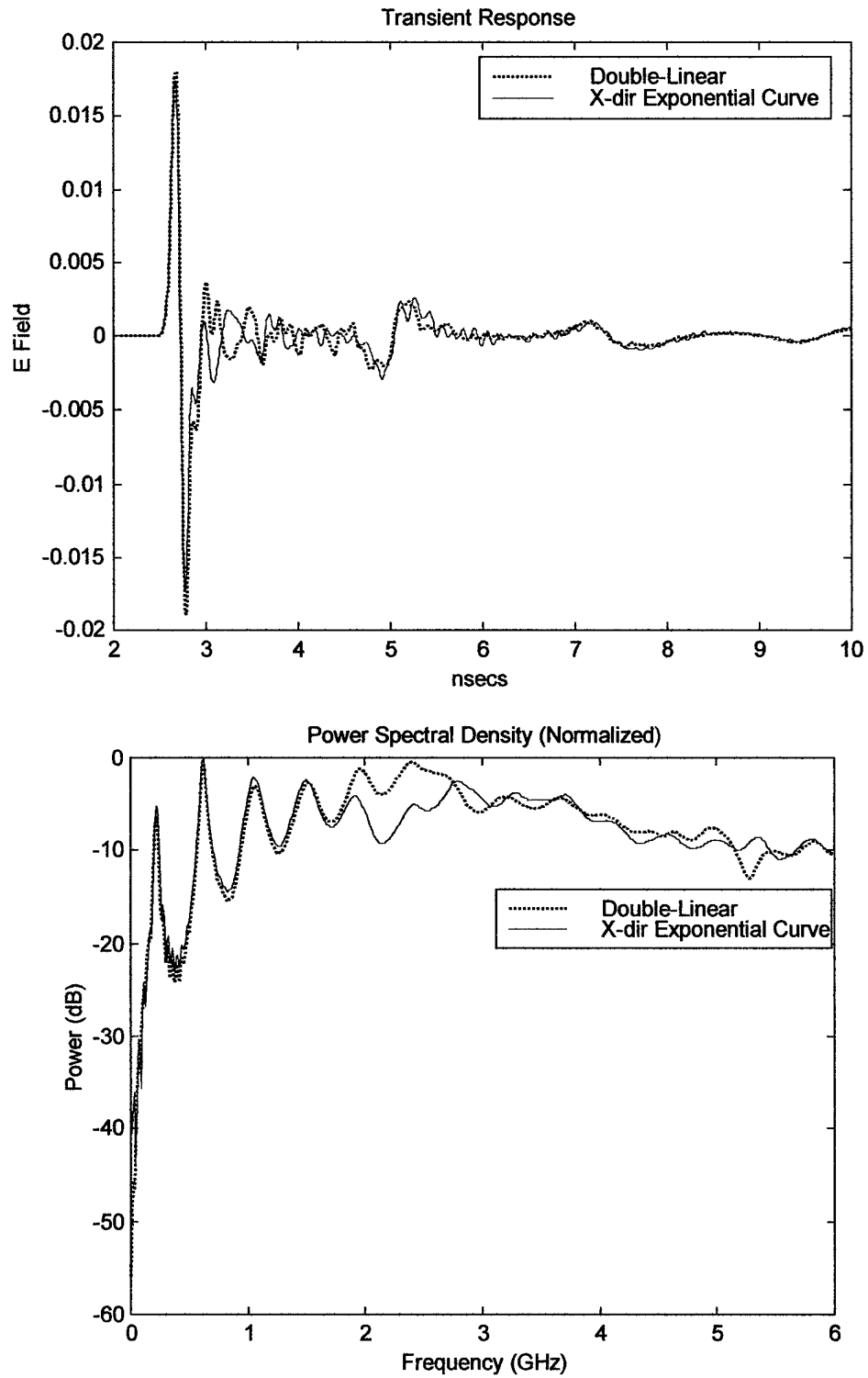


Figure C-1. Comparison of Double-Linear and X-dir Exponential Taper Curve
(1-Element, Large Horn, Gaussian Input Pulse)

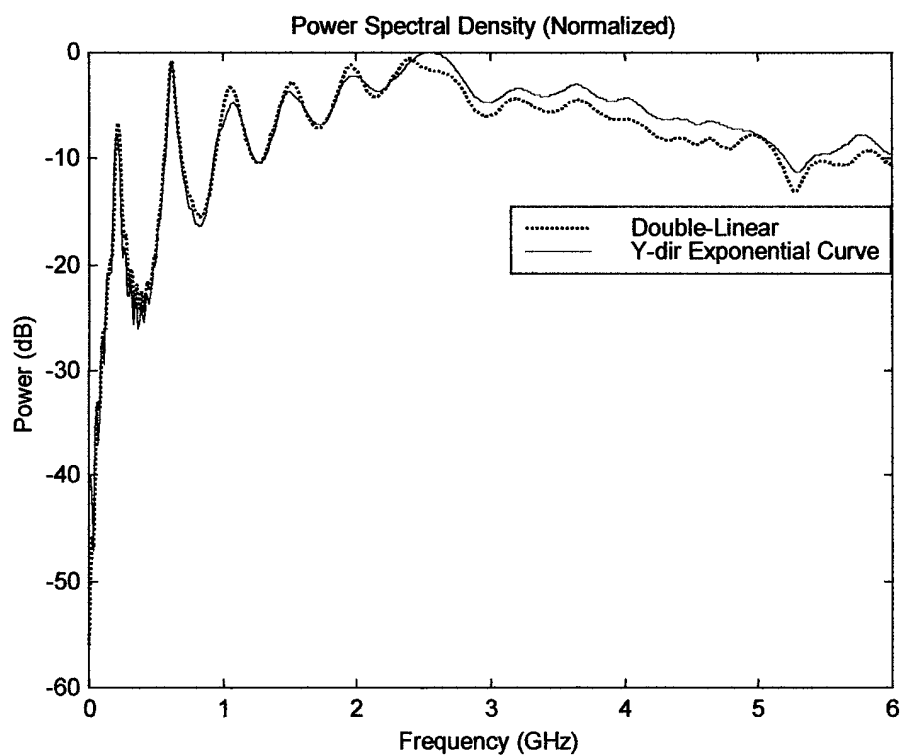
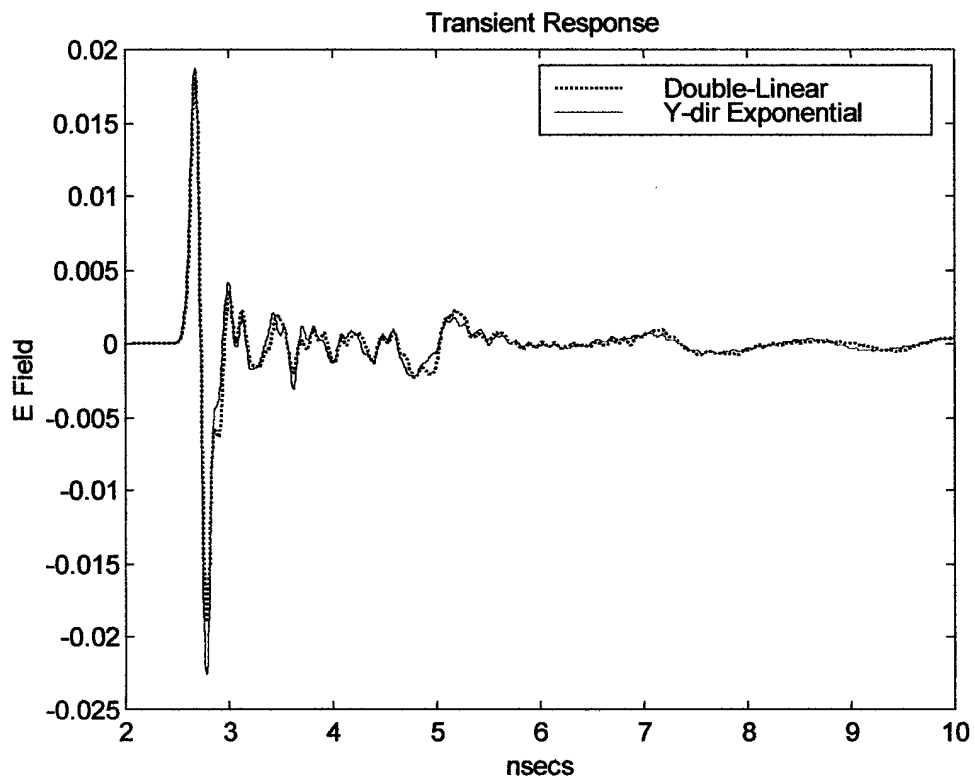


Figure C-2. Comparison of Double-Linear and Y-dir Exponential Taper Curve (1-Element, Large Horn, Gaussian Input Pulse)

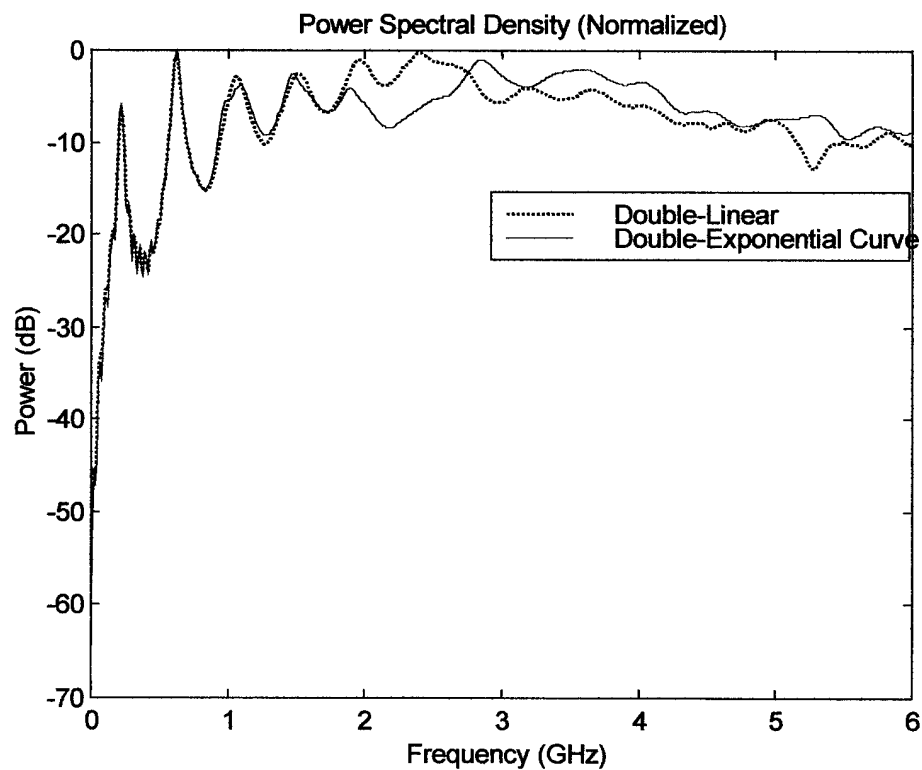
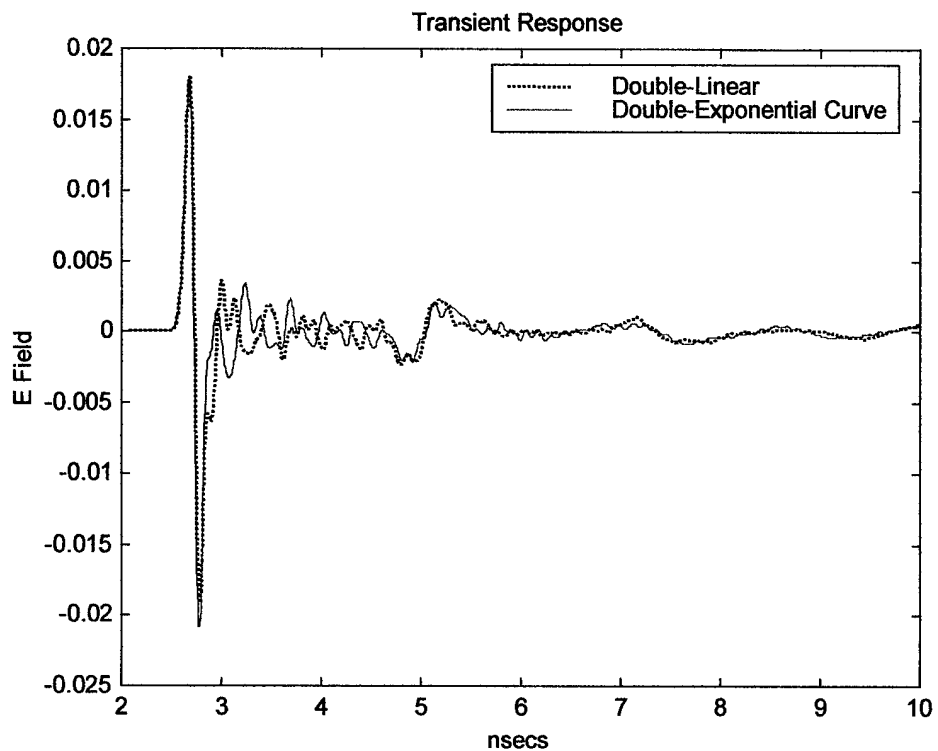


Figure C-3. Comparison of Double-Linear and Double-Exponential Taper Curve (1-Element, Large Horn, Gaussian Input Pulse)

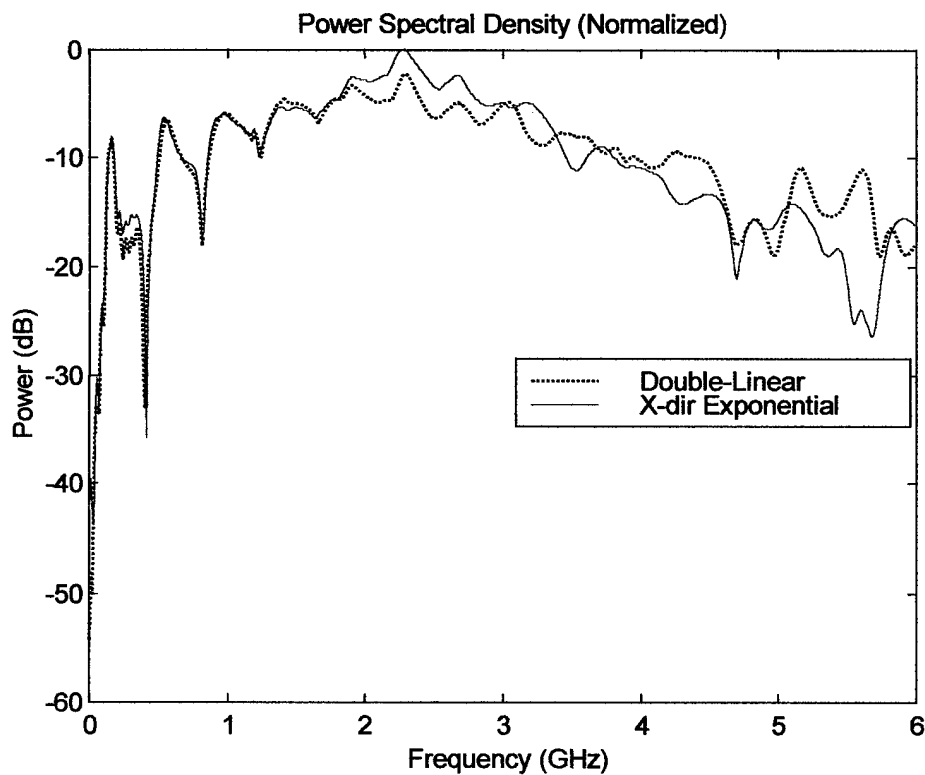
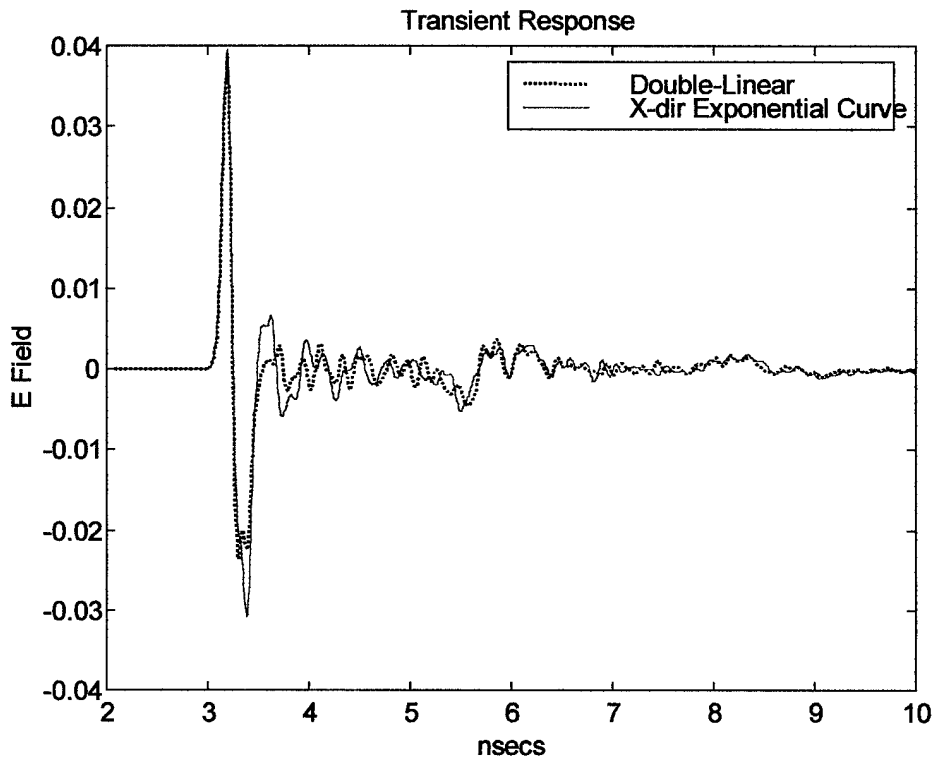


Figure C-4. Comparison of Double-Linear and X-dir Exponential Taper Curve (2-Element, Large Horn, Gaussian Input Pulse)

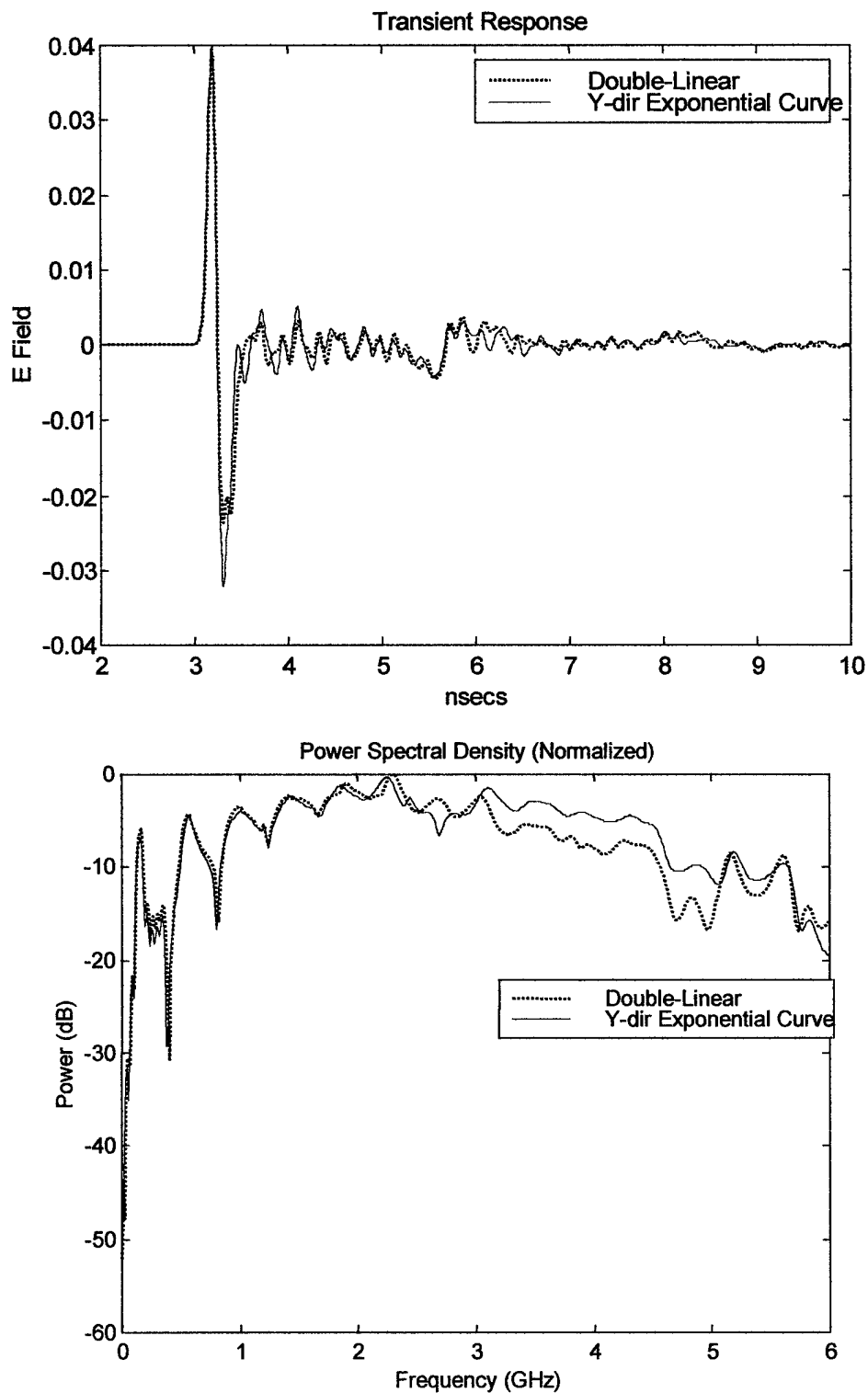


Figure C-5. Comparison of Double-Linear and Y-dir Exponential Taper Curve (2-Element, Large Horn, Gaussian Input Pulse)

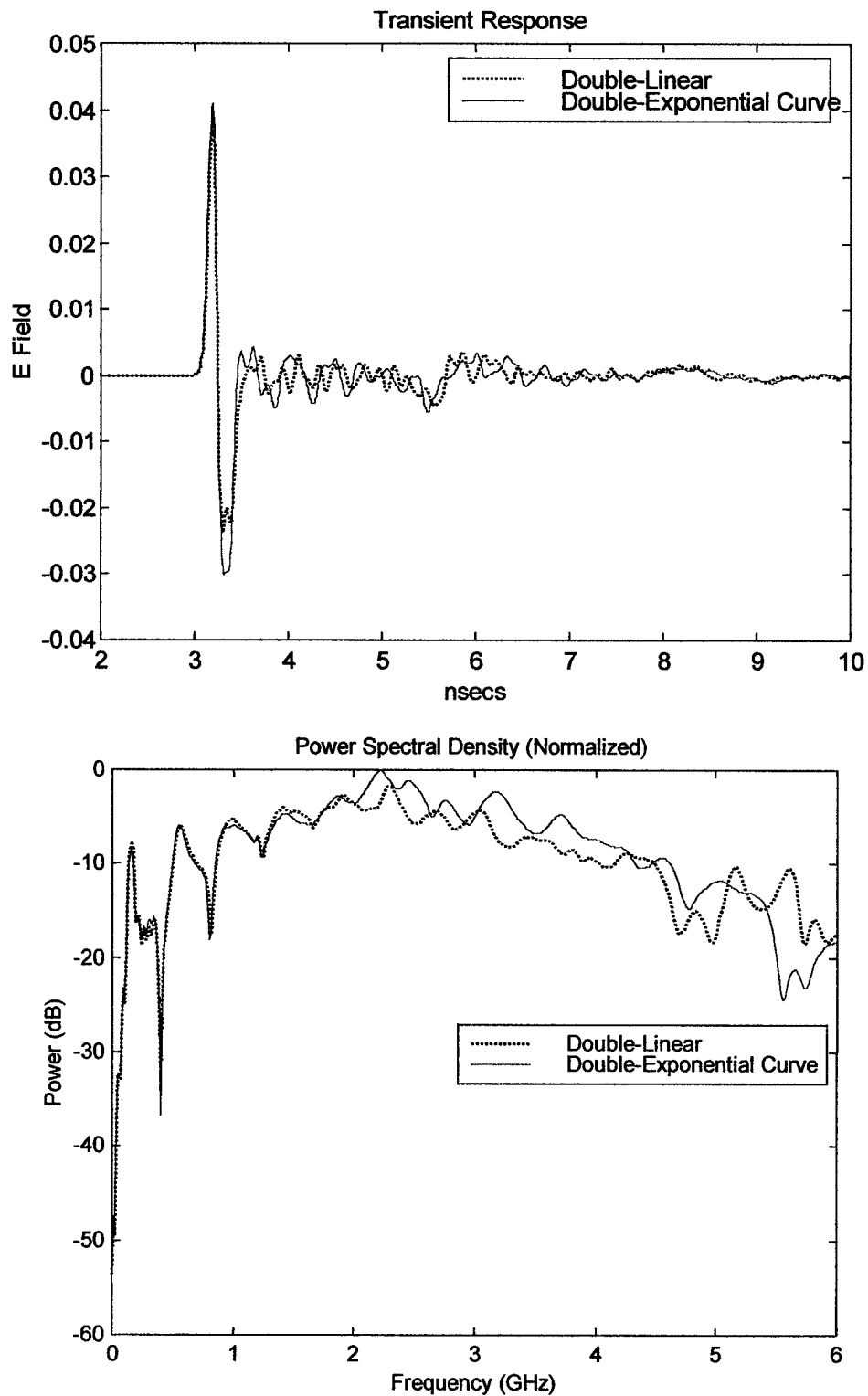


Figure C-6. Comparison of Double-Linear and Double-Exponential Taper Curve
 (2-Element, Large Horn, Gaussian Input Pulse)

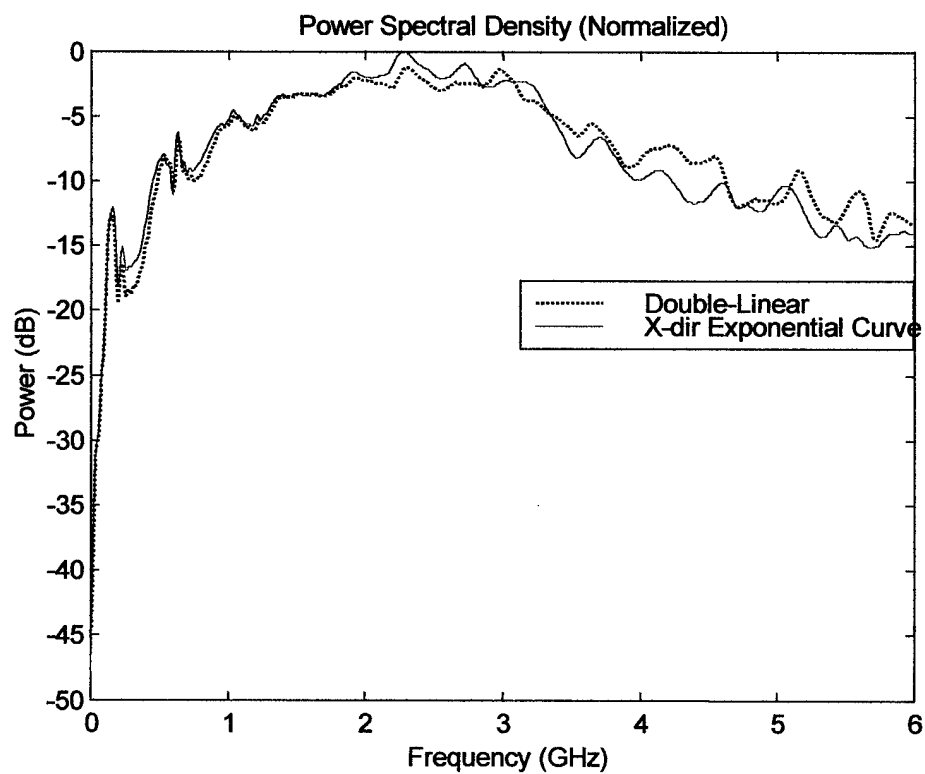
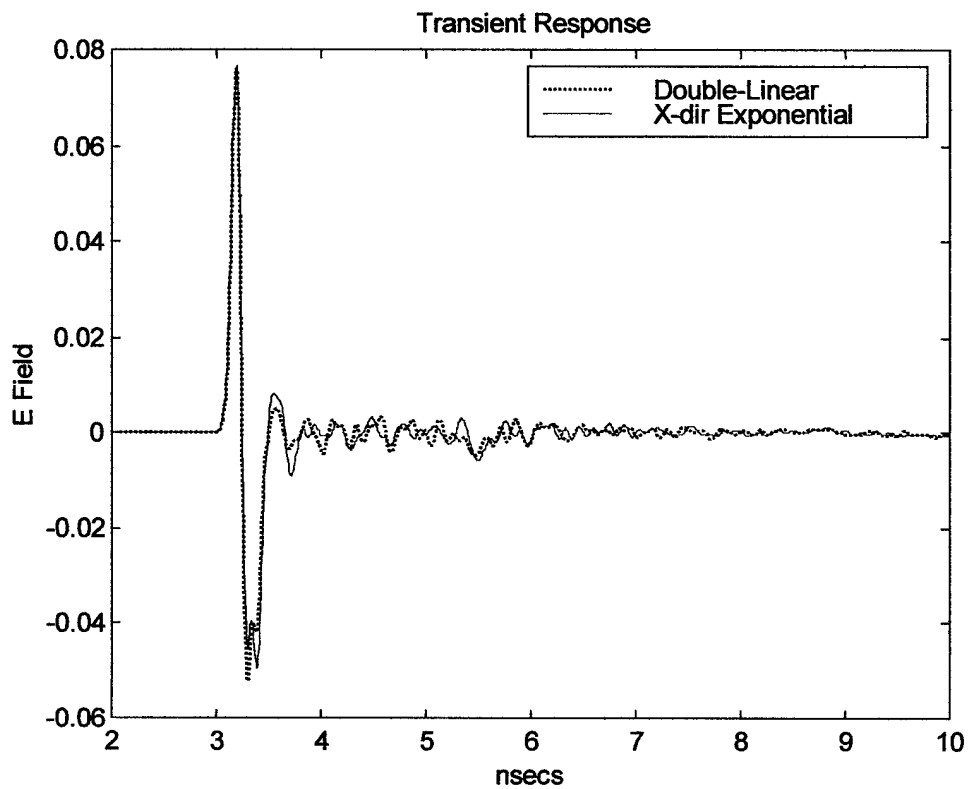


Figure C-7. Comparison of Double-Linear and X-dir Exponential Taper Curve (4-Element, Large Horn, Gaussian Input Pulse)

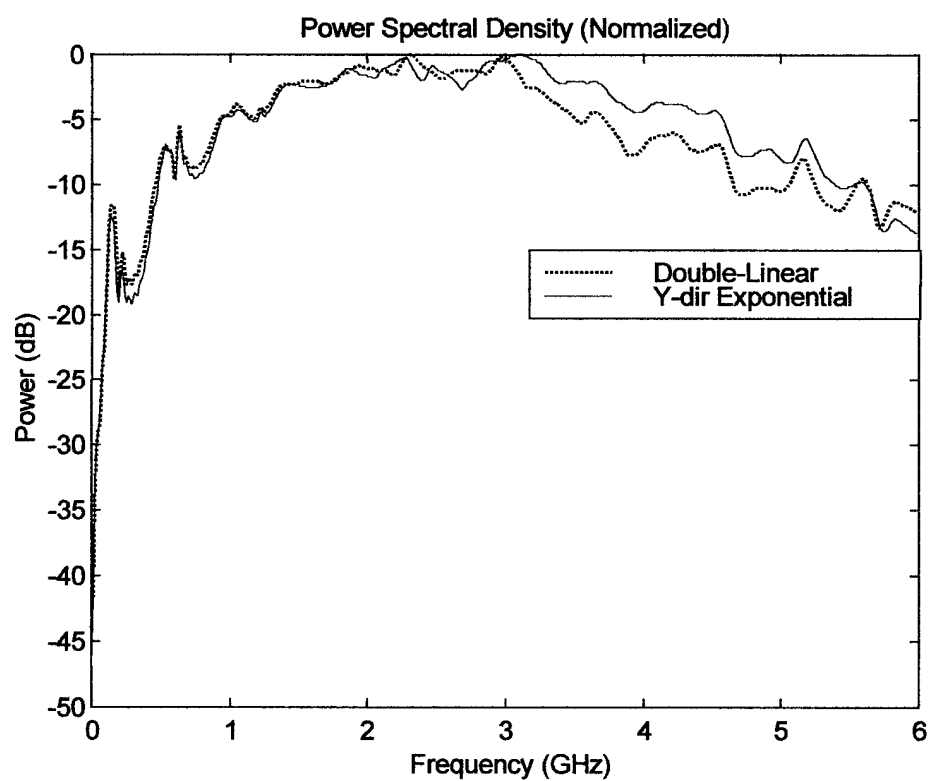
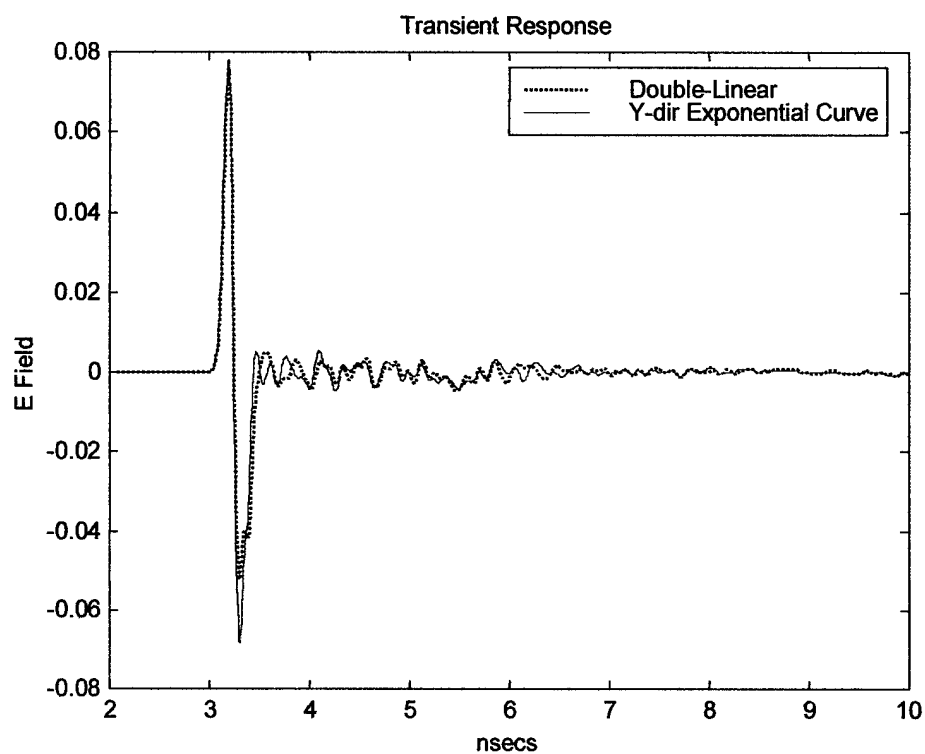


Figure C-8. Comparison of Double-Linear and Y-dir Exponential Taper Curve (4-Element, Large Horn, Gaussian Input Pulse)

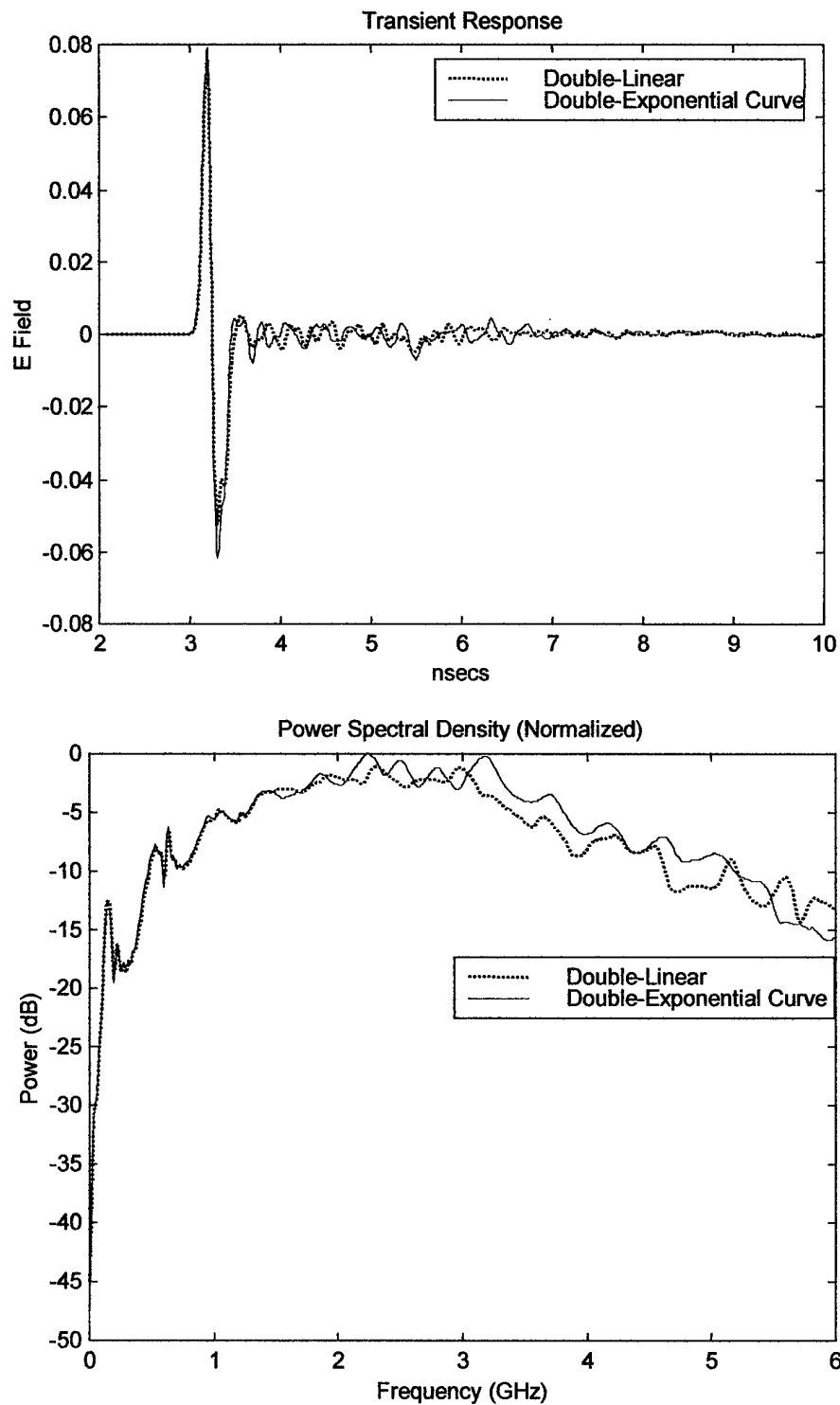


Figure C-9. Comparison of Double-Linear and Double-Exponential Taper Curve (4-Element, Large Horn, Gaussian Input Pulse)

Appendix D

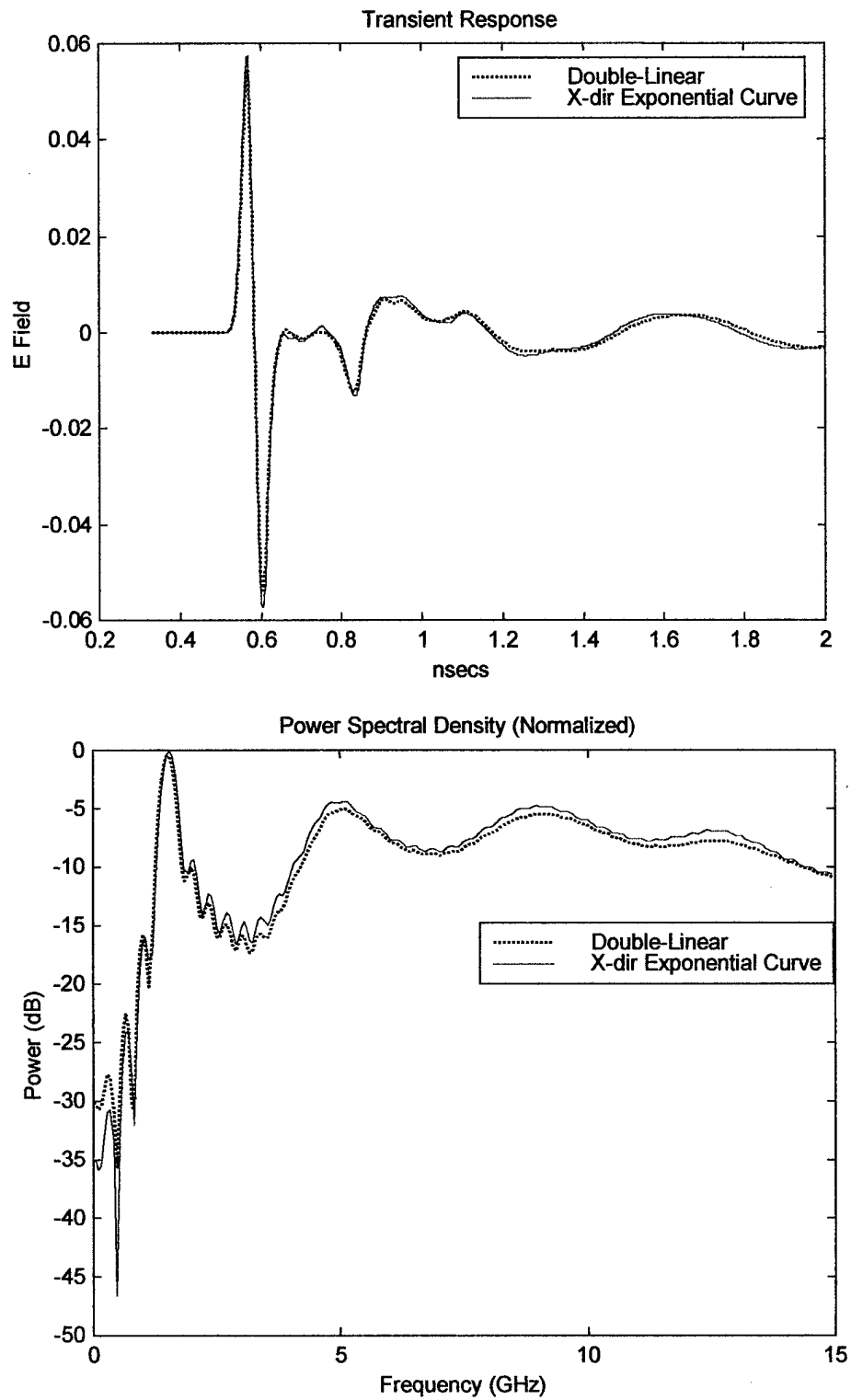


Figure D-1. Comparison of Double-Linear and X-dir Exponential Taper Curve
(1-Element, Small Horn, Gaussian Input Pulse)

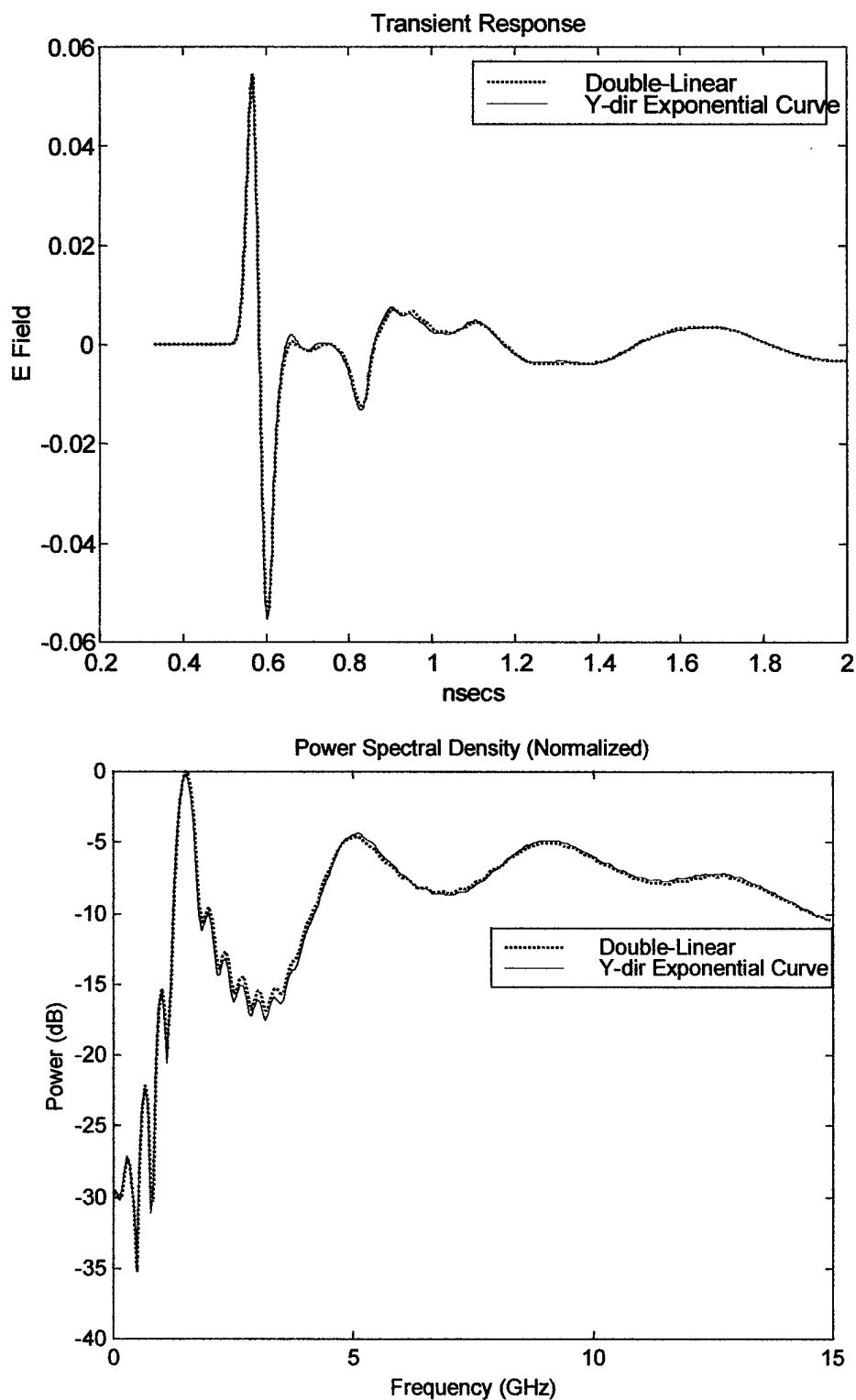


Figure D-2. Comparison of Double-Linear and Y-dir Exponential Taper Curve (1-Element, Small Horn, Gaussian Input Pulse)

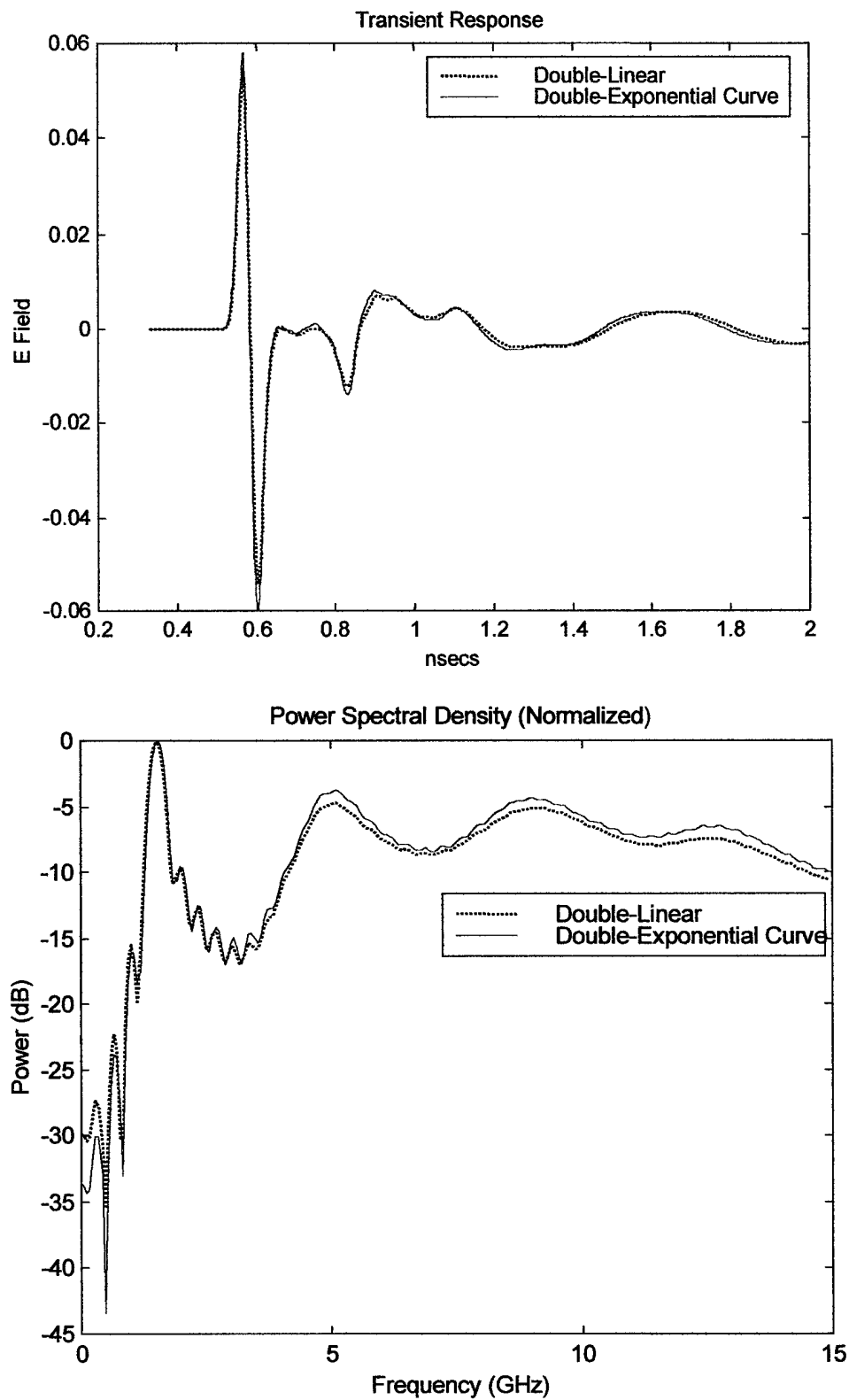


Figure D-3. Comparison of Double-Linear and Double-Exponential Taper Curve
(1-Element, Small Horn, Gaussian Input Pulse)

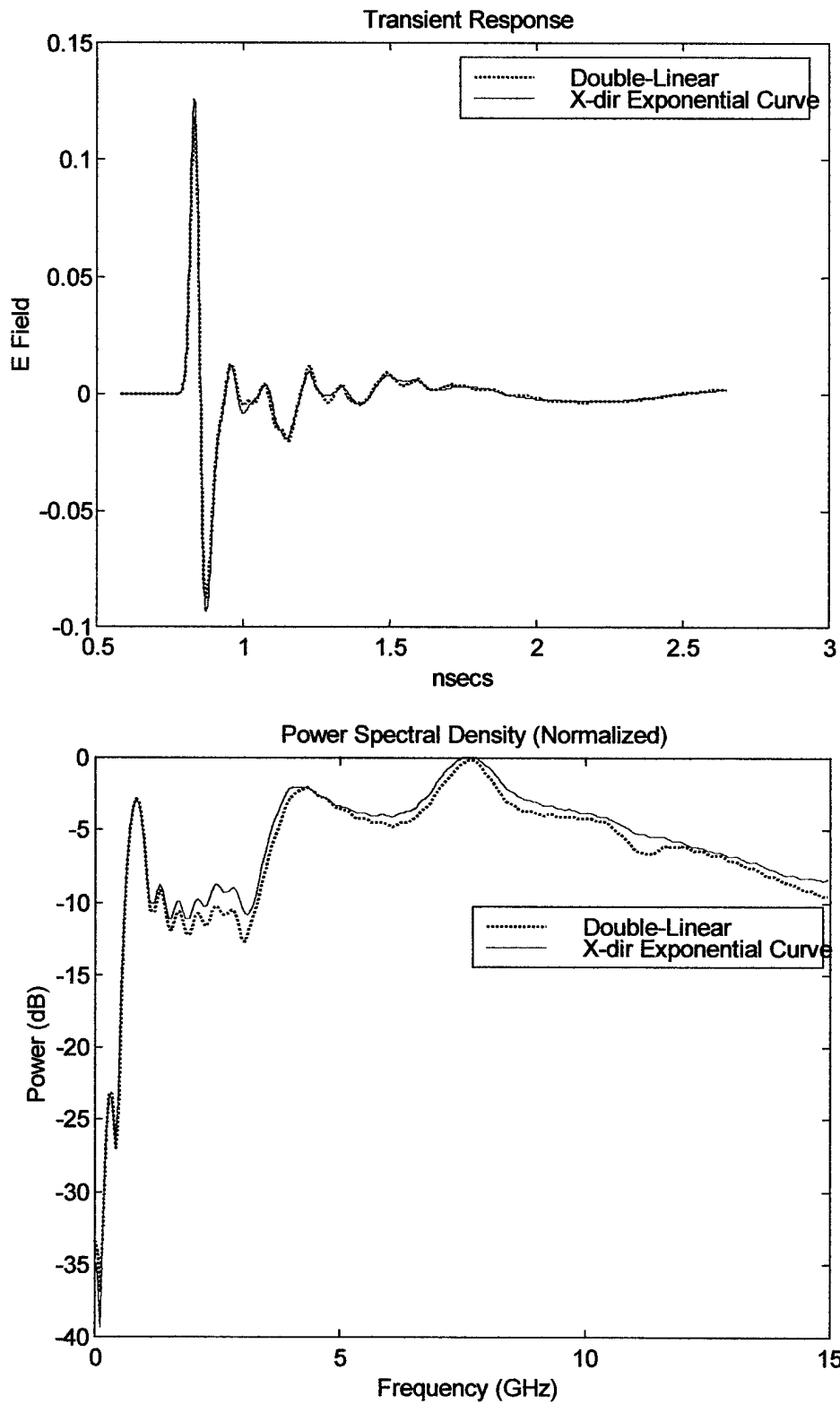


Figure D-4. Comparison of Double-Linear and X-dir Exponential Taper Curve
(2-Element, Small Horn, Gaussian Input Pulse)

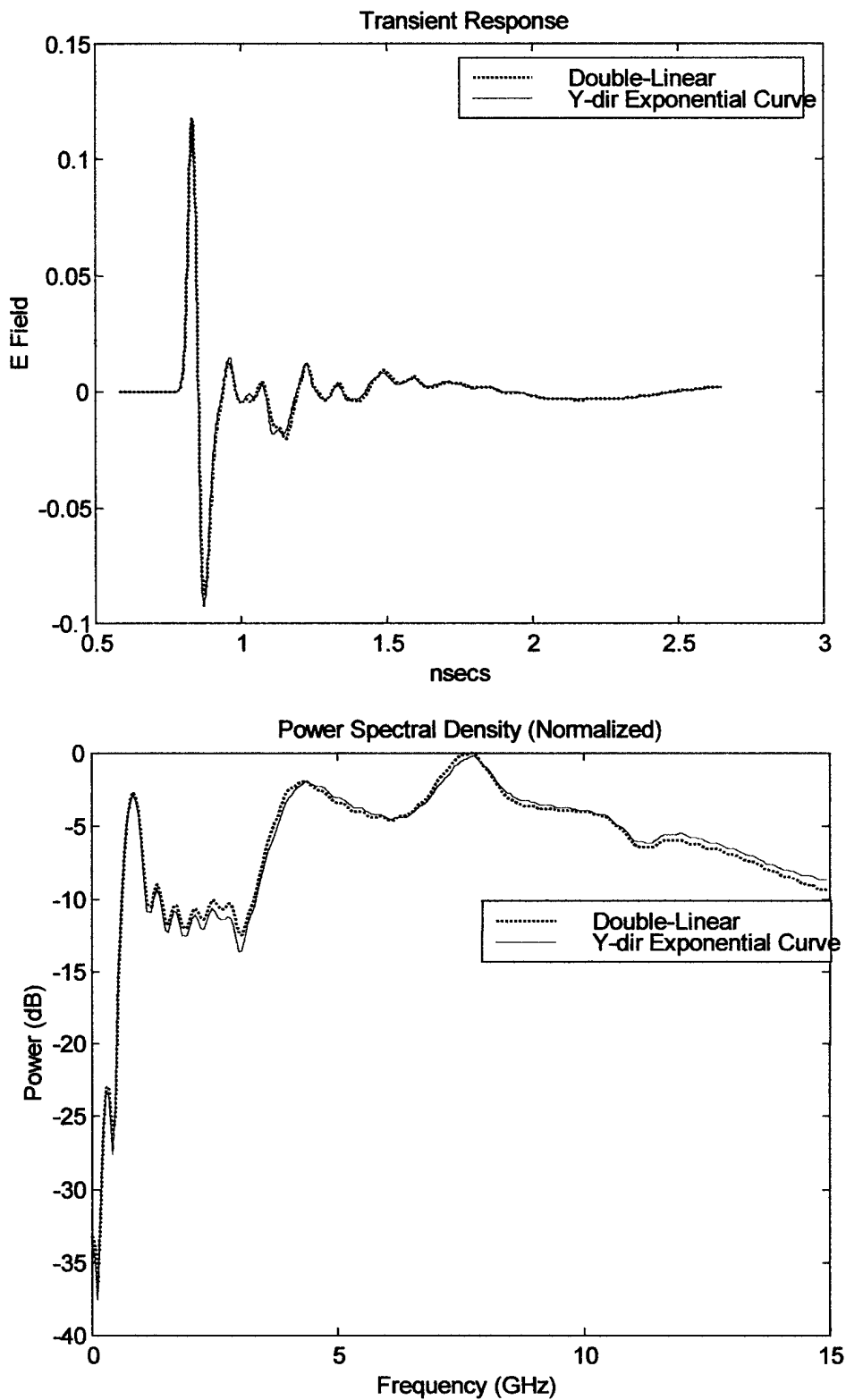


Figure D-5. Comparison of Double-Linear and Y-dir Exponential Taper Curve (2-Element, Small Horn, Gaussian Input Pulse)

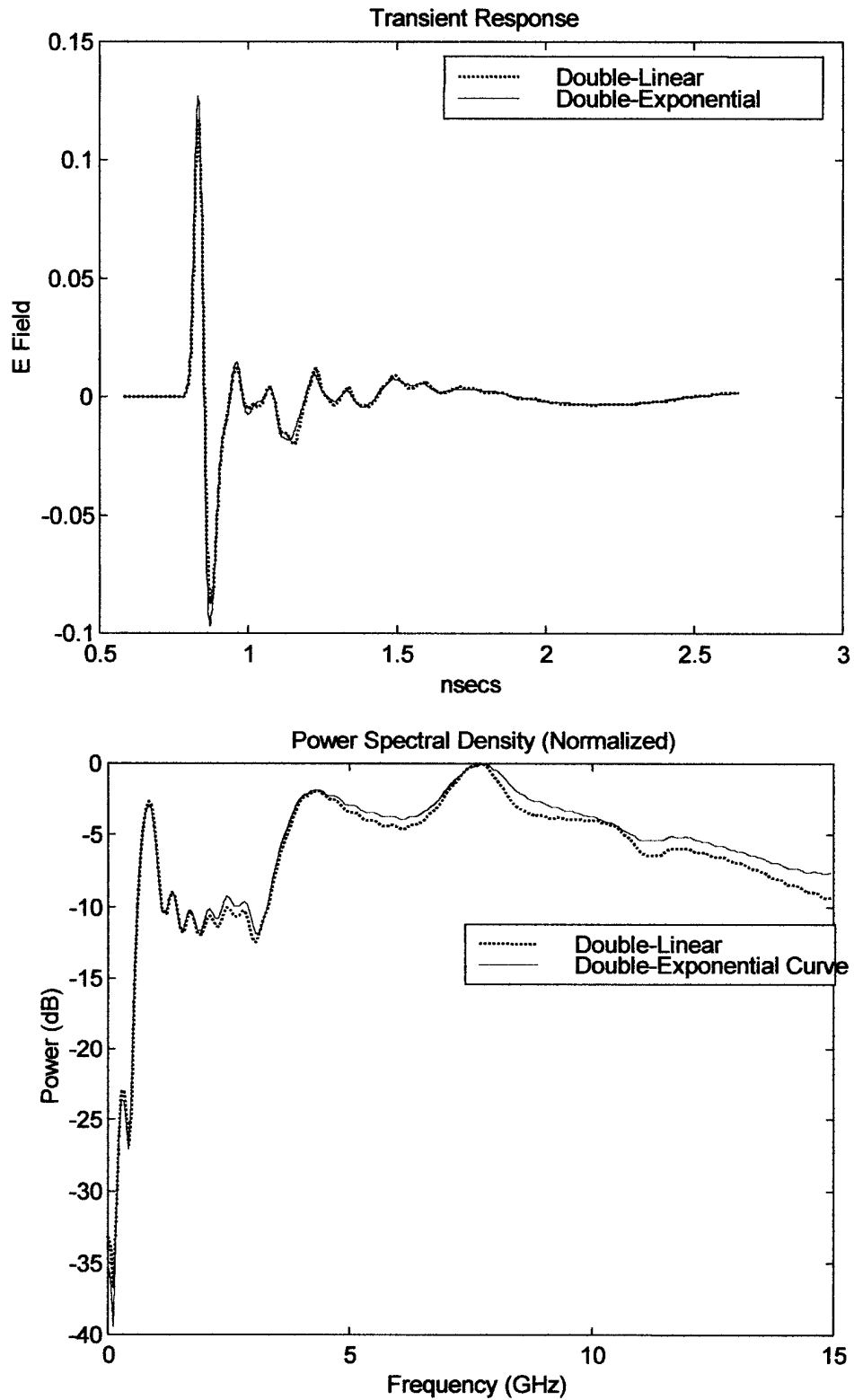


Figure D-6. Comparison of Double-Linear and Double-Exponential Taper Curve (2-Element, Small Horn, Gaussian Input Pulse)

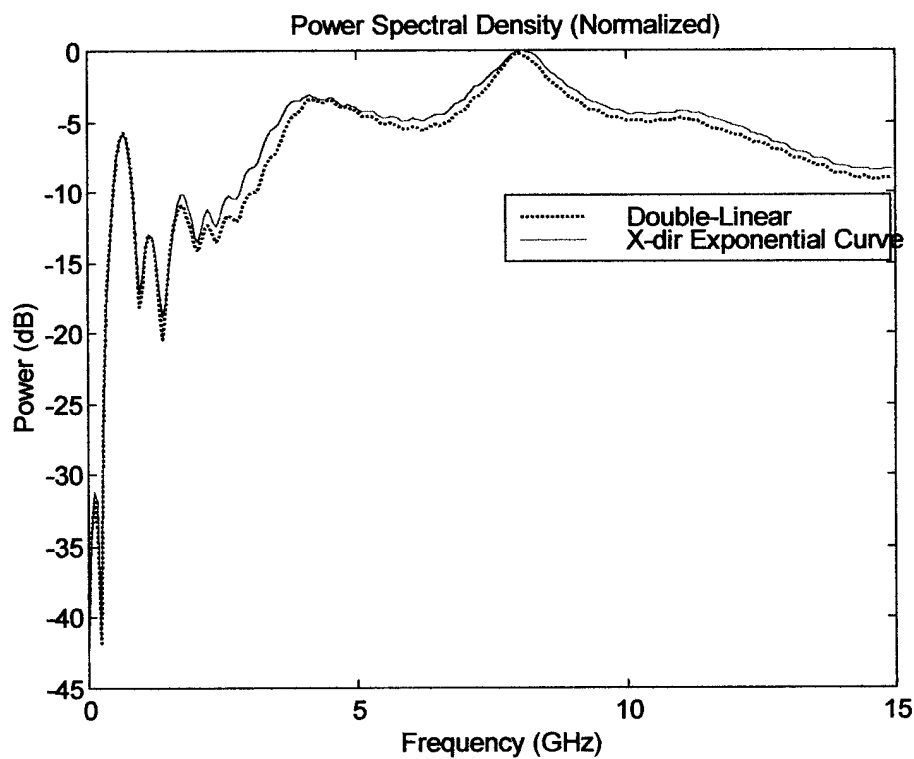
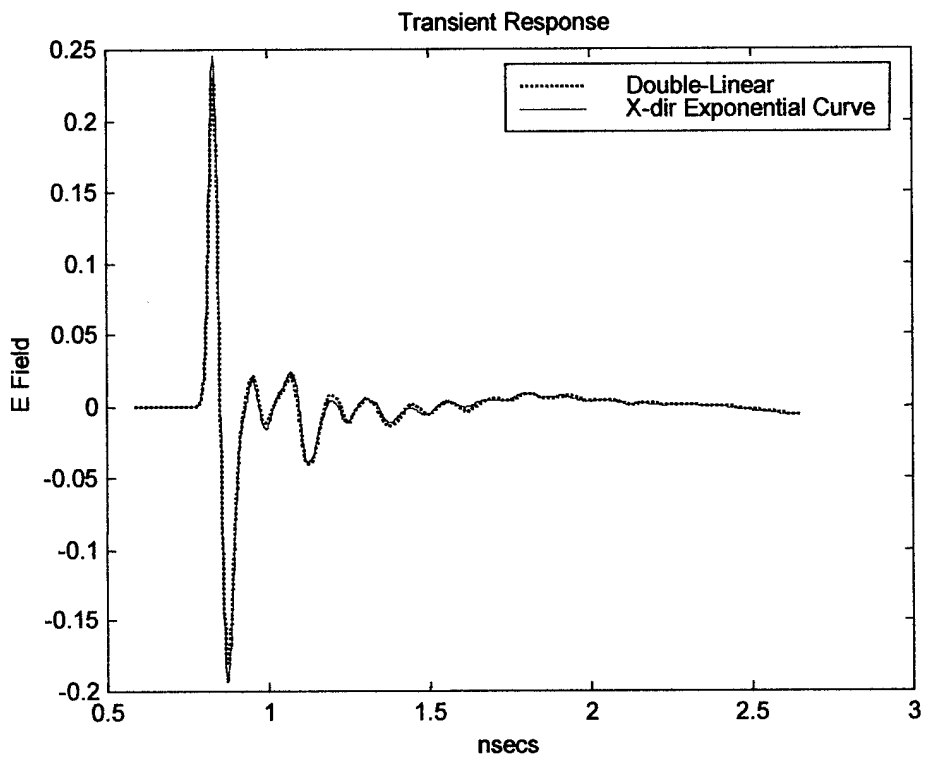


Figure D-7. Comparison of Double-Linear and X-dir Exponential Taper Curve (4-Element, Small Horn, Gaussian Input Pulse)

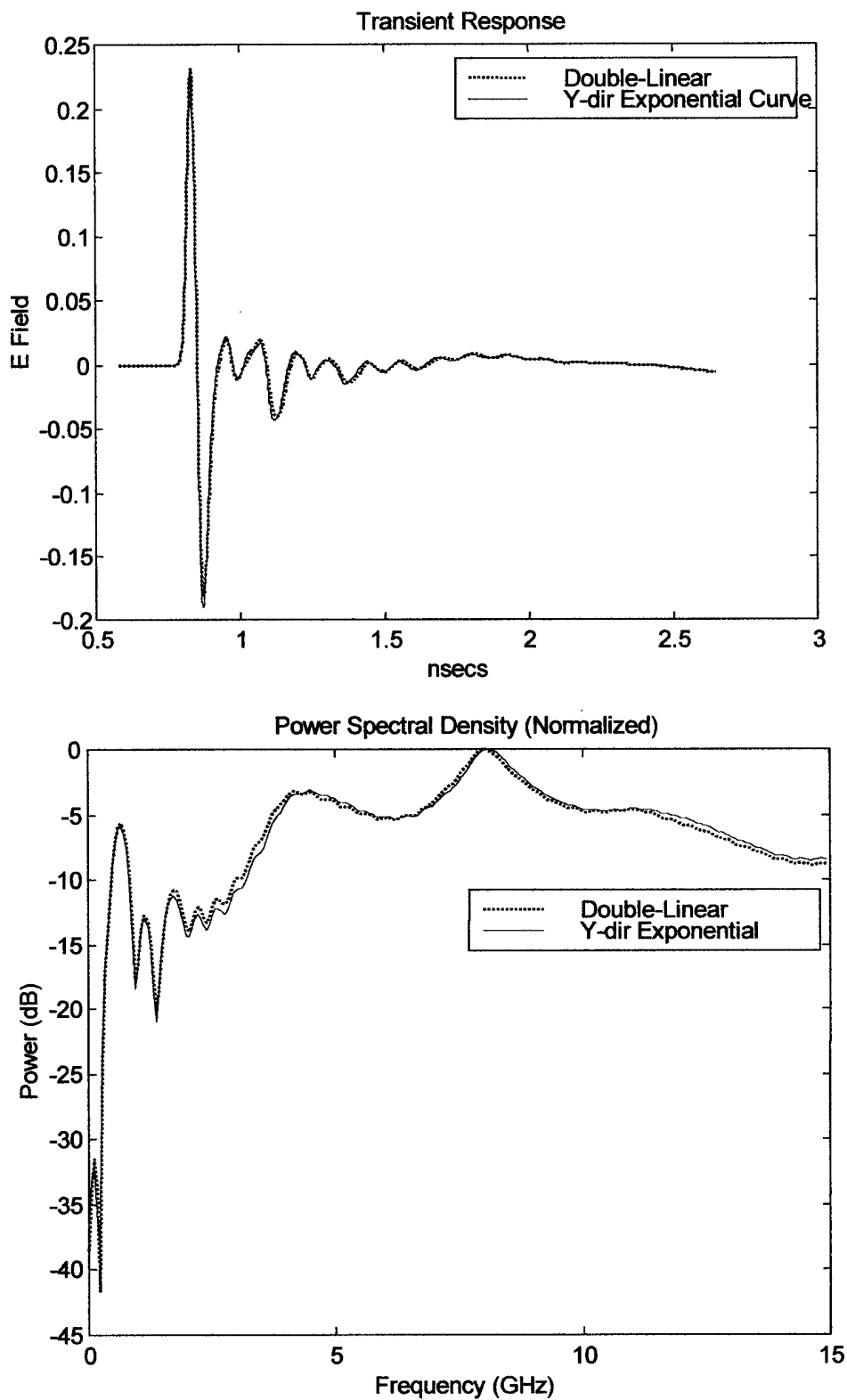


Figure D-8. Comparison of Double-Linear and Y-dir Exponential Taper Curve (4-Element, Small Horn, Gaussian Input Pulse)

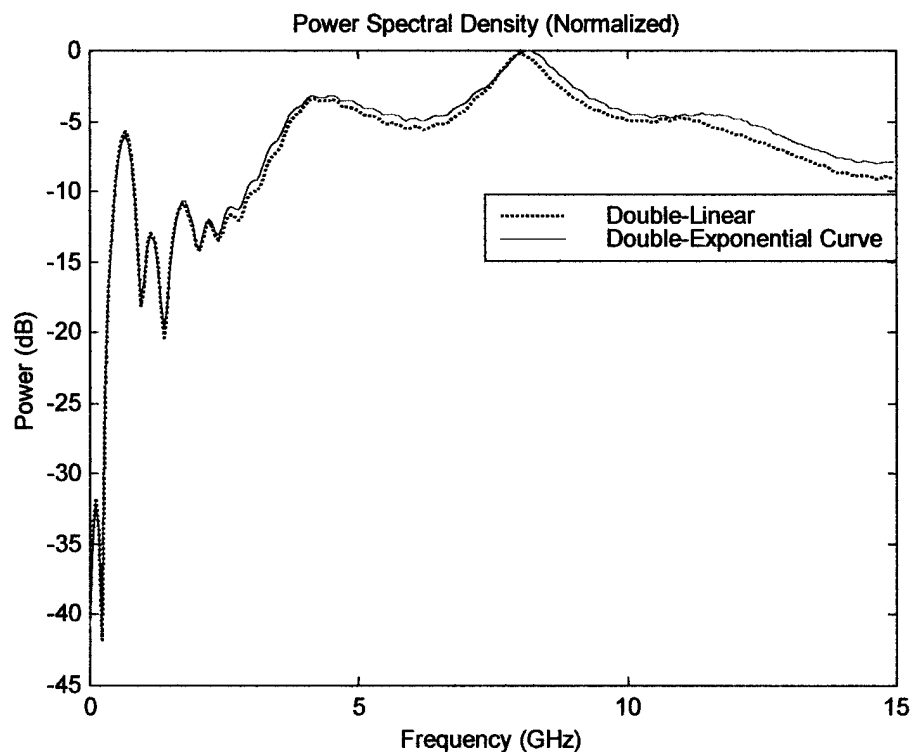
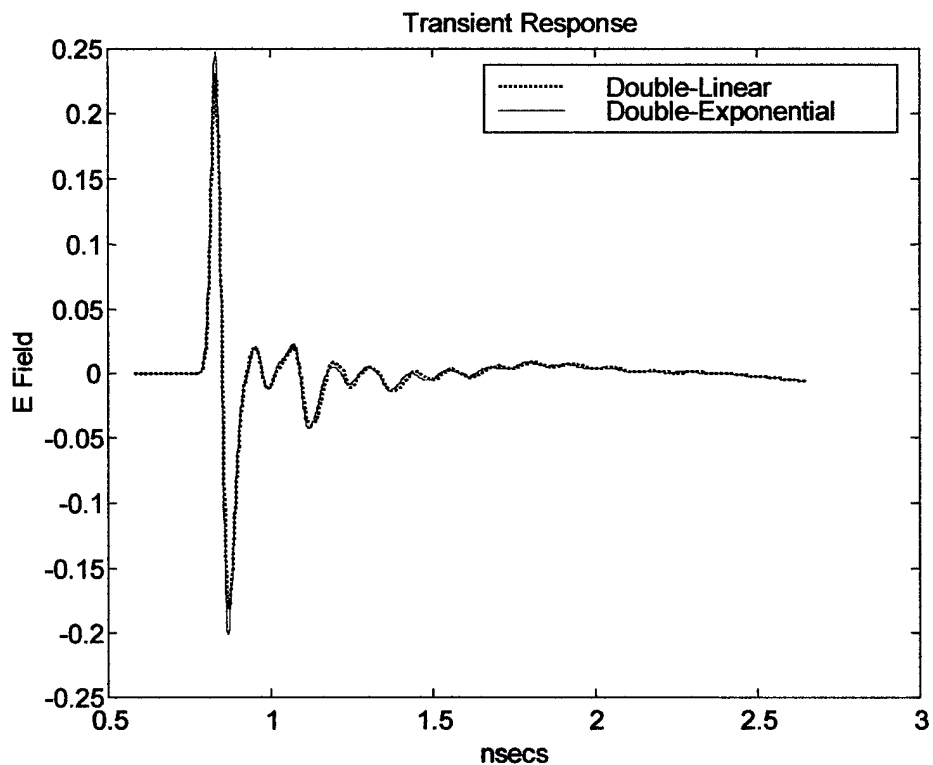


Figure D-9. Comparison of Double-Linear and Double-Exponential Taper Curve (4-Element, Small Horn, Gaussian Input Pulse)

Bibliography

- [1] Ondrejka, A. R., J. M. Ladbury, H.W. Medley, and R. Johuk. "TEM Horn Antenna Design Guide," National Institute of Standards and Technology, unpublished report
- [2] Shlager, Kurt L., Glen S. Smith, and James G. Malony, "Accurate Analysis of TEM Horn Antennas for Pulse Radiation," IEEE Transactions on Electromagnetic Compatibility, vol. 38, no.3:414-423, August 1996
- [3] Wolstenholme, Dennis J. Reduction of Off-Boresight Fields For a TEM Horn Antenna, MS thesis, AFIT/GE/ENG/94D-33. School of Engineering, Air Force Institute of Technology (AETC), Wright-Patterson AFB OH, December 1994.
- [4] Stutzman, Warren L. and Gary A. Thiele. Antenna Theory and Design 2nd ed. New York: John Wiley & Sons, Inc., 1998
- [5] Samaddar, S.N. and E.L. Mokole. "Some Basic Properties of Antennas Associated with Ultrawideband Radiation," in Ultra-Wideband, Short-Pulse Electromagnetic, Carl E. Baum, Lawrence Carin, and Alexander P. Stone, New York and London: Plenum Press, 1997
- [6] Giri D.V. and H. Lackner. A Reflector Antenna for Radiating Impulse-Like Waveforms. Sensor and Simulation Notes – Note 382. AFRL/DEH, 4 July 1995.
- [7] McLoad, Robert R. "Temporal Scattering and Response Software: Users' Manual Version 2.1 (R)," Lawrence Livermore National Laboratory, unpublished report, September 1990
- [8] Benford, James and John Swegle. High-Power Microwaves. Boston London: Artech House, 1992
- [9] Bohl, Juergen. High Power Microwave Hazard Facing Smart Ammunitions. System Design and Assessment Notes – Note 35. AFRL/DEH, 14 December 1995.
- [10] Davanloo, Farzin, Dan L. Borovina, Johnnell L. Koriath, Raymond K. Krause, Carl B. Collins, Forrest J. Agee, Jon P. Hull, Jon S.H. Schoenberg, and Lawrence E. Kingsley. "High Power, Sub-Nanosecond Rising Waveforms Created by the Stacked Blumlein Pulsers," Ultra-Wideband, Short-Pulse Electromagnetic 3, Carl E. Baum, Lawrence Carin, and Alexander P. Stone, New York and London: Plenum Press, 1997
- [11] Tesch F.M. Some Considerations for the Design of Pulse-Radiating Antennas. Sensor and Simulation Notes – Note 398. AFRL/DEH, 12 July 1996.

- [12] Kanda, M. "Transients a Resistively Loaded Linear Antenna Compared With Those in a Conical Antenna and a TEM," IEEE Trans. Antennas & Propagation, vol. 28, :132-136, Jan 1980.
- [13] Theodorou, E.A., M.R. Gorman, P.R. Riggs, and F.N. Kong. "Broadband Pulse Optimized Antenna," IEE Proc. vol. 130, part H, no. 6:403-409, October 1983.
- [14] Kanda, M. "The Effects of Resistive Loading of TEM Horns," IEEE Trans. on Electromagnetic Compatibility, vol. 24, no. 2:245-255, 2 May 1982.
- [15] Robertson, R. Clark and Michael A. Morgan. "Ultra-Wideband Impulse Receiving Antenna Design and Evaluation," in Ultra-Wideband, Short-Pulse Electromagnetic 2, Lawrence Carin, and Alexander P. Stone, New York and London: Plenum Press, 1995
- [16] Vogel, M.H. "Design of the Low-Frequency Compensation of an Extreme-Bandwidth TEM Horn and Lens IRA," in Ultra-Wideband, Short-Pulse Electromagnetic, Carl E. Baum, Lawrence Carin, and Alexander P. Stone, New York and London: Plenum Press, 1997
- [17] Baum Carl E. Low-Frequency-Compensated TEM Horn . Sensor and Simulation Notes – Note 377. AFRL/DEH, 28 January 1995.
- [18] Felsen, L.B. Topics in Applied Physics – Transient Electromagnetics Fields. Berlin Heidelberg New York: Springer-Verlag, 1976.
- [19] Maloney, James G. and Glen S. Smith. "Optimization of a Resistively Loaded Conical Antenna for Pulse Radiation," Proc. 1992 IEEE AP-S Int. Symp. vol. 4:1968-1971, Chicago, IL, July 1992.
- [20] Maloney, James G. Analysis and Synthesis of Transient Antennas using the Finite Difference Time Domain (FDTD) Method. PhD dissertation. Georgia Institute of Technology, Atlanta, GA, 1992.
- [21] Baum, Carl E. "Transient Arrays," Ultra-Wideband, Short-Pulse Electromagnetic 3, Carl E. Baum, Lawrence Carin, and Alexander P. Stone, New York and London: Plenum Press, 1997
- [22] Baum, Carl E. Timed Arrays for Radiating Impulse-Like Transient Fields . Sensor and Simulation Notes – Note 361. AFRL/DEH, 31 July 1993.
- [23] Schwartz, Jodi Lisa, and Bernard D. Steinberg. "Properties of Ultrawideband Arrays," Ultra-Wideband, Short-Pulse Electromagnetic 3, Carl E. Baum, Lawrence Carin, and Alexander P. Stone, New York and London: Plenum Press, 1997

- [24] Yakura, Joe S. Analysis of Rectangular Profile Transverse Electromagnetic Horn Antennas for Pulse Radiation Using A Finite-Difference-Time-Domain Technique: Final Report, March 1997. PL-TR-97-1096. Phillips Laboratory, Advanced Weapons and Survivability Directorate. Air Force Material Command, Kirtland Air Force Base, NM, March 1997.
- [25] Yee, K.S. "Numerical Solution of Initial Boundary Value Problems Involving Maxwell's Equations in Isotropic Media," IEEE Antennas & Propagation Magazine, vol. 14:302-307, 1966.
- [26] Shlager, Kurt L. and John B. Schneider. "A Selective Survey of Finite-Difference Time-Domain Literature," IEEE Antennas & Propagation Magazine, vol. 37, no. 4:39-56, 1995.
- [27] Taflove, Allen. Computational Electrodynamics, The Finite-Difference Time-Domain Method, Boston London, Artech House, 1995.
- [28] Kunz, Karl S. and Raymond J. Luebbers. The Finite Difference Time Domain Method for Electromagnetics, Boca Raton, CRC Press, 1993.
- [29] Katz, Daniel S., Melinda J. Piket-May, Allen Taflove, Koranda R. Unashankar. "FDTD Analysis of Electromagnetic Wave Radiation from Systems Containing Horn Antennas," IEEE Trans. Antennas & Propagation, vol.39,:1203-1212, August 1991.
- [30] Thiele, Eric and A. Taflove. "FD-TD Analysis of Vivaldi Flared Horn Antennas and Arrays," IEEE Trans. Antennas & Propagation, vol. 42,:633-640, May 1994.
- [31] Schneider, John B. and Kurt L. Shlager. "FDTD Simulations of TEM Horns and the Implications for the Staircase Representation," IEEE Trans. Antennas & Propagation, vol.45,:1830-1838, December 1997.
- [32] Hecken, R.P. "The Near-Optimum Matching Section Without Discontinuities," IEEE Trans. on Microwave Theory and Techniques, vol. 20,:734-739, November 1972.
- [33] Evans, S. and Associates. "TEM Horn Antenna: Input Reflection Characteristics in Transmission," IEE Proceedings, vol. 130, Pt. H, No. 6,:403-409, October 1983
- [34] Sandlin, Brian S. A Wire Antenna Designed for Space Wave Radiation Over the Earth Using a Genetic Algorithm, MS thesis, AFIT/GE/ENG/97D-10. School of Engineering, Air Force Institute of Technology (AETC), Wright-Patterson AFB OH, December 1997
- [35] Author Unknown. MGED User's Manual:1-4,
<http://ftp.arl.mil/~mike/papers/brlcad5.0/html/BRLCAD/mged/mged.html>

Vita

Troy Utton was born in Durango, Colorado and raised in Glenrock, Wyoming, where his parents, Bill and Dana, still reside. Upon graduating from Glenrock High School he attended Embry-Riddle Aeronautical University in Prescott, AZ. Besides graduating with a Bachelor of Science in Electrical Engineering in 1993, another wonderful thing happened, he met his future wife, the former Miss Glendora Ferguson. Upon their graduation, they made the trek to Hill AFB, UT, where Troy's first assignment was as the Avionics Flight Controls Engineer for the entire F-16A&B fleet (and some systems on the C&D fleet) in the F-16 Management Directorate, Ogden Air Logistics. Two more wonderful events happened while in Utah. Troy and Glendora were married in May of 1995 and blessed with a son, Ty, in July of 1996. In July of 1997 the three of them, along with Tazzy and Ruger (Siberian Huskies), transversed the continent, arriving at Wright-Patterson AFB in August of 1997, where for the next 18 months Troy attended AFIT taking the Electromagnetic Curriculum with a focus in antennas. During this period they were once again blessed with a healthy baby girl, Sierra Marie.

The six of them plan to transverse the continent once again to Troy's follow on assignment at Phillips Laboratory, Kirtland AFB, NM.

Permanent Address: P.O. Box 249
Glenrock WY
82637